

Effect of Corrosion Inhibitor on Water Wetting and Carbon Dioxide Corrosion In  
Oil-Water Two-Phase Flow

A dissertation presented to  
the faculty of  
the Russ College of Engineering and Technology of Ohio University

In partial fulfillment  
of the requirements for the degree  
Doctor of Philosophy

Chong Li

June 2009

© 2009 Chong Li. All Rights Reserved.

This dissertation titled  
Effect of Corrosion Inhibitor on Water Wetting and Carbon Dioxide Corrosion In  
Oil-Water Two-Phase Flow

by

CHONG LI

has been approved for  
the Department of Chemical and Biomolecular Engineering  
and the Russ College of Engineering and Technology by

---

Srdjan Nesic

Professor of Chemical and Biomolecular Engineering

---

Dennis Irwin

Dean, Russ College of Engineering and Technology

**ABSTRACT**

LI, CHONG, Ph.D., June 2009, Chemical Engineering

Effect of Corrosion Inhibitor on Water Wetting and Carbon Dioxide Corrosion In Oil-Water Two-Phase Flow (198 pp.)

Director of Dissertation: Srdjan Nesic

The internal corrosion of flowlines and pipelines made from carbon steel is encountered in the oil and gas industry. The corrosion process is primarily associated with the presence of free water in offshore or onshore production, particularly when it is accompanied by carbon dioxide gas. Corrosion inhibitor injection in oilfields is a very common and useful method for pipeline internal corrosion prevention. There is a need to understand the physics of phase wetting, carbon dioxide corrosion and the effect of corrosion inhibitor on those two processes in oil-water two-phase flow.

In this study, the flow patterns and phase wetting regimes of oil-water two-phase flow were experimentally investigated in a large scale flow loop. Five major flow patterns were observed within the test flow conditions by flow visualization. Three types of phase wetting regimes (water wetting, oil wetting and intermittent wetting) were found by using a carbon steel test section consisting of wall conductance probes, wall sampling and corrosion monitoring. Based on experimental results, phase wetting maps were generated for model oil and five crude oils in the flow loop tests.

Following the large scale flow loop tests, a small scale flow apparatus, called a doughnut cell was developed to simulate phase wetting occurring in oil-water two-phase

pipe flow. Phase wetting maps were created for model oil and five crude oils in the doughnut cell tests.

Two generic inhibitors, quaternary ammonium chloride and fatty amino were studied in this work. Corrosion inhibition tests showed that a direct exposure to oil phase enhances the performance of fatty amino inhibitor. Both inhibitors produce not only a reduction in oil-water interfacial tension, which promotes easier water entrainment by the oil, but also changes the wettability of the steel surface from hydrophilic to hydrophobic, which may reduce the possibility of CO<sub>2</sub> corrosion.

A mechanistic phase wetting prediction model was developed to predict the transition between water breakout and full water entrainment. The model was validated with the experimental results of model oil and crude oils obtained from flow loop and doughnut cell tests. The model predictions have a good agreement with empirical results of model oil, but the model overpredicts the critical oil velocity of full water entrainment for all tested crude oils. The phase wetting prediction model is also used to correct the geometry difference between doughnut cell and flow loop. A corrosion inhibition model was built based on fitting corrosion inhibition test results with the Langmuir adsorption isotherm. A strategy is proposed to predict uninhibited and inhibited CO<sub>2</sub> corrosion rate in oil-water two-phase pipe flow by integrating phase wetting, CO<sub>2</sub> corrosion and inhibition models.

Approved: \_\_\_\_\_

Srdjan Nesic

Professor of Chemical and Biomolecular Engineering

**DEDICATION**

*To*

*My parents, Wencai Li and Baochen Nie*

*and*

*My wife, Dan Li and my son, Eric X. Li*

## ACKNOWLEDGMENTS

My deepest gratitude is to my advisor, Dr. Srdjan Nestic for his support, guidance and encouragement during my Ph.D. study at Ohio University. Throughout my Ph.D. research at Institute for Corrosion and Multiphase Technology, Dr. Nestic taught and encouraged me to develop professional research skills.

I would like to express my sincere appreciation to Dr. Jiyong Cai, Dr. Khairul Alam, Dr. Sonja Richter for their leadership on my research project and to Dr. Winston Robbins for his advice on corrosion inhibitor study. I would also like to acknowledge my indebtedness to Mr. Albert Schubert, Mr. John Goettge, Mr. Danny Cain, Mr. Cody Shafer, Mr. Bruce Brown, Mr. Marc Singer and Mr. Garret Brown for their assistance in the technical work. I appreciate all the joint work and invaluable discussion with students, Mr. Xuanping Tang, Mr. Francois Ayello, Mr. Pankaj Ajmera and Ms. ShanShan Yang in Water Wetting JIP; All the fellow students, Ms. Edie Chalfant and Ms. Debra Bullington for turning the Institute for Corrosion and Multiphase Technology to be a warm home for me.

I would like to thank the faculty members, Dr. Valerie Young and Dr. Daniel Gulino for their guidance on academic issues and Dr. David Young for providing me invaluable advice on my dissertation, paper publications and student posters.

I would like to acknowledge the sponsor companies, BP, ConocoPhillips, Eni, ExxonMobil, Petrobras, Saudi Aramco, Shell and Total, for giving the financial support and technical directions for my research work.

## TABLE OF CONTENTS

	Page
Abstract.....	3
Dedication.....	5
Acknowledgments.....	6
List of tables.....	9
List of figures.....	11
Chapter 1: Introduction.....	16
Chapter 2: Literature review.....	21
2.1 Carbon dioxide corrosion.....	21
2.1.1 Mechanisms of carbon dioxide corrosion.....	21
2.1.2 Factors affecting carbon dioxide corrosion.....	25
2.1.3 Modeling of carbon dioxide corrosion.....	29
2.1.4 Carbon dioxide corrosion control strategies.....	34
2.2 Oil-water two-phase pipe flow.....	38
2.2.1 Characteristics of oil-water two-phase pipe flow.....	38
2.2.2 Modeling of oil-water two-phase flow.....	46
2.2.3 Small scale apparatus for studying oil-water two-phase flow.....	59
2.3 Corrosion inhibitors.....	63
2.3.1 Surface active properties.....	63
2.3.2 Modeling of corrosion inhibition.....	68
Chapter 3: Research objectives.....	72
Chapter 4: Experimental study of oil-water pipe flow.....	75
4.1 Experimental setup and procedure.....	75
4.1.1 Multiphase flow loop.....	75
4.1.2 Test sections and instrumentation.....	80
4.1.3 Experimental procedure.....	84
4.1.4 Test matrix.....	84
4.2 Results and discussion.....	85
4.3 Summary.....	106
Chapter 5: Experimental study of carbon dioxide corrosion inhibition.....	110
5.1 Experimental setup and procedure.....	110
5.1.1 Equipment.....	110
5.1.2 Experimental procedure.....	111
5.1.3 Test matrix.....	114
5.2 Results and discussion.....	116
5.2.1 Pure corrosion inhibition tests.....	116
5.2.2 Direct oil wet tests.....	124
5.2.3 Partitioning tests.....	127
5.3 Summary.....	129
Chapter 6: Experimental study of corrosion inhibitor surface active properties.....	130
6.1 Experimental setup and procedure.....	130

6.1.1 Equipment .....	130
6.1.2 Experimental procedure .....	131
6.1.3 Test matrix .....	133
6.2 Results and discussion .....	135
6.3 Summary .....	141
Chapter 7: Experimental study of oil-water two-phase flow in doughnut cell .....	142
7.1 Experimental setup and procedure .....	142
7.1.1 Development of the doughnut cell .....	142
7.1.2 Experimental procedure .....	147
7.1.3 Test matrix .....	148
7.2 Results and discussion .....	148
7.3 Summary .....	159
Chapter 8: Phase wetting and carbon dioxide corrosion inhibition prediction models ..	160
8.1 Phase wetting prediction model .....	160
8.1.1 Model development .....	160
8.1.2 Linkage between doughnut cell and flow loop .....	165
8.1.3 Model verification .....	167
8.2 Carbon dioxide corrosion inhibition model .....	175
8.2.1 Model development .....	175
8.3 Summary .....	179
Chapter 9: Conclusions and future work .....	181
9.1 Conclusions .....	181
9.2 Future work .....	182
Reference .....	184
Appendix A: Interface of acquisition software for wall conductance probes used on flow loop and doughnut cell .....	195

## LIST OF TABLES

	Page
Table 1 List of adsorption isotherms. ....	71
Table 2 Main components in multiphase flow loop system displayed in Figure 10.....	76
Table 3 Test matrix for oil-water two-phase flow loop tests. ....	85
Table 4 Physical properties of model oil and seven crude oils tested in this research work. .....	85
Table 5 Comparison of wall sampling results with flow patterns and phase wetting regimes obtained in the model oil-brine horizontal pipe flow. ....	92
Table 6 Comparison of wall sampling results with phase wetting regimes obtained in the C1 crude oil-brine horizontal pipe flow. ....	96
Table 7 Comparison of wall sampling results with phase wetting regimes obtained in the C2 crude oil-brine horizontal pipe flow. ....	97
Table 8 CO <sub>2</sub> corrosion rate under different phase wetting regimes in C2 crude oil-brine horizontal pipe flow. ....	97
Table 9 Comparison of wall sampling results with phase wetting regimes obtained in the C3 crude oil-brine horizontal pipe flow. ....	98
Table 10 CO <sub>2</sub> corrosion rate under different phase wetting regimes in C3 crude oil-brine horizontal pipe flow. ....	98
Table 11 Comparison of wall sampling results with phase wetting regimes obtained in the C4 crude oil-brine horizontal pipe flow. ....	100
Table 12 CO <sub>2</sub> corrosion rate measured by ER probe under C4 crude oil-brine emulsion formation in flow loop tests with pipe inclinations. ....	101
Table 13 CO <sub>2</sub> corrosion rate measured by ER probe under C4 crude oil-brine emulsion formation in horizontal flow loop tests with high water cut. ....	101
Table 14 Comparison of wall sampling results with phase wetting regimes obtained in the C5 crude oil-brine horizontal pipe flow. ....	102
Table 15 CO <sub>2</sub> corrosion rate under different phase wetting regimes in C5 crude oil-brine horizontal pipe flow. ....	103
Table 16 CO <sub>2</sub> corrosion rate measured by ER probe under C5 crude oil-brine emulsion formation in horizontal flow loop tests with water cut from 20 to 70%. ....	103
Table 17 Compositions of fatty amino inhibitor package (as received from Champion Technologies). ....	115
Table 18 Compositions of quaternary ammonium chloride inhibitor package (as received from Champion Technologies). ....	115
Table 19 Test matrix of corrosion inhibition test series conducted in glass cell. ....	115
Table 20 Chemical composition of ASTM 1018 carbon steel. ....	115
Table 21 Test matrix of oil-water interfacial tension measurements. ....	134
Table 22 Test matrix of contact angle measurements. ....	134
Table 23 Test matrix of emulsion stability measurements. ....	134
Table 24 Chemical composition of X65 carbon steel. ....	134
Table 25 Test matrix of the doughnut cell tests. ....	148

Table 26 List of the factor of safety for the model oil and five different crude oils in the flow loop tests. ....	169
Table 27 Factor of safety for the model oil and five crude oils in the doughnut cell tests. ....	172

## LIST OF FIGURES

	Page
Figure 1 Six oil-water two-phase flow patterns proposed by Trallero (1995). The light color phase represents water phase and the dark color phase is for the oil phase. ....	41
Figure 2 Force analysis on a dispersed droplet in the continuous flowing phase. $F_g$ – radial component of gravity acting on the droplet, $F_t$ – radial component of turbulent velocity fluctuations acting on the droplet and $\beta$ – pipe inclination. ....	53
Figure 3 Cross section view of the three-layer stratified oil-water two-phase pipe flow (Cai et al., 2004). ....	56
Figure 4 Schematic of oil-water three-layer stratified flow. ....	56
Figure 5 3D rendering of a horizontal rotating cylinder apparatus for studying effect of water wetting on CO <sub>2</sub> corrosion (Nesic and Carroll, 2003). ....	60
Figure 6 Real view of updated horizontal rotating cylinder apparatus (Cai et al., 2005b). .....	61
Figure 7 Small scale apparatus, carousel, used for studies of water entrainment and breakout in crude oil (Pots et al., 2006). ....	62
Figure 8 Contact angle of a water droplet on carbon steel surface immersed in a continuous oil phase, showing how the interfacial tension at oil-water, oil-steel and water–steel determine the shape of the droplet (Li et al., 2008). ....	65
Figure 9 Equivalent circuits for CO <sub>2</sub> corrosion: (a) without inhibitor; (b) with inhibitor. The addition of inhibitor adds another time constant to the Equivalent circuit. ....	69
Figure 10 Schematic of multiphase flow loop used for large scale oil-water two-phase investigation (Courtesy of Jiyong Cai). ....	75
Figure 11 Schematic of the internal structure of oil-water separator, which is a part of the inclinable flow loop system used in this study (Courtesy of Jiyong Cai). ....	78
Figure 12 pH probe port and water sampling port on the water boot of the separator, which is a part of the inclinable flow loop system used in this work. ....	79
Figure 13 Upstream test section of the inclinable flow loop system used in this work. ....	80
Figure 14 Schematic of a test section with the instrumentation marked (Courtesy of Joshua Addis). ....	81
Figure 15 Staggered spatial arrangement on the upstream test section for wall conductance probes. ....	82
Figure 16 Flow pattern map of model oil-brine in horizontal pipe flow. ....	87
Figure 17 Flow pattern of stratified flow with water droplets: (a) red food color dyed water and model oil at mixture velocity of 0.52 m/s and water cut of 4.9%; (b) fluorescein dyed water and model oil at mixture velocity of 0.5 m/s and water cut of 5%. ....	88
Figure 18 Flow pattern of stratified flow with mixing layer: (a) mixture velocity of 0.61 m/s and water cut of 18%; (b) mixture velocity of 0.75 m/s and water cut of 20%. ....	88
Figure 19 Phase wetting map of model oil-brine in horizontal, 4 inch pipe flow. The dotted line shows a transition from intermittent to oil wetting. ....	89
Figure 20 CO <sub>2</sub> corrosion rate measured with Fe <sup>2+</sup> concentration monitoring under different phase wetting regimes in model oil-brine horizontal pipe flow. ....	93

Figure 21 Phase wetting map of C1 crude oil-brine in horizontal pipe flow. The dotted line shows a transition from intermittent to oil wetting.....	95
Figure 22 Phase wetting map of C2 crude oil-brine in horizontal pipe flow. The dotted line shows a transition from intermittent to oil wetting.....	96
Figure 23 Phase wetting map of C3 crude oil-brine in horizontal pipe flow. The dotted line shows a transition from intermittent to oil wetting.....	98
Figure 24 Phase wetting map of C4 crude oil-brine in horizontal pipe flow. The dotted line shows a transition from intermittent to oil wetting.....	99
Figure 25 Phase wetting map of C5 crude oil-brine in horizontal pipe flow. The dotted line shows a transition from intermittent to oil wetting.....	102
Figure 26 Comparison of transition lines from intermittent to oil wetting for model oil and five different crude oils in horizontal, 4 inch pipe flow.....	105
Figure 27 Comparison of transition lines from intermittent wetting to oil wetting for C1 crude oil-brine in horizontal and inclined upstream pipe flows. ....	108
Figure 28 Comparison of transition lines from intermittent wetting to oil wetting for C1 crude oil-brine in horizontal and inclined downstream pipe flows.....	108
Figure 29 Comparison of transition lines from intermittent wetting to oil wetting for C3 crude oil-brine in horizontal and inclined upstream pipe flows. ....	109
Figure 30 Comparison of transition lines from intermittent wetting to oil wetting for C3 crude oil-brine in horizontal and inclined downstream pipe flows.....	109
Figure 31 Schematic of glass cell set up (Courtesy of Jiabin Han). ....	111
Figure 32 General chemical structures of the (a) quaternary ammonium chloride (“quat”) and (b) fatty amino compound. R represents a hydrocarbon chain in the structure. ....	115
Figure 33 Potentiodynamic sweeps for 100 ppm “quat” pure inhibition test. ....	117
Figure 34 Potentiodynamic sweeps for 100 ppm fatty amino pure inhibition test. ....	117
Figure 35 Corrosion rates measured by LPR for “quat” pure corrosion inhibition tests at different concentrations. The vertical dotted line indicates inhibitor addition time. ....	119
Figure 36 Corrosion rates measured by LPR for fatty amino pure corrosion inhibition tests at different concentrations. The vertical dotted line indicates inhibitor addition time. ....	119
Figure 37 Summary of corrosion rate and inhibition efficiency versus inhibitor concentration for “quat” and fatty amino inhibitors in pure corrosion inhibition tests. .	120
Figure 38 Comparison of potentiodynamic sweeps at different concentrations of “quat” in pure corrosion inhibition tests.....	121
Figure 39 Corrosion potential <i>versus</i> corrosion current of corrosion points measured with the LPR at 200 ppm “quat” in pure corrosion inhibition tests.....	123
Figure 40 Comparison of potentiodynamic sweeps at different concentrations of fatty amino in pure corrosion inhibition tests.....	123
Figure 41 Corrosion potential versus corrosion current of corrosion points measured by LPR at 5 ppm fatty amino in pure corrosion inhibition tests.....	124
Figure 42 Comparison of corrosion rates in direct oil wet and pure corrosion inhibition tests for 5 ppm “quat” inhibitor. The vertical dotted line indicates inhibitor addition timeline and other vertical solid lines indicate oil wetting timelines.....	125

Figure 43 Comparison of corrosion rates in direct oil wet and pure corrosion inhibition tests for 60 ppm “quat” inhibitor. The vertical dotted line indicates inhibitor addition timeline and other vertical solid lines indicate oil wetting timelines.....	125
Figure 44 Comparison of corrosion rates in direct oil wet and pure corrosion inhibition tests for 1 ppm fatty amino inhibitor. The straight dotted line indicates inhibitor addition timeline and other straight solid lines indicate oil wetting timelines.....	127
Figure 45 Comparison of corrosion rates in direct oil wet and pure corrosion inhibition tests for 5 ppm fatty amino inhibitor. The vertical dotted line indicates inhibitor addition timeline and other vertical solid lines indicate oil wetting timelines.....	127
Figure 46 Comparison of corrosion rates in partitioning and pure corrosion inhibition tests for 5 ppm fatty amino inhibitor. The straight dotted line indicates inhibitor addition time and two straight solid lines represent the model oil addition timelines.....	128
Figure 47 A real view picture of the CSC-DuNouy tensiometer used to measure oil-water interfacial tension (Courtesy of Francois Ayello).....	131
Figure 48 A real view of the system including goniometer, camera and light source used to measure contact angle of droplet on the steel surface (Courtesy of Xuanping Tang). 132	132
Figure 49 Model oil-brine interfacial tension measured at different concentrations of fatty amino and “quat” corrosion inhibitors.....	135
Figure 50 Images of oil droplet on steel surface in contact angle measurements with 0, 1, 5, 20 and 200 ppm fatty amino inhibitor added in the continuous water phase. In the pictures, inhibitor concentrations and measured contact angle values are written on the black areas, which are the bottom portions of carbon steel specimens. ....	136
Figure 51 Images of oil droplet on steel surface in contact angle measurements with 0, 1, 5, 20 and 200 ppm “quat” inhibitor added in the continuous water phase. In the pictures, inhibitor concentrations and measured contact angle values are written on the black areas, which are the bottom portions of carbon steel specimens. ....	137
Figure 52 Contact angles of oil-in-water versus inhibitor concentration for “quat” and fatty amino. ....	137
Figure 53 Images of water droplet on steel surface in contact angle measurements with 0, 1, 5 and 200 ppm fatty amino inhibitor added in the continuous oil phase. In the pictures, inhibitor concentrations and measured contact angle values are written on the black areas, which are the bottom portions of carbon steel specimens. ....	138
Figure 54 Recorded time for model oil-brine complete separation in emulsion stability tests with “quat” and fatty amino addition at 20% water cut.....	140
Figure 55 Recorded time for model oil-brine complete separation in emulsion stability tests with “quat” and fatty amino addition at 50% water cut.....	141
Figure 56 The whole doughnut cell test system with main components named. ....	143
Figure 57 Cut view of the doughnut cell with main components numbered and named. 144	144
Figure 58 3D schematic of the DC motor mounted on the key plate and motor holder. 145	145
Figure 59 A schematic top view of the stainless steel 316 flange. ....	147
Figure 60 Phase wetting map of model oil-brine in doughnut cell experiments. The dotted line shows a transition line from intermittent to oil wetting.....	149
Figure 61 Phase wetting map of C1 crude oil-brine in doughnut cell experiments. The dotted line shows a transition from intermittent to oil wetting.....	150

Figure 62 Phase wetting map of C2 crude oil-brine in doughnut cell experiments. The dotted line shows a transition from intermittent to oil wetting. ....	151
Figure 63 Phase wetting map of C3 crude oil-brine in doughnut cell experiments. The dotted line shows a transition from intermittent to oil wetting. ....	151
Figure 64 Phase wetting map of C6 crude oil-brine in doughnut cell experiments. The dotted line shows a transition from intermittent to oil wetting. ....	152
Figure 65 Phase wetting map of C7 crude oil-brine in doughnut cell experiments. The dotted line shows a transition from intermittent to oil wetting. ....	152
Figure 66 Comparison of the transition lines from intermittent wetting to oil wetting for model oil and five different crude oils in doughnut cell experiments. ....	154
Figure 67 Comparison of the transition lines from intermittent wetting to oil wetting. (a) for model oil, (b) for C1 crude, (c) for C2 crude, (d) for C3 crude and (e) for four different oils in flow loop (L) and doughnut cell (D) experiments. ....	156
Figure 68 Phase wetting map of model oil-brine with 1 ppm “quat” addition in doughnut cell experiments. The dotted line shows a transition from intermittent to oil wetting. ..	157
Figure 69 Phase wetting map of model oil-brine with 5 ppm “quat” addition in doughnut cell experiments. The dotted line shows a transition from intermittent to oil wetting. ..	157
Figure 70 Phase wetting map of model oil-brine with 20 ppm “quat” addition in doughnut cell experiments. The dotted line shows a transition from intermittent to oil wetting. ..	158
Figure 71 Comparisons of the transition lines from intermittent wetting to oil wetting for model oil-brine with 0, 1, 5 and 20 ppm “quat” inhibitor addition in the doughnut cell experiments. ....	158
Figure 72 Flow chart of the phase wetting prediction model. ....	164
Figure 73 Comparison of the predicted transition lines for model oil in the flow loop (4 inch) and the doughnut cell (2.18 inch) by the mechanistic phase wetting prediction model from intermittent wetting to oil wetting. ....	167
Figure 74 Comparison of the empirical phase wetting transition lines, (a) for mode oil, (b) for C1, (c) for C2, (d) for C3, (e) for C4 and (f) for C5 crude oils in multiphase flow loop (L) tests with the model predictions (P). ....	168
Figure 75 Phase wetting map of the model oil-brine with 5 ppm “quat” inhibitor addition in horizontal flow loop experiments. The solid and dotted lines are the phase wetting transition lines from model predictions and empirical test results, respectively. ....	171
Figure 76 Comparison of the empirical phase wetting transition lines, (a) for model oil, (b) for C1, (c) for C2, (d) for C3, (e) for C6 and (f) for C7 crude oils in the doughnut cell (D) tests with the phase wetting model predictions (P). ....	172
Figure 77 Comparison of the empirical phase wetting transition lines for the model oil-brine with (a) for 1 ppm, (b) for 5 ppm, (c) for 20 ppm “quat” inhibitor additions and (d) for all the test concentrations in the doughnut cell (D) tests with the model prediction (P). ....	173
Figure 78 Comparison of the phase wetting transition lines, (a) for model oil, (b) for C1, (c) for C2 and (d) for C3 crude oils in the flow loop (L) with that in the doughnut cell experiments corrected by the phase wetting model (D+C). ....	175
Figure 79 Corrosion inhibition experimental data of “quat” and fatty amino inhibitors fitted by the Langmuir adsorption isotherm. ....	176

Figure 80 A strategy of the uninhibited and inhibited CO<sub>2</sub> corrosion rate predictions for oil-water two-phase pipe flow by connecting the phase wetting model, three-layer stratified flow model, CO<sub>2</sub> corrosion prediction model and corrosion inhibition model. .... 179

Figure 81 Main interface of the acquisition software. .... 196

Figure 82 Interface of 160 wall conductance probes on the upstream test section..... 196

Figure 83 Interface of 93 wall conductance probes on the downstream test section..... 197

Figure 84 Interface of 140 wall conductance probes on the doughnut cell. .... 197

Figure 85 Interface of 4 traversing probes on the test section. .... 198

## CHAPTER 1: INTRODUCTION

In both offshore and onshore oilfield production, the pipelines transporting oil and gas operate with two-phase (oil-water) or three-phase (gas-oil-water) flow conditions. Crude oil, natural gas and formation water are transported by risers from downholes to wellhead platforms. Well fluids are then carried by flowlines from wellhead platforms to a treatment platform (also called central gathering platform), where the oil and gas from different wells are mixed. At the treatment platform, the mixtures are separated with separators. Oil and gas are transported separately in pipelines to treatment facilities, storage facilities and refinery plants. However, even with separation some produced water, as low as 0.5% to 2% water cut (volume ratio of water phase to total liquid phase), is not avoidable in oil transportation pipelines. After separation on the treatment platform, the formation water is injected back into the reservoirs (sometimes together with seawater and carbon dioxide gas) to maintain or increase the reservoir pressure for oilfield recovery. In this way, the quantity of produced water in aging oilfield has steadily been growing over the years.

As discussed above, oil is accompanied with formation water through the whole journey of upstream operations, from reservoirs to downstream facilities. One of the serious problems generated by the formation water is internal corrosion of flowlines and pipelines. Internal corrosion can lead to pipeline failure, loss of production, ultimately shutdown and a possible environmental disaster. The consequence is that a considerable manpower and expense is required to replace the failed facility and to conduct failure analysis. A study conducted in 2002 by CC Technologies Laboratories, Inc. on behalf of

U.S. FHWA (Federal Highway Administration, 2002) and NACE (National Association of Corrosion Engineers) shows that the cost of corrosion in oil and gas production industry in United States is about \$1.4 billion annually.

One of the frequent and major internal corrosion problems is carbon dioxide corrosion (also called sweet corrosion in the oil and gas industry). Carbon dioxide gas dissolves in the produced water and results in the formation of carbonic acid, which gives rise to acid corrosion of carbon steel pipelines. Although corrosion resistance alloys (CRAs) are produced by pipeline manufacturers to be resistive to sweet corrosion occurring in oilfields, carbon steel is still predominantly used in the design of pipelines and surface facilities in oilfields due to lower cost of carbon steel *versus* the CRAs.

The effect of multiphase flow on carbon dioxide corrosion is a complex phenomenon. It is believed that different phase wetting regimes on steel surfaces can greatly affect pipeline internal corrosion. Whenever water physically contacts the pipeline internal surface, which is termed here “water wetting”, the steel can corrode. The oil phase plays an important role in internal corrosion control. If the water is fully entrained in the flowing oil and the oil continuously wets the steel surface, where oil wetting occurs, the internal corrosion can be avoided. There is a missing link between different phase wetting regimes and corrosion prediction. Hence, it is a challenge for corrosion engineers to determine more precisely the occurrence of water wetting in multiphase flow leading to carbon dioxide corrosion and conversely oil wetting leading to corrosion free conditions.

Organic corrosion inhibitors have been widely and successfully used to maintain or increase the use of carbon steel in oilfields. They inhibit corrosion by forming an adsorbed organic compound film on the steel surface. In the past, it was well known that the adsorbed compounds work by slowing down reactions occurring in the carbon dioxide corrosion process. However, there are other important effects of inhibitors on phase wetting, which were only considered in a qualitative way. The first effect is a decrease in the oil-water interfacial tension which relates to the flow pattern of oil-water two-phase flow. The second effect is a change in the wettability of the steel surface and relates to the hydrodynamic interaction between oil, water, the adsorbed inhibitor film and the steel surface.

In order to understand the fundamentals behind water wetting and carbon dioxide corrosion in oil-water two-phase flow, a water wetting project was sponsored by Saudi Aramco Oil Company which started in 2004. Experimental studies were conducted at the Institute for Corrosion and Multiphase Technology at Ohio University in a 4 inch internal diameter (ID) fully inclinable multiphase flow loop. One model oil and five crude oils were tested with deionized water and 1 wt% NaCl in it to determine phase wetting regimes under different flow conditions. Meanwhile, a mechanistic phase wetting prediction model for oil-water two-phase flow was developed. The model is based on dispersed flow boundary prediction model extracted from the literature and is discussed in Chapter 2. The model considers pipe diameter, pipe inclination, oil and water properties (density, viscosity and interfacial tension), velocity and water cut. It should be pointed out that it does not consider corrosion inhibitor additives, crude oil chemistry and

steel surface state. To better explain the fundamentals of phase wetting and to predict internal corrosion, a Water Wetting Joint Industry Project (WW JIP) was initiated in 2006 and sponsored by eight major oil and gas companies (BP, ConocoPhillips, Eni, ExxonMobil, Petrobras, Saudi Aramco, Shell and Total). The main goal of the project is to answer two questions, First: where is the corrosive water in pipe flow? Second: how does the water interact with pipe inner wall? Five research topics were proposed and assigned to three Ph.D and two master students who worked in the WW JIP. The topics are: effects of corrosion inhibitors, general crude oil chemistry, asphaltenes, waxes and steel surface states on phase wetting and carbon dioxide corrosion in oil-water two-phase flow.

This dissertation focuses on the effect of corrosion inhibitor. It includes an experimental study of the phase wetting phenomenon carried out both in the large scale flow loop and a small scale apparatus, called doughnut cell, designed and developed by the present author. Two generic inhibitors, quaternary ammonium chloride (“quat”) and fatty amino compound, were investigated to look at their effect on corrosion inhibition, the changes of oil-water interfacial tension and wettability of the steel surface. The phase wetting prediction model was improved to better predict the onset of the oil wetting regime, which leads to corrosion free condition.

It should be pointed out that all the large scale flow loop experiments were conducted with the help from another two Ph.D. students in the project, Mr. Xuanping Tang and Mr. Francois Ayello and former project leader, Dr. Jiyong Cai. The experimental results obtained there are shared between the three Ph.D. students and

various aspects appear in their dissertations. With respect to model development, the background theory and ideas behind the models as well as most of the improvement were also shared between the students. However, each student had their own focus area. This study mainly focuses on the phase wetting transition from intermittent wetting (when the bottom of the pipe inner wall is alternatively wetted by the oil and water which leads to a corrosion situation) to oil wetting (corrosion free situation) and the effect of corrosion inhibitor on the phase wetting transition. Parts of the joint work on flow loop tests and model development have been published in SPE (Society of Petroleum Engineers) conference (Cai *et al.*, 2005a), NACE International conferences (Li *et al.*, 2006a; Tang *et al.*, 2006 and 2007; Ayello *et al.*, 2008b), and internal project report (Cai *et al.*, 2005b) delivered to the sponsor. Part of the individual work on corrosion inhibitor studies was published at the ICC (International Corrosion Congress) conference (Li *et al.*, 2008). In order to avoid confusion, all the text referring to the joint results which were published before are rewritten in this dissertation by the author.

## CHAPTER 2: LITERATURE REVIEW

A literature review was conducted with the main themes being carbon dioxide corrosion, oil-water two-phase flow and corrosion inhibition. The literature review below reflects the current understanding these areas and helps identify the gaps in the knowledge as it relates to this research topic.

### 2.1 Carbon dioxide corrosion

#### 2.1.1 Mechanisms of carbon dioxide corrosion

Carbon dioxide corrosion, also called sweet corrosion, involves the interactions between steel, water and CO<sub>2</sub>. In the light of common and expensive problems occurring in the oil and gas industry, carbon dioxide corrosion has been extensively studied in the past few decades. CO<sub>2</sub> corrosion was also referred to as “acid corrosion” due to the formation of weak carbonic acid and release of hydronium ion (H<sup>+</sup>) through several chemical reactions (2-1) to (2-4).



Compared to strong acids, such as hydrochloric acid (HCl) and sulfuric acid (H<sub>2</sub>SO<sub>4</sub>), which can completely dissociate in water, carbon acid is considered a weak acid, which dissociates only partially in water. However, experimental work shows that aqueous CO<sub>2</sub> leads to a higher corrosion rate than strong acid solutions at the same pH.

The aqueous CO<sub>2</sub> corrosion of carbon steel is an electrochemical process occurring at the steel surface. The overall reaction is given by:



A corrosion product, iron carbonate (FeCO<sub>3</sub>) forms in CO<sub>2</sub> corrosion, which can remain dissolved or precipitate on the steel surface. The electrochemical reactions include anodic (oxidation) and cathodic (reduction) reactions, which have been investigated extensively in the past.

The main anodic reaction is the dissolution of iron to give ferrous ions (2-6).



The mechanism and kinetics of iron dissolution proposed by Bockris *et al.* (1961) is:



An activated complex, FeOH is formed by reaction of iron and hydroxide ion (OH<sup>-</sup>). The rate determining step (RDS) is dependent on the FeOH concentration. It was found with experiments that the overall reaction order of iron dissolution (2-6) with respect to OH<sup>-</sup> is calculated as one, in range of pH 1 to 4.

de Waard and Milliams (1975a) adopted the mechanism of iron dissolution described above in their studies of carbonic acid corrosion. Experimental results in both HCl, 1 wt% NaCl and CO<sub>2</sub> saturated, 1 wt%. NaCl solutions confirmed that the anodic reaction rate is proportional to OH<sup>-</sup> concentration. Similar results were found by Schmitt

and Rothmann (1978b) in CO<sub>2</sub> containing NaSO<sub>4</sub> solution in the temperature range of 25°C to 75°C. They also found that the anodic reaction rate is independent of flow.

Research by Hurlen *et al.* (1984) showed that high purity iron has active, prepassive and passive regions at different potential ranges. CO<sub>2</sub> has little effect on anodic reaction of iron in active state. Davies and Burstein (1980) suggested that the formation of hydroxide, Fe(OH)<sub>2</sub>, and the complex,  $Fe(CO_3)_2^{2-}$  in the active and prepassive regions in bicarbonate solution control the anodic reaction of iron. Videm and Kvarekvaal (1996) and Videm (2000) found that the anodic reaction rate increases proportional to the OH<sup>-</sup> concentration and is independent of flow at pH less than 4.4. At pH greater than 4.4, the dissolution rate is independent of pH but increases with flow.

Nesic and Postlethwaite (1996a) found that in hydrochloric acid solution without purging CO<sub>2</sub> the reaction order of iron dissolution with respect to pH is one for pH between 3 and 4. Between pH 4 and 5, it decreases very little. While in CO<sub>2</sub> tests, it was found that the iron dissolution reaction is not affected by pH in the range of pH 4 to 6.

Two main cathodic reactions, (2-10) and (2-11), were proposed and adopted for CO<sub>2</sub> corrosion. Reaction (2-10) is the well known hydronium ion reduction, which is also the main cathodic reaction in strong acid corrosion without CO<sub>2</sub>. For fully dissociated strong acid, the hydronium ion reduction rate is highly dependent on bulk solution pH and mass transfer rate of hydronium ion from bulk solution to steel surface. Increasing pH from 3 to 4 in hydrochloric acid solution without CO<sub>2</sub>, the limiting current of cathodic reaction was found to be ten times lower. The limiting current is sensitive to flow as well as pH (Nesic and Postlethwaite, 1996a). In CO<sub>2</sub> environment carbonic acid (H<sub>2</sub>CO<sub>3</sub>) is a

reservoir of hydronium ions through two dissolution steps, (2-3) and (2-4). With the consumption of hydronium ions by cathodic reaction (2-10) and carbonic acid by chemical reactions, (2-3) and (2-4), dissolved CO<sub>2</sub> in solution becomes a reservoir of carbonic acid (2-2). Consequently, mechanism of the cathodic reaction of CO<sub>2</sub> corrosion has been thought to be hydronium ion reduction with additional sources of hydronium ions by the dissociation of carbonic acid. If this assumption was true it would be expected to find the same magnitude of flow dependent limiting current density in CO<sub>2</sub> solution as in strong acid solution. However, experimental findings by Schmitt and Rothman (1978a) and Nesic *et al.* (1996a) suggested that the limiting current of hydronium ion reduction is composed of two parts, a diffusion controlled H<sup>+</sup> and H<sub>2</sub>CO<sub>3</sub> reductions (flow sensitive) and a slow reaction controlled CO<sub>2</sub> hydration (flow insensitive).



The direct reduction of undissociated H<sub>2</sub>CO<sub>3</sub> on steel surface (2-11) was first proposed by de Waard and Milliams (1975a, 1975b) to explain why aqueous CO<sub>2</sub> solution is more corrosive than strong acid under the same pH. The subsequent recombination of the produced bicarbonate ions and hydronium ions, (2-3), can take place on steel surface to regenerate carbonic acid. According to the authors, reaction (2-11) is a rate determining step in cathodic reaction for aqueous CO<sub>2</sub> corrosion.

Schmitt and Rothman (1978a) found that the diffusion controlled limiting current component in the overall cathodic limiting current is composed of not only the hydronium ion diffusion rate, but also the undissociated carbonic acid diffusion rate,

which accounts for about 20% to 25% of the overall cathodic limiting current. The flow independent limiting current component was explained by the authors as chemical reaction rate controlled carbon dioxide hydration (2-2).

Gray *et al.* (1989) proposed the similar mechanism of cathodic reaction as Schmitt and Rothman (1978a). However, they concluded that the rate determining step is homogeneous CO<sub>2</sub> hydration rather than heterogeneous reaction related to CO<sub>2</sub> adsorption onto the steel surface proposed by Schmitt and Rothman (1978a). Gray *et al.* (1990) suggested that charge transfer controlled bicarbonate ions reduction (2-12) plays an important role in enhancing corrosion rate at pH of 6 to 10, where it falls out of the interested pH range for CO<sub>2</sub> corrosion.



Nesic and Postlethwaite (1996a) suggested that CO<sub>2</sub> corrosion cathodic limiting current can be controlled by one or more of the following steps: diffusion of H<sup>+</sup>, diffusion of H<sub>2</sub>CO<sub>3</sub> and hydration of CO<sub>2</sub>. At pH 5 or higher and lower potentials, water reduction (2-13) becomes the dominant reaction in both strong acid corrosion and CO<sub>2</sub> corrosion, which is under charge transfer control and insensitive to flow.



### 2.1.2 Factors affecting carbon dioxide corrosion

Having summarized the current understanding of CO<sub>2</sub> corrosion mechanisms, this section will discuss several important controlling factors of uniform CO<sub>2</sub> corrosion, which include water chemistry, temperature and flow. Localized corrosion caused by CO<sub>2</sub> is beyond the research scope and will not be discussed in this work.

### *Effect of water chemistry*

Water chemistry is a key component of CO<sub>2</sub> corrosion. It involves pH calculation, iron carbonate formation, and other types of scale formation. The main species produced by dissolved CO<sub>2</sub> in water are carbonic acid, hydronium ion, bicarbonate ion and carbonate ion. A list of common dissolved species and involved chemical reactions in oilfield formation water was summarized by Nordsveen *et al.* (2003) and Nesic (2007). Concentrations of species in solution can be calculated by solving chemical reaction equilibria with electroneutrality equation for open system (constant partial pressure of CO<sub>2</sub>) and/or conservation equation of carbonic species for closed system (varied partial pressure of CO<sub>2</sub>). With some known parameters, such as total pressure, partial pressure of CO<sub>2</sub> and temperature, aqueous solution pH can be calculated.

If the solubility limit,  $K_{sp}$ , is exceeded, precipitation of scale will occur. The most common scale for CO<sub>2</sub> corrosion is the formation of iron carbonate (2-14). Precipitation of iron carbonate on the steel surface can be protective and act as a diffusion barrier for corrosive species and have surface covering effect (Nordsveen *et al.* 2003). The most important leading factors of FeCO<sub>3</sub> scale formation are water chemistry and temperature. Supersaturation (S) is used to describe the scale formation tendency (2-15). If the supersaturation is less than one, the precipitation of FeCO<sub>3</sub> scale is impossible. When the supersaturation is greater than one, appreciable amount of FeCO<sub>3</sub> precipitation can occur.



$$S = \frac{c_{Fe^{2+}} c_{CO_3^{2-}}}{K_{sp}} \quad (2-15)$$

If supersaturations of various salts are achieved, other types of mineral scale deposition can occur on oilfield facilities possibly resulting in severe restriction of fluid flow and loss of efficiency. The common scales occurring in oilfields are calcium carbonate ( $\text{CaCO}_3$ ), calcium sulfate ( $\text{CaSO}_4$ ), barium sulfate ( $\text{BaSO}_4$ ), and strontium sulfate ( $\text{SrSO}_4$ ). Although these scales can give protection for steel from the corrosion perspective, they produce scaling and fouling problems from the flow assurance point of view. Scale inhibitors are commonly used in oilfield to inhibit mineral scales formation (Li, 2006b).

The formation water contains variable salt content depending on the field location. In some cases the salt content can be up to 20 wt% or higher. However, most of  $\text{CO}_2$  corrosion studies are conducted at 1 wt% to 3 wt% NaCl solutions, and no effect of salt concentration on uniform  $\text{CO}_2$  corrosion has been found in this range. Recently, a study conducted by Fang *et al.* (2006) with high salt content between 3 wt% to 25 wt% NaCl in water phase shows that uniform  $\text{CO}_2$  corrosion rate decreases with increasing salt concentration.

### ***Effect of temperature***

It would be expected that higher corrosion rate is achieved with increasing temperature due to the acceleration of electrochemical and chemical reactions and the transport rate of corrosive species in solution. On the other hand, an increase of temperature promotes the kinetics of  $\text{FeCO}_3$  scale formation, which can slow down the corrosion rate.

Experiments conducted by de Waard and Milliams (1975a) covered the temperature range from 5.5°C to 80°C. The changes of CO<sub>2</sub> partial pressure and solution pH due to increasing temperature were considered in their study. They calculated an activation energy of 10.7 kcal/mole for CO<sub>2</sub> corrosion. With this value, a worst case CO<sub>2</sub> corrosion rate can be calculated at any temperature from 5.5°C to 80°C. A good agreement was found between predicted corrosion rates and experimental values below 40°C. Above that temperature, experimental values are lower than predicted corrosion rates due to FeCO<sub>3</sub> scale built up on the test coupons. Gray *et al.* (1990) found a similar trend, *i.e.*, that CO<sub>2</sub> corrosion rate increases with increasing temperature from 25°C to 60°C, but becomes stable from 90°C to 125°C due to FeCO<sub>3</sub> scale formation.

Nesic *et al.* (1996a) confirmed using electrochemical measurements in solution without CO<sub>2</sub> that an increase in the diffusion coefficient for hydronium ions with increasing temperature results in an increase of cathodic limiting current, *i.e.*, higher corrosion rate. They also found from experiments with purging CO<sub>2</sub> in solutions that the CO<sub>2</sub> corrosion rate increases from 1 mm/yr at 20°C to 3 mm/yr at 80°C, even though the partial pressure of CO<sub>2</sub> decreases from 1 to 0.55 bar in the test temperature range.

### ***Effect of flow***

As discussed above, the limiting current of cathodic reaction includes a flow dependent component, diffusion of H<sup>+</sup> and H<sub>2</sub>CO<sub>3</sub>, and a flow independent part, hydration of CO<sub>2</sub>. There are two types of flow that needs to be discussed, single-phase and multiphase flow. For single-phase water flow, increasing flow velocity usually accelerates the corrosion rate, since it enhances mass transfer rate of corrosive species

from bulk solution to steel surface and corrosion product species away from steel surface to bulk solution. If  $\text{FeCO}_3$  scale or corrosion inhibitor film forms on the steel surface, flow may not have significant effect on uniform corrosion rate due to protective scale or inhibitor film. However, turbulent flow can mechanically remove the protective scale or film at high shear stress locations, such as valves, weld beads, bends and flanges.

For effect of multiphase flow on  $\text{CO}_2$  corrosion, both experimental and modeling work becomes more complex than for single-phase flow. The most significant difference between single-phase flow and multiphase flow has to do with flow patterns and phase wetting regimes. Since internal pipeline corrosion is associated with water wetting on the steel surface, if water is entrained in the flowing oil phase, corrosion can be substantially reduced or avoided. There has been little published in the literature, which has been done on the effect of phase wetting on  $\text{CO}_2$  corrosion in multiphase flow. Nesic *et al.* (2004 and 2008b) have published an integrated  $\text{CO}_2$ ,  $\text{H}_2\text{S}$  corrosion and multiphase flow prediction model. With a prediction of the multiphase flow pattern the model can determine the transition from corrosion condition to corrosion free condition. If water wets the pipe wall, the model calculates key hydrodynamic parameters, water layer thickness and velocity, these are required by the corrosion prediction model developed for single-phase flow.

### 2.1.3 Modeling of carbon dioxide corrosion

There are a large number of  $\text{CO}_2$  corrosion prediction models developed and used in the oil and gas industry. Some of them are mechanistic models based on a theoretical foundation, and others are empirical or semi-empirical correlations obtained from

laboratory or oilfield corrosion data. Semi-empirical models include partly a theoretical background and empirical models are not supported by corrosion or flow mechanisms. The most challenging part of building a mechanistic CO<sub>2</sub> corrosion model is to cover and explain all the physicochemical processes in CO<sub>2</sub> corrosion. In other words, answering “what it involves and how it happens?” is more important than writing and solving mathematical equations in the whole modeling process. Nyborg (2002) reviewed the basic backgrounds, performances and limitations of 16 selected CO<sub>2</sub> corrosion prediction models by evaluating model predictions with oilfield corrosion database information. Netic (2007) published a review paper of CO<sub>2</sub> corrosion prediction models. In the paper, the current understanding on mechanisms, important factors and modeling strategies of CO<sub>2</sub> corrosion were described.

The CO<sub>2</sub> corrosion prediction model developed and revised by de Waard and Milliams (1975a and 1975b), de Waard and Lotz (1993), de Waard *et al.* (1995) has been widely used in the oil and gas industry. The first version published in 1975, (2-16), in which  $V_{\text{corr}}$  (mm/yr) is corrosion rate and  $t$  (°C) is temperature,  $p_{\text{CO}_2}$  (bar) represents partial pressure of CO<sub>2</sub>, assumed that pH is only dependent on temperature and partial pressure of CO<sub>2</sub>. The model considers the direct reduction of H<sub>2</sub>CO<sub>3</sub> as cathodic reaction. The constants in the equation were determined by CO<sub>2</sub> corrosion experiments in a laboratory. The authors (de Waard and Milliams, 1975b) also presented a simple graphic form of the Equation (2-16) to “read” corrosion rate as a function of temperature and partial pressure of CO<sub>2</sub>.

$$\log V_{\text{cor}} = 7.96 - \frac{2320}{t + 273} - 5.55 \times 10^{-3} t + 0.67 \log p_{\text{CO}_2} \quad (2-16)$$

de Waard and Lotz (1993) extended the original model to account for effect of protective scales, flow velocity, oil/water wetting, glycol, *etc.* The model was improved by adjusting constants with more experimental data and adding empirical correction factors to (2-16). However, the model correction factors were generated by best fitting numerous field and laboratory corrosion data, which enables the model to explain their experimental results. It is not reliable to extrapolate the results for different conditions. The effect of crude oil was considered in their model by introducing an oil factor  $F_{oil}$ , as shown in (2-17). The factor is set to zero for crude oil velocity above 1 m/s in which case water can be entrained up to 30% water cut leading to oil wetting and corrosion free condition. This criterion was determined based on Lotz's (1990) experimental results.

$$F_{oil} = 0; \text{ if water cut } < 30\% \text{ and crude oil velocity } > 1\text{m/s}$$

$$\text{Otherwise } F_{oil} = 1 \quad (2-17)$$

The model (de Waard and Lotz, 1993) does not consider many key parameters, such as pipe diameter, inclination, oil/water properties and oil/water chemistry, which should be included in a mechanistic model. The effect of flow on mass transfer of corrosive species was added to the model by applying a resistance model (2-18), in which  $V_r$  (mm/yr) is electrochemical reaction rate and  $V_m$  (mm/yr) stands for mass transfer rate of  $H_2CO_3$ , which is dependent on diffusion coefficient, pipe diameter, flow velocity and kinematic viscosity of the fluid. The constants in calculation of key terms in resistance model were updated with a large number of flow loop experimental data (de Waard *et al.* 1995).

$$\frac{1}{V_{cor}} = \frac{1}{V_r} + \frac{1}{V_m} \quad (2-18)$$

de Waard *et al.* (2001) proposed a new way of calculating the oil factor, (2-19), in which  $W$  (%) denotes for water cut,  $\theta$  ( $^{\circ}$ ) is angle of pipe inclination,  $U_{oil}$  (m/s) represents superficial oil velocity and  $c_1$ ,  $c_2$ ,  $c_3$  are constants. It is based on water-in-oil emulsion breakpoint approach. Equation (2-20) shows that the emulsion breakpoint,  $W_{break}$  (%), was obtained by conducting a linear regression on the emulsion experiments with a range of crude oil from light to heavy (Craig, 1998). The three constants in (2-19) were determined by field data case by case. It makes this semi-empirical model hard to extrapolate, although the model considers water cut, pipe inclination, oil phase velocity and provides a link between crude oil API gravity and emulsion breakpoint.

$$F_{oil} = c_1 \frac{W}{W_{break}} U_{oil} + c_2 \frac{\theta}{90} + c_3 \frac{\theta}{90} \frac{W}{W_{break}} U_{oil} \quad (F_{oil} \leq 1) \quad (2-19)$$

$$W_{break} = -0.0166 \times API + 0.83 \quad (20 < API < 50) \quad (2-20)$$

Gray *et al.* (1989) developed a mechanistic  $CO_2$  corrosion prediction model based on analysis of electrochemical reactions at pH 4. The controlling step of corrosion rate was considered as hydration of  $CO_2$  in the model. Later Gray *et al.* (1990) extended the model to a wider range of pH 2 to 11 and temperature 25 to  $125^{\circ}C$  with more experiments. The direct reduction of bicarbonate ion was added into the model at high pH ( $>6$ ). The model did not consider water chemistry, protective scale formation, flow and oil wetting effects.

Pots (1995) developed a mechanistic Limiting Corrosion Rate (LCR)  $CO_2$  corrosion model which gives worse case corrosion rate prediction based on the mass transfer control assumption. The model has reasonable prediction at flow velocity of 1 m/s, but at higher flow velocity charge transfer replaces mass transfer as a controlling

step for corrosion rate. The author (Pots, 1995) also proposed a new coupled mass transport and electrochemical reactions approach by numerically solving a set of equations for mass transport, charge neutrality, chemical reactions, and electrochemical charge transfer kinetics. The protective  $\text{FeCO}_3$  scale formation and oil wetting effect were not considered in the model. The LCR model was used to predict corrosion rate in gas-liquid two phase flow, but only when flow pattern, liquid flow velocity, holdup, height of liquid layer are known from experiments or two-phase flow prediction model.

Nordsveen *et al.* (2003) published a mechanistic  $\text{CO}_2$  corrosion model including theory and model verification. The paper reviewed all the physicochemical processes underlying in  $\text{CO}_2$  corrosion, including chemical reactions, electrochemical reactions and transport processes. A set of equations were written based on the description of physicochemical processes. In light of complex and coupled equations, a finite difference numerical method was used to solve the mathematical equations. The comparison between model prediction and flow loop experiments revealed that a better agreement was achieved at high flow velocity, low temperature and low  $\text{CO}_2$  partial pressure. It also showed that the model needs to be improved in regards to the protective  $\text{FeCO}_3$  scale. The model considered the favorable conditions of  $\text{FeCO}_3$  scale formation and protective effect due to scale coverage and transport barriers. However it did not cover the scale formation kinetics and morphology. Nestic and Lee (2003) proposed a model of  $\text{FeCO}_3$  scale growth as a part of the development of mechanistic  $\text{CO}_2$  model (Nordsveen *et al.*, 2003). In the scale growth model, the precipitation rate of  $\text{FeCO}_3$  is controlled by temperature and local concentrations of scale formation species determined by transport

processes. The protectiveness of  $\text{FeCO}_3$  scale depends on the value of scaling tendency, the ratio of precipitation rate *versus* the corrosion rate.

There are  $\text{CO}_2/\text{H}_2\text{S}$  corrosion prediction models, which are proprietary models developed by companies and research institutes. One of those proprietary models is the software package called MULTICORP, which has been developed at the Institute for Corrosion and Multiphase Technology at Ohio University. MULTICORP covers most key aspects of  $\text{CO}_2/\text{H}_2\text{S}$ /organic acid corrosion in single-phase water flow and multiphase flow which are related to internal pipeline corrosion in the oil and gas industry (Nesic *et al.*, 2008b). As a proprietary software package, it is only available to sponsors. In 2008, a free and downloadable  $\text{CO}_2/\text{H}_2\text{S}$  corrosion prediction software, called FREECORP, was released by the Institute for Corrosion and Multiphase Technology at Ohio University (Nesic *et al.* 2008a). FREECORP was built as a user friendly Excel add-in function based on public knowledge of  $\text{CO}_2/\text{H}_2\text{S}$ , acetic acid and oxygen corrosion mechanisms. Even though it does not include multiphase flow prediction function, it can be easily linked to any multiphase flow prediction module/software since the program code of the FREECORP is available to the public.

#### 2.1.4 Carbon dioxide corrosion control strategies

A tremendous loss of oilfield production can occur due to internal pipeline corrosion ( $\text{CO}_2$ ,  $\text{H}_2\text{S}$  corrosion, *etc.*). For example, the pipeline failure accident in Alaska due to internal corrosion caused a 200,000 gallon, 1.9 acre oil spill and a shutdown of oilfield productions leading to U.S. domestic crude oil production falling by 8% (Jacobson, 2007). Carbon steel is a common construction material in oilfield facilities due

to lower cost than corrosion resistant alloys (CRAs), but with a poor corrosion resistance. Controlling CO<sub>2</sub> corrosion during production is essential for the use of carbon steel. One of the most common oilfield corrosion control strategies is using “carbon steel + corrosion allowance + corrosion inhibitor + corrosion monitoring” (Turgoose, 2004). The corrosion allowance is an added wall thickness in addition to the wall thickness required for operational pressure to achieve the designed service life (Kapusta *et al.*, 1999). The corrosion allowance can be determined by the pipeline desired service life time and predicted corrosion rate, which requires either reliable corrosion prediction model or past field experience. The correctly chosen value of corrosion allowance can assure pipeline integrity and save unnecessary costs. One example of a field case is that corrosion allowance was determined 3 mm thicker than actually required because of an inaccurate prediction of a corrosion model. It cost more than \$1 million US dollar for pipeline materials alone, which was not required, and higher cost of pipeline manufacture (Rippon and Simon Thomas, 2002).

If the predicted corrosion rate is high enough to require corrosion allowance over the predetermined limit (8 mm is often used as a limit), corrosion inhibitor should be considered to reduce the field corrosion rate. According to NACE, corrosion inhibitor is defined as “a substance which retards corrosion when added to an environment in small concentrations”. Among all the internal pipeline corrosion control methods, injection of corrosion inhibitor is most widely used because it is economical, highly effective and easily implemented in ppm concentration levels. Before corrosion inhibitor is applied in an oilfield, several inhibitors are evaluated and screened in small scale laboratory tests,

including not only corrosion inhibition performance, but also partitioning, foaming, compatibility, emulsion, stability and environmental effect. The injection concentration of inhibitor is determined by the laboratory tests with parameters close to field operation conditions. Inhibitor can be applied in continuous treatment or batch treatment based on field location, conditions and solubility of inhibitor.

Corrosion monitoring plays an important role in internal pipeline corrosion control management. It answers how corrosive the fluids are and at what rate steel has been corroded. Since the field fluids and operating conditions may vary with time during the production life, operators and corrosion engineers need to know the effectiveness of applied corrosion control methods. With those feedbacks, optimization of current control methods or the addition of new control method may be needed. The essential data collection includes some basic operational conditions, such as flow rate, pressure, and temperature. Fluid analysis should be further conducted and recorded for pH, acid gas compositions, ferrous ion count, and more detailed water chemistry. Some techniques are available for direct corrosion rate measurements, such as weight loss coupon, electrical resistance (ER) probe, and linear polarization resistance (LPR) probe. There are some limitations on each of the corrosion monitoring techniques. Several different monitoring techniques are usually used in oilfields. The corrosion monitoring data does not only give an early warning of corrosion problems, but it also helps to identify possible causes of corrosion failure or helps to provide information on future integrity management.

Other than chemical treatment with corrosion inhibitor, pH stabilizer has been used for corrosion control purposes. It lowers corrosion rate by increasing the solution pH

based on chemical reactions with acid species, whereas corrosion inhibitor inhibits corrosion by adsorption on the steel surface. Typical pH stabilizers are ammonia, caustic and amines. In CO<sub>2</sub> corrosion environments, these stabilizers increase the solution pH and further promote FeCO<sub>3</sub> scale formation on the steel surface (Halvorsen *et al.*, 2007). A potential problem, which can be introduced by pH stabilizer is the formation of other scales that can cause blocking of pipelines. Since the concentration of CO<sub>3</sub><sup>2-</sup> will be increased with increasing pH, precipitation of CaCO<sub>3</sub> can occur (Dugstad *et al.*, 2003).

Coating and cathodic protection have been successfully used for the protection of external pipeline corrosion. Internal coatings including plastic, fiberglass and CRA clad have been applied for the protection of internal carbon steel pipeline corrosion (Smith, 1999). However, plastic and fiberglass have limited success and are not recommended for aggressive environments, such as H<sub>2</sub>S, high temperature and high pressure. As an example, plastic coating on N-80 carbon steel pipelines failed in 19 months under H<sub>2</sub>S and high chloride concentration conditions (Smith, 1999). CRA clad tubing requires a special connection treatment for sealing. CRA solid tubing is suitable to use under severe corrosion conditions. However, localized corrosion and stress corrosion cracking are the most potential failure concerns of CRA solid tubing (Smith, 1999).

Crude oil has been known to act as a “natural inhibitor” in oilfield production to give lower corrosion rate than it is expected by corrosion model prediction or found by laboratory tests without considering crude oil effect. Crude oil can entrain corrosive water and prevent it from contacting with the steel surface directly. These hydrodynamic and wettability related issues were experimentally studied by Cai *et al.* (2005b). Another

effect is the direct corrosion inhibition by compounds present in crude oil, such as oxygen, sulfur and nitrogen containing compounds, which can adsorb on the steel surface either from the oil phase or from the water phase after partitioning to give corrosion protection (Ayello *et al.*, 2008a).

## **2.2 Oil-water two-phase pipe flow**

### **2.2.1 Characteristics of oil-water two-phase pipe flow**

Flows of hydrocarbon phase (oil) and aqueous phase (water), which are two immiscible liquids, are often referred to oil-water two-phase flow. The main difference between oil-water flow and gas-liquid flow is the small density contrast for oil-water flow (typically 0.7-1.1), but large density contrast for gas-liquid flow (typically 0.001-0.2) (Simmons and Azzopardi, 2001). The main difference between multiphase flow and single-phase flow is the occurrence of various flow patterns and phase wetting scenarios in multiphase flow. Flow pattern refers to the macroscopic spatial distribution of phases in the pipe and phase wetting refers to the microscopic contact of phases with the pipe wall. These two terms are correlated with each other and are both affected by parameters such as flow rate of each phase, pipe diameter and inclination, and the physical properties of the fluids (density, viscosity, surface tension and interfacial tension). A large number of research studies have been done and published on the topic of oil-water two-phase flow in order to develop and improve predictions of flow patterns.

### ***Flow pattern***

Various names of flow patterns in oil-water two-phase pipe flow have been seen in the literature due to different terminologies, different test liquids used in the experiments and other test system effects, such as pipe diameter, inclination, type of pump, type of liquid mixer, with/without separator, *etc.* Identification of flow patterns was mainly based on visual observation (Russell *et al.*, 1959; Charles *et al.*, 1961; Trallero, 1995; Nadler and Mewes, 1997; Angeli and Hewitt, 2000; Oddie *et al.*, 2003; Wegmann and von Rohr, 2006; Rodriguez and Oliemans 2006; Li *et al.*, 2006;), differential pressure transducer (Russell *et al.*, 1959; Charles *et al.*, 1961; Kurban *et al.*, 1995; Trallero, 1995; Nadler and Mewes, 1997; Valle and Utvik, 1997; Oddie *et al.*, 2003; Rodriguez and Oliemans, 2006), traversing conductance probes (Valle and Utvik, 1997), wall conductance probes (Trallero, 1995; Oddie *et al.*, 2003), high frequency impedance probe (Kurban *et al.*, 1995; Vigneaux *et al.*, 1998; Angeli and Hewitt, 2000; Oddie *et al.*, 2003), sampling tubes (Fairuzov *et al.*, 2000; Shi, 2001) and densitometer (Valle and Utvik, 1997; Oddie *et al.*, 2003; Rodriguez and Oliemans, 2006). An important term used for flow pattern transition of oil-water two-phase flow is called phase inversion. The original dispersed phase becomes a continuous flowing phase when the concentration of this phase reaches a critical point and the original continuous flowing phase changes to a dispersed phase (Shi, 2001).

Russell *et al.* (1959) observed three typical flow patterns: stratified, mixed and bubble flow in a horizontal, 1 inch internal diameter (ID) transparent plastic pipe. The test fluids were mineral oil with density of 834 kg/m<sup>3</sup> and viscosity of 18 cp and water.

Charles *et al.* (1961) selected three mineral oils with viscosities of 6.29 cp, 16.8 cp and 65 cp and added carbon tetrachloride into the oils to achieve the same density as the water phase. The equal density oil-water combination was tested in a horizontal, 1 inch ID pipeline. Five different flow patterns, which were identified, can be summarized as water-dispersed-in-oil, oil-dispersed-in-water and annular flows.

Kurban *et al.* (1995) carried out experimental study of oil-water two-phase flow in a horizontal, 1 inch ID acrylic flow rig. The test oil phase has density of  $800 \text{ kg/m}^3$ , viscosity of 1.6 cp and oil-water interfacial tension of 17 dyne/cm. Four flow patterns of stratified oil-water, stratified water-mixing layer, mixed and stratified mixing layer-oil flows were reported in their work. The thicknesses of liquid layers in stratified flows were measured by using the high frequency impedance probe. In dispersed flows the sizes and distribution of water droplets were measured with conductance probes and flow pattern visualization.

Trallero (1995) reviewed the past works on flow pattern determination and attempted to reclassify flow pattern terminology. He conducted oil-water two-phase flow in a horizontal, 2 inch ID flow loop. The test mineral oil has density of  $884 \text{ kg/m}^3$ , viscosity of 28.8 cp and oil-water interfacial tension of 36 dyne/cm. Based on his work and literature, six flow patterns (Figure 1) were summarized as two main categories: segregated flow and dispersed flow. Segregated flow includes stratified flow and stratified flow with mixing at the interface. An oil-dispersed-in-water layer on a water layer, an emulsion of oil in water, an emulsion of water in oil and a water-dispersed-in-oil over an oil-dispersed-in-water belong to a dispersed flow pattern category.

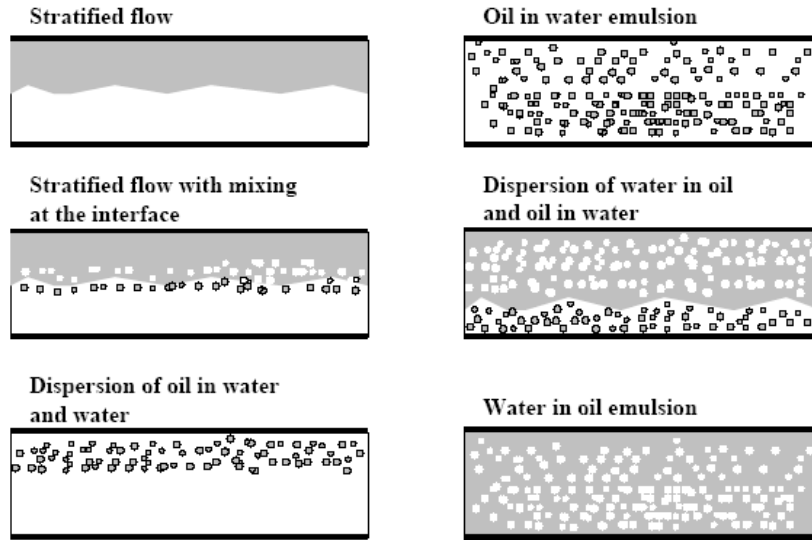


Figure 1 Six oil-water two-phase flow patterns proposed by Trallero (1995). The light color phase represents water phase and the dark color phase is for the oil phase.

Nadler and Mewes (1997) carried out an oil-water two-phase flow experimental investigations in a horizontal, 2.3 inch ID acrylic pipe. The viscosity of the mineral oil was changed in the range of 22 to 35 cp by changing the system temperature. Their results have a good agreement with six flow patterns found by Trallero (1995).

Valle and Utvik (1997) conducted several experiments in a horizontal, 3 inch ID flow loop with a light crude oil with density of  $741 \text{ kg/m}^3$  and viscosity of 1 cp and synthetic formation water. The water cut in the experiments was gradually increased from 0% to 100% at constant mixture velocity of 1.17, 1.74 and 2.33 m/s, respectively. They found that water-in-oil dispersed layer at bottom with oil continuous layer at top (called dispersed oil continuous flow) forms below 40-45% water cut. Above 40-45% water cut, oil cannot further hold up the dispersed water phase, which leads to oil and water stratified flow. In a transition zone between two flow patterns, an unstable layer was

detected between continuous oil layer and continuous water layer defined as stratified flow with mixing at the interface (Trallero, 1995).

Fairuzov *et al.* (2000) carried out oil-water two-phase flow in a horizontal, 16 inch ID pipeline. The test light crude oil has density of  $851 \text{ kg/m}^3$  and viscosity of 0.5 cp. Stratified flow, stratified flow with mixing layer and dispersed flow were identified in their tests, same as two main categories proposed by Trallero (1995). However, no attempt was made to classify different stratified and dispersed flows in their study. Angeli and Hewitt (2000) studied kerosene with density of  $801 \text{ kg/m}^3$ , viscosity of 1.6 cp and oil-water interfacial tension of 17 dyne/cm and tap water in a horizontal, 1 inch ID flow loop. They proposed four main flow patterns which were consistent with flow patterns found by Trallero (1995), but the names of the flow patterns were different.

Wegmann and von Rohr (2006) conducted two-phase flow of water and paraffinic oil in a horizontal, 0.276 inch (7mm) ID glass flow loop. The test oil has density of 818-820.5  $\text{kg/m}^3$  and viscosity of 4.3-5.2 cp according to changes of test temperature. Fluorescein sodium salt was added into the deionized water phase. With an Argon-Ion laser light, the color of the water phase became to green to enhance the contrast between oil and water. Four flow patterns were proposed: stratified, intermittent, annular dispersed and dispersed flows. However, due to their research interests, the experiments were only done in a small diameter pipe where the pipe wall may affect flow patterns.

Rodriguez and Oliemans (2006) employed oil-water two-phase flow in a horizontal and slightly inclined ( $\pm 5^\circ$ ), 3 inch ID stainless steel flow loop. The test fluids were mineral oil with density of  $830 \text{ kg/m}^3$ , viscosity of 7.5 cp and oil-water interfacial

tension of 20.4 dyne/cm and brine. The flow patterns observed in their tests are in agreement with those proposed by Trallero (1995). The only difference is that stratified wavy flow replaces stratified smooth flow with pipe inclination.

### ***Water wetting and water entrainment***

CO<sub>2</sub> corrosion in oil-water two-phase flow is highly dependent on the actual area of pipe wall wetted by corrosive water. Water wetting refers to the bottom of the pipe continuously wetted by the water phase. If entrainment of all the water phase into the flowing oil phase is achieved, which occurs under certain flow conditions, it is termed oil wetting, which may greatly reduce the CO<sub>2</sub> corrosion rate. In the open literature, only a few research studies on water wetting and water entrainment can be found.

Wicks and Fraser (1975) concluded that there is a critical oil velocity for water entrainment, which increases with pipe diameter. The water entrainment starts with water droplets in the oil phase in the transition region from stratified wavy flow to water-in-oil dispersed flow. The observations in solid-liquid and liquid-liquid flows confirmed the theory of the maximum droplet size proposed by Hinze (1955). According to the theory, the maximum size of water droplets that the oil flow can sustain before the water falls out of dispersion is related to the oil and water density, oil viscosity, oil-water interfacial tension, pipe diameter and flow velocity. The authors proposed a simplified model to calculate the critical oil velocity for water entrainment based on maximum water droplet size calculation and empirical correlation of the minimum velocity for particles transport. Several field cases with observations of internal pipeline corrosion were examined with

the model. The predictions showed that water entrainment was unlikely in the oilfields according to known operating conditions and fluid properties.

Wu (1995) improved the water entrainment model proposed by Wicks and Fraser (1975). She proposed three flow patterns which are stratified, stratified-dispersed and fully dispersed flows in relation to water entrainment. The calculations of the maximum water droplet size proposed by Hinze (1955) and a transition criterion from stratified flow to stratified-dispersed flow proposed by Brauner and Maron (1992) were adopted by the author to calculate the critical droplet size for entrainment. The author also pointed out that the wettability of steel surface and the surface roughness plays an important role in water wetting. The contact angle of a water droplet on steel surface, which is immersed in an oil phase, was illustrated for the purpose of wettability in her work.

Smith *et al.* (1987) brought up a simple rule of thumb that crude oil could entrain and carry water up to 20% by volume if oil flow velocity is greater than 1 m/s. It was proposed based on the corrosion rate observations of field cases. The rule overlooked many important parameters, such as oil and water properties, pipe diameter, *etc.* A later study by Craig (1998) proved that crude oils of different densities and viscosities have a different capacity for carrying water phase. He proposed an emulsion breakpoint concept to estimate corrosiveness of oil-water mixture by calculating conductivity of water-in-oil emulsion. At low water cut, the conductivity of oil-water mixture is strongly dependent on oil viscosity. Once water-in-oil emulsion forms, corrosion is controlled by the rate of water molecules coalescing to wet the steel surface as fine droplets. de Waard *et al.*

(2001) updated the calculation of oil factor in their CO<sub>2</sub> corrosion model by using the oil-water emulsion breakpoint concept.

Adams *et al.* (1993) mentioned the phase behavior of the fluids in modeling of tubing life. They estimated three kinds of phase behavior based on water cut. Oil wetting and reduced corrosion rate are achieved at water cut below 30%. Between 30% to 50% water cut, intermittent wetting occurs. At water cut above 50%, there is always water wetting in tubing, no matter the values of flow velocity, pipe diameter, oil properties. Obviously, the rule is still empirical and oversimplified the water entrainment criterion. Furthermore, the field experience indicated that water wetting and entrainment is a complex problem, since corrosion can occur when the water cut is as low as 1%, and in another case no severe corrosion is observed for water cut as high as 50% (Craig, 1998).

Papavinasam *et al.* (2007) studied the effect of oil on corrosion according to a developed laboratory methodology by testing 14 hydrocarbons collected from field pipelines. The authors concluded that the effect of oil on corrosion can be identified by types of emulsion (water-in-oil and oil-in-water), wettability (oil, water and mixed wets) and corrosiveness of brine in the system. The emulsion phase inversion points are in the range of 0 to 40% water cut for 14 different hydrocarbons tested. The wettability tests indicated that the clean steel surface is hydrophilic in the oil-water two-phase system. No correlation was found to link the corrosion inhibition by the presence of oil with the density and viscosity of the oil phase.

Pots *et al.* (2006) reviewed the factors in multiphase flow, which can affect internal pipeline corrosion. Modeling, field testing, laboratory flow loop and small scale

apparatus testing of water entrainment or breakout were also discussed by the authors. In their opinion, there will not be a model including all the affected parameters that give a definite answer for field application.

### 2.2.2 Modeling of oil-water two-phase flow

A number of models have been developed to predict multiphase flow patterns, which are not being considered here. The main focus in this section is to review the modeling of water entrainment and breakout in oil-water two-phase pipe flow. If water breakout occurs, the predictions of important hydrodynamic parameters related to corrosion rate calculation, such as water layer thickness, water phase velocity and shear stress are also reviewed.

Empirical rules (Smith *et al.*, 1987; Adams *et al.*, 1993) or models (Wicks and Fraser, 1975; Wu, 1995; de Waard *et al.*, 2001) have a lot of limitations, even though they can help to determine the likelihood of water entrainment and breakout in a qualitative sense. In this work, a mechanistic phase wetting prediction model is proposed to predict the transition between water breakout and water entrainment. The model is developed based on the extension and modification of modeling work done by Barnea (1986 and 1987), Brauner (2001), Cai *et al.* (2004) and Vedapuri *et al.* (1997). In the following two sections, a detailed review of the water entrainment and water breakout based models found in the open literature will be introduced and explained.

#### ***Water entrainment***

Water entrainment means that the water is dispersed and carried by the flowing oil phase as droplets. It is essential to determine the maximum water droplet size that can

exist in the turbulent flow without further breakup into smaller droplets. The bigger the water droplet size is, the lower is the tendency of droplets to be sustained in a horizontal flow since the gravity force tends to separate water out of the oil and; the force required to do this is proportional to droplet size. Most of the models for calculating maximum gas bubble size in gas-liquid flow and maximum liquid droplet size in liquid-liquid flow are built on the theory proposed by Hinze (1955).

Hinze (1955) showed that a maximum droplet/bubble size ( $d_{\max}$ ) in turbulent flow depends on the critical Weber number (2-21), which is defined as the ratio between the external shear force ( $\tau$ ) and the countering droplet/bubble interfacial tension force ( $\sigma$ ). In the case of water entrainment in turbulent oil flow, the external shear force, which tends to deform a droplet, is the turbulent kinetic energy ( $\frac{1}{2}\rho u'$ ) coming from turbulent eddies over a distance equal to the droplet diameter. The turbulent kinetic energy used to break up a droplet is proportional to the droplet surface energy ( $\frac{\sigma}{d_{\max}}$ ). It should be pointed out that Equation (2-22) considers the energy balance on a single droplet. The assumption is that the concentration of the dispersed phase (dilute dispersion) is low enough to have little effect on coalescence of the dispersed droplets. Equation (2-22) can be written in the form of Equation (2-23), in which  $k_1$  represents the percentage of turbulent kinetic energy in a balance with surface energy of the droplet. The subscript letter c in the equations represents continuous phase and the subscript letter d denotes for dispersed phase.

$$(N_{We})_{crit} = \frac{\tau * d_{max}}{\sigma} \quad (2-21)$$

$$\rho_c u'^2 \propto \frac{\sigma}{d_{max}} \quad (2-22)$$

$$k_1 \rho_c u'^2 = \frac{\sigma}{d_{max}} \quad (2-23)$$

The turbulent kinetic energy resulting from dynamic pressure fluctuations is related to the mean square of the velocity fluctuations ( $u'^2$ ) within turbulent eddies. The turbulent energy dissipation rate (per unit mass and unit time),  $e$ , can be calculated as Equation (2-24) or Equation (2-25) (Hinze, 1955), in which  $m_c$  is the mass flow rate of the continuous phase and the value of the constant  $k_3$  was proposed as 2, according to Batchelor (1951). The eddy length scale,  $l_k$ , is set equal to the maximum droplet size (2-26), by assuming the deforming is more effective when the size of an eddy is the same as the droplet diameter. Substituting Equations (2-25) and (2-26) into (2-23) gives Equation (2-27), in which the constant,  $k_4$ , equal to 0.725 was determined by Brauner (2001) from liquid-liquid emulsion experimental data of Clay (1940). For a pipe flow, the turbulent energy dissipation rate,  $e$ , (2-29) is related to the pressure drop,  $\Delta P$ , (2-28), where  $L$  is pipe length,  $D$  is pipe diameter,  $\varepsilon_c$  is percentage of continuous phase,  $\rho_c$  is continuous phase density and  $U_c$  is continuous phase velocity.

$$e = \frac{[energy\ input]}{[mass] * [time]} = \frac{k_2 m_c u'^2}{m_c \frac{l_k}{u}} = k_2 \frac{u'^3}{l_k} \quad (2-24)$$

$$u'^2 = k_3 (e \cdot l_k)^{2/3} \quad (2-25)$$

$$l_k = d_{max} \quad (2-26)$$

$$d_{\max} \left( \frac{\rho_c}{\sigma} \right)^{0.6} e^{0.4} = k_4 = 0.725 \quad (2-27)$$

$$\frac{1}{4} \pi D^2 \cdot \Delta P = \pi D L \cdot \tau \quad (2-28)$$

$$e = \frac{[\text{pressure drop}] * [\text{volume}]}{[\text{mass}] * [\text{time}]} = \frac{\frac{4L \cdot \tau}{D} * \frac{1}{4} \pi D^2 L}{\frac{1}{4} \pi D^2 L \varepsilon_c \rho_c * \frac{L}{U_c}} = \frac{4U_c \tau}{D \varepsilon_c \rho_c} \quad (2-29)$$

By inserting Equation (2-30) and Equation (2-31), in which  $f$  is fiction factor,  $\rho_m$  is oil-water mixture density and  $\varepsilon_d$  is percentage of dispersed phase, into Equation (2-29), it comes Equation (2-32), which substituted into Equation (2-27), Hinze's (1955) maximum droplet size model becomes Equation (2-33).

$$\tau = \frac{1}{2} f \rho_m U_c^2 \quad (2-30)$$

$$\varepsilon_c = 1 - \varepsilon_d \quad (2-31)$$

$$e = \frac{2U_c^3 f}{D} \frac{\rho_m}{\rho_c (1 - \varepsilon_d)} \quad (2-32)$$

$$d_{\max}^{dilute} = 0.725 \left( \frac{\rho_c}{\sigma} \right)^{-0.6} \left( \frac{2U_c^3 f}{D} \right)^{-0.4} \left[ \frac{\rho_m}{\rho_c (1 - \varepsilon_d)} \right]^{-0.4} \quad (2-33)$$

Since only a single droplet was considered in the turbulent flow, the Hinze model (1955) is only valid at low concentrations of the dispersed phase (named dilute dispersions by Brauner, 2001), not accounting for droplet coalescence. In homogeneous turbulence, the percentage of dispersed phase,  $\varepsilon_d$  (2-35), is determined by the superficial velocities of the dispersed and continuous phases,  $U_d$  and  $U_c$  (2-34).  $Q_d$  and  $Q_c$  are the

volume flow rate of the dispersed and continuous phases. The mixture density,  $\rho_m$  (2-36), is determined by the density of each phase and the percentage of dispersed phase.

$$U_c = \frac{Q_c}{A}; U_d = \frac{Q_d}{A} \quad (2-34)$$

$$\varepsilon_d = \frac{U_d}{U_d + U_c} \quad (2-35)$$

$$\rho_m = \varepsilon_d \rho_d + (1 - \varepsilon_d) \rho_c \quad (2-36)$$

The friction factor,  $f$ , can be calculated from the Blasius Equation (2-37) for a smooth pipe flow, in which the Reynolds number of the continuous phase is calculated from (2-38). A universal correlation, Equation (2-39), proposed by Colebrook (1939), which is suitable for both smooth and rough pipes can be used.  $K/D$  in (2-39) is relative roughness for the pipe wall. Equation (2-39) is implicit, which makes the solving process more complex due to iterations or the need for using Moody's diagram. Haaland (1983) proposed a simplified, explicit correlation (2-40) for the friction factor. Guet *et al.* (2006) used Haaland's (1983) correlation to extend the Hinze's model (1955) for the effect of pipe roughness on the maximum droplet size calculation.

$$f = \frac{0.046}{\text{Re}_c^{0.2}} \quad (2-37)$$

$$\text{Re}_c = \frac{\rho_c D U_c}{\mu_c} \quad (2-38)$$

$$\frac{1}{\sqrt{f}} = -2 \log \left( \frac{2.51}{\text{Re} \sqrt{f}} + \frac{K}{3.7D} \right) \quad (2-39)$$

$$\frac{1}{\sqrt{f}} = -1.8 \log \left[ \frac{6.9}{\text{Re}} + \left( \frac{K}{3.7D} \right)^{1.11} \right] \quad (2-40)$$

Brauner (2001) extended the Hinze model (1955) to account for dispersed droplet coalescence at higher concentrations of dispersed phase (called dense dispersions). Under such condition, the total surface energy of the dispersed droplets can be calculated with the cross sectional area of the droplet ( $\pi d_{\max}^2$ ), interfacial tension ( $\sigma$ ) and number of dispersed droplets ( $\frac{Q_d}{\pi d_{\max}^3 / 6}$ ), as shown in Equation (2-41). The total surface energy of the dispersed phase is proportional to the total turbulent kinetic energy provided by the continuous phase (2-42). The constant,  $C_H$ , which represents the percentage of total turbulent kinetic energy used for droplet breakup to counter the total surface energy from every dispersed droplet, is set as one.

$$E_s = \pi d_{\max}^2 \cdot \sigma \cdot \frac{Q_d}{\pi d_{\max}^3 / 6} = \frac{6\sigma}{d_{\max}} Q_d \quad (2-41)$$

$$\frac{\rho_c u'^2}{2} Q_c = C_H \frac{6\sigma}{d_{\max}} Q_d \quad (2-42)$$

Substituting (2-25) and (2-32) into (2-42) gives Equation (2-43), the maximum droplet size calculation for dense dispersions. Brauner (2001) suggested that the maximum droplet size of the dispersed phase (2-44) is the largest one of the two calculated values from dilute (2-33) and dense (2-43) dispersions.

$$d_{\max}^{dense} = 2.22 \left( \frac{\rho_c U_c^2}{\sigma} \right)^{-0.6} \left( \frac{\varepsilon_d}{1 - \varepsilon_d} \right)^{0.6} \left[ \frac{\rho_m}{\rho_c (1 - \varepsilon_d)} f \right]^{-0.4} D^{0.4} \quad (2-43)$$

$$d_{\max} = \text{Max} \left( d_{\max}^{dilute}, d_{\max}^{dense} \right) \quad (2-44)$$

Barnea (1986 and 1987) presented methods for the calculation of two critical bubble sizes for gas-liquid two-phase flow. The methods were adopted by Brauner (2001) for liquid-liquid two-phase flow. One of two droplet sizes,  $d_{cg}$ , is the critical size above which the dispersed droplet migrates toward the bottom of pipe and separates out from the continuous phase due to gravity, and is dominant in horizontal or near-horizontal flows. The radial component of gravity and turbulent fluctuations acting on a dispersed droplet (Figure 2) is calculated in Equation (2-45) and (2-46), respectively. The turbulent velocity fluctuations in radial direction,  $v'$ , can be empirically estimated to be equal to the friction velocity,  $U_*$ , which is calculated by (2-47) according to Barnea (1986). A force balance of these two forces ( $F_g = F_t$ ) gives Equation (2-48) for the critical droplet size,  $d_{cg}$ . It was called “creaming” by Barnea (1986) and Brauner (2001), since the equation was initially generated for gas bubbles arising in continuous liquid phase toward the upper wall of pipe due to buoyancy.

$$F_g = \frac{\pi d_{cg}^3}{6} |\rho_d - \rho_c| g \cos \beta \quad (2-45)$$

$$F_t = \frac{\pi d_{cg}^2}{4} \cdot \frac{1}{2} \rho_c v'^2 \quad (2-46)$$

$$v' = U_* = U_m \left( \frac{f}{2} \right)^{0.5} \quad (2-47)$$

$$d_{cg} = \frac{3}{8} \frac{\rho_c U_m^2 f}{|\rho_d - \rho_c| g \cos \beta} \quad (2-48)$$

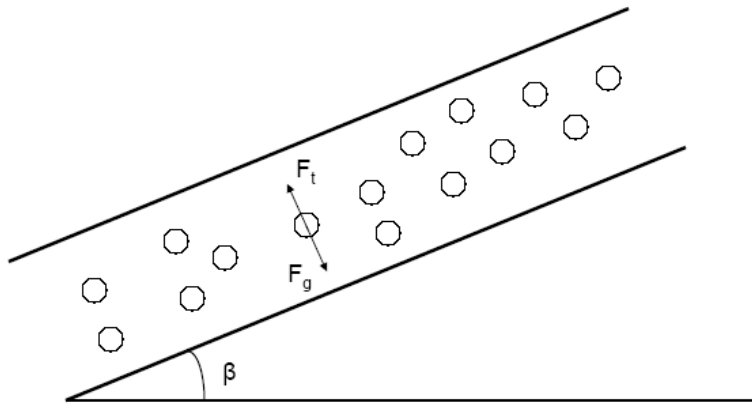


Figure 2 Force analysis on a dispersed droplet in the continuous flowing phase.  $F_g$  – radial component of gravity acting on the droplet,  $F_t$  – radial component of turbulent velocity fluctuations acting on the droplet and  $\beta$  – pipe inclination.

Another critical droplet size,  $d_{cd}$ , represents a size above which the droplet will be distorted from a spherical shape. The dispersed droplets are treated as rigid, spherical shapes over a range of diameters. If the droplet size is large enough to allow distortion and agglomeration to occur, swerving motion and coalescence of the droplets is enhanced. This is dominant in vertical or near-vertical flows. The oscillation of rising (upward inclined flow) or falling (downward inclined flow) flattened droplets leads the droplets to be pushed toward the pipe wall. Brodkey (1969, p.584) found that Equation (2-49) proposed by Bond and Newton (1928) for a dispersed droplet circulating in a continuous phase is good for establishing the onset of droplet distortion and swerving. Brauner (2001) added the effect of pipe inclination into the criteria, as shown in Equation (2-50). However, Brauner (2001) claimed that the term  $(\cos\beta)^{0.5}$  is not critical because the inclination effect is of the same order of uncertainty in the constant, 0.4, in Equation (2-49), which was determined by fitting experimental data of different gas-liquid and

liquid-liquid systems (Bond and Newton, 1928). Barnea (1987) suggested that the critical droplet size of the dispersed phase (2-51) is the smallest one of the two calculated values from the effects of gravity (2-48) and distortion (2-50).

$$d_{cd} = \left( \frac{0.4\sigma}{|\rho_d - \rho_c|g} \right)^{0.5} \quad (2-49)$$

$$d_{cd} = \left( \frac{0.4\sigma}{|\rho_d - \rho_c|g \cos \beta'} \right)^{0.5} \quad (2-50)$$

$$\text{with } \beta' = \begin{cases} |\beta|, & |\beta| < 45^\circ \\ 90^\circ - |\beta|, & |\beta| > 45^\circ \end{cases}$$

$$d_{crit} = \text{Min}(d_{cg}, d_{cd}) \quad (2-51)$$

A transition criterion (2-52) between the water breakout and the full water entrainment in oil-water two-phase flow is proposed by Brauner (2001).

$$d_{\max} \leq d_{crit} \quad (2-52)$$

This means that full water entrainment takes place when the maximum water droplet size,  $d_{\max}$ , in the continuous turbulent oil phase is equal to or smaller than the critical droplet size,  $d_{crit}$ . Otherwise, water breakout occurs. With the input of pipe diameter, inclination, oil/water properties (density, viscosity and interfacial tension), oil phase velocity, water cut and equations (2-33, 2-43, 2-44, 2-48, 2-50, 2-51), the criterion outlined in (2-52) can answer if complete water entrainment is achieved. The values of constants in the equations, 0.725 in (2-33), 2.22 in (2-43), 0.375 in (2-48) and 0.4 in (2-50), were determined from the empirical correlations or adapted to fit the experimental data.

### ***Water breakout***

If the turbulence in the oil phase is insufficient to entrain all the water phase, water breakout occurs and the water flows separately from the oil phase. From the point of view of internal pipeline corrosion prediction, it is essential to know the *in situ* water velocity and the water layer thickness, which is used to calculate the wall shear stress and the area of pipe inner wall wetted by the water, respectively. This section reviews a three-layer stratified flow model that predicts these parameters.

Taitel *et al.* (1995) proposed a mechanistic three-layer flow model for gas-oil-water three-phase stratified flow to predict the thickness of the gas, oil and water layers. Vedapuri *et al.* (1997) applied this three-layer flow model for oil-water stratified flow with mixing layer (see Figure 3) to calculate the thickness of water layer and the mixing layer. The model prediction had a good agreement with their experimental data of horizontal and inclined, 4 inch pipe flow.

Figure 4 is a schematic of the three-layer stratified flow, in which  $A_O$ ,  $A_M$ ,  $A_W$  are the cross sectional areas of flow,  $S_O$ ,  $S_M$ ,  $S_W$  are the wetted perimeters,  $\tau_O$ ,  $\tau_{i1}$ ,  $\tau_{i2}$ ,  $\tau_W$  are the shear stress,  $U_O$ ,  $U_M$ ,  $U_W$  are the superficial velocities, subscripts o, m, w denote oil layer, mixed layer, water layer, and subscripts *i1* and *i2* denote the interfaces of water layer-mixed layer and mixed layer-oil layer.

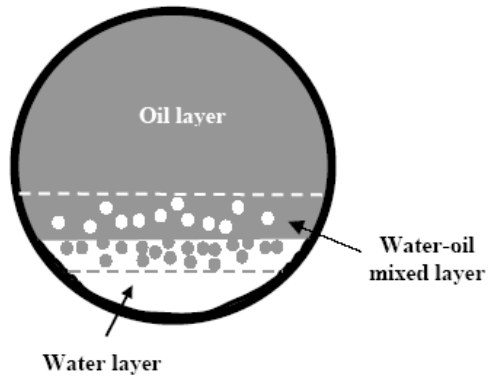


Figure 3 Cross section view of the three-layer stratified oil-water two-phase pipe flow (Cai et al., 2004).

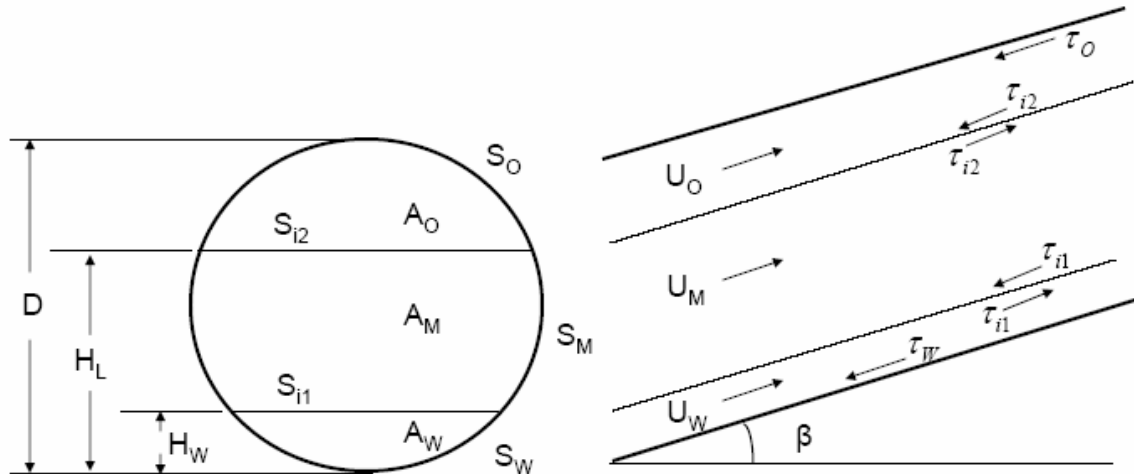


Figure 4 Schematic of oil-water three-layer stratified flow.

Momentum balances for the water layer (2-53), the mixing layer (2-54) and the oil layer (2-55) are carried out assuming only axial motion for each layer with no slip at the interfaces. In the equations,  $dp/dx$  denotes the pressure gradient, which is the same in different layers at given location. Eliminating the pressure gradient term by combining (2-53) and (2-54), (2-54) and (2-55), the following Equations (2-56) and (2-57) can be derived. The wall shear stresses and interfacial shear stresses are calculated by using

Blasius type Equation as shown in (2-58) and (2-59) (Taitel *et al.*, 1995). The friction factors for wall shear stresses,  $f_w, f_M, f_o$ , are evaluated by Equation (2-60) (Taitel *et al.*, 1995). The interfacial friction factors,  $f_{i1}, f_{i2}$ , (2-61) are set as equal the wall friction factors of the faster phases (Brauner and Maron, 1989).

$$-A_w \left( \frac{dp}{dx} \right) - \tau_w S_w + \tau_{i1} S_{i1} - \rho_w A_w g \sin \beta = 0 \quad (2-53)$$

$$-A_M \left( \frac{dp}{dx} \right) - \tau_M S_M - \tau_{i1} S_{i1} + \tau_{i2} S_{i2} - \rho_M A_M g \sin \beta = 0 \quad (2-54)$$

$$-A_o \left( \frac{dp}{dx} \right) - \tau_o S_o - \tau_{i2} S_{i2} - \rho_o A_o g \sin \beta = 0 \quad (2-55)$$

$$\tau_M \frac{S_M}{A_M} - \tau_w \frac{S_w}{A_w} - \tau_{i2} \frac{S_{i2}}{A_M} + \tau_{i1} \left( \frac{S_{i1}}{A_M} + \frac{S_{i1}}{A_w} \right) + (\rho_M - \rho_w) g \sin \beta = 0 \quad (2-56)$$

$$\tau_o \frac{S_o}{A_o} - \tau_M \frac{S_M}{A_M} - \tau_{i1} \frac{S_{i1}}{A_M} + \tau_{i2} \left( \frac{S_{i2}}{A_M} + \frac{S_{i2}}{A_o} \right) + (\rho_o - \rho_M) g \sin \beta = 0 \quad (2-57)$$

$$\tau_w = f_w \frac{\rho_w U_w^2}{2}, \quad \tau_M = f_M \frac{\rho_M U_M^2}{2}, \quad \tau_o = f_o \frac{\rho_o U_o^2}{2} \quad (2-58)$$

$$\tau_{i1} = f_{i1} \frac{\rho_w (U_M - U_w)}{2} |U_M - U_w|, \quad \tau_{i2} = f_{i2} \frac{\rho_o (U_o - U_M)}{2} |U_o - U_M| \quad (2-59)$$

$$f_w = \frac{0.046}{\text{Re}_w^{0.2}}, \quad f_M = \frac{0.046}{\text{Re}_M^{0.2}}, \quad f_o = \frac{0.046}{\text{Re}_o^{0.2}}$$

$$\text{with } \text{Re}_w = \frac{4U_w A_w \rho_w}{S_w \mu_w}, \quad \text{Re}_M = \frac{4U_M A_M \rho_M}{(S_M + S_{i1}) \mu_M}, \quad \text{Re}_o = \frac{4U_o A_o \rho_o}{(S_o + S_{i2}) \mu_o} \quad (2-60)$$

$$f_{i1} = f_M, \quad f_{i2} = f_o \quad (2-61)$$

A mass balance is carried out for the water phase and the oil phase (2-62).

Dividing by the pipe cross sectional area produces Equation (2-63), which contains

superficial velocity of each layer. With six unknown parameters:  $A_w$ ,  $A_m$ ,  $U_{swL}$ ,  $U_{sol}$ ,  $U_{sm}$ , and  $\varepsilon_m$ , two more equations are required. The water cut in the mixing layer,  $\varepsilon_m$ , is estimated to be equal to either the input water cut for low viscosity oil or equal to 50% for high viscosity oil based on experiment observations (Vedapuri *et al.*, 1997). Shi (2001) confirmed that the water cut in the mixing layer is between the input water cut and 50% based on flow loop test results. Since there was no theoretical correlation developed to calculate the *in situ* water cut in the mixing layer, Cai *et al.* (2004) assumed it equal to 50%. They also proposed an entrainment factor, FE, shown in Equation (2-64), in which  $U_{crit}$  is the critical oil phase velocity for full water entrainment. The entrainment factor describes how close the oil phase velocity is approaching the critical entrainment value. When the entrainment factor equals one, all the water phase is entrained and the thickness of the water layer should approach zero. The superficial velocity of the pure water layer,  $U_{swL}$ , can be estimated with Equation (2-65). Substituting it into (2-63) gives (2-66) and (2-67) for the superficial velocity of the mixing layer and the pure oil layer.

$$Q_w = Q_{wL} + \varepsilon_m Q_m, \quad Q_o = Q_{oL} + (1 - \varepsilon_m) Q_m \quad (2-62)$$

$$U_{sw} = U_{swL} + \varepsilon_m U_{sm}, \quad U_{so} = U_{sol} + (1 - \varepsilon_m) U_{sm} \quad (2-63)$$

$$FE = \frac{U_{so}}{U_{crit}} \quad (2-64)$$

$$U_{swL} = U_{sw} (1 - FE) \quad (2-65)$$

$$U_{sm} = \frac{U_{sw} \cdot FE}{\varepsilon_m} \quad (2-66)$$

$$U_{sol} = U_{so} - (1 - \varepsilon_m) \frac{U_{sw} \cdot FE}{\varepsilon_m} \quad (2-67)$$

The number of equations now equals the number of unknowns. The three-layer stratified flow model requires the same input parameters as the water entrainment model, density of oil and water, viscosity of oil and water, oil-water interfacial tension, pipe diameter, pipe inclination and either superficial velocity of oil and water or mixture velocity and water cut. To get the thickness of the water layer ( $H_w$ ) and the *in situ* water phase velocity ( $U_{sw}$ ), the momentum and mass balance Equations (2-56), (2-57) and (2-63) need to be solved simultaneously.

### 2.2.3 Small scale apparatus for studying oil-water two-phase flow

To understand the physics of water wetting and water entrainment for CO<sub>2</sub> corrosion, most of the experimental work has been conducted in laboratory flow loops since accurate oilfield measurements are difficult. However, such large scale flow loops have difficulties and drawbacks, such as large amounts of oil required, pumping effect, separation issue, pipe size and length, pipe material, *etc.* Therefore, a small scale benchtop apparatus is needed to study phase wetting and CO<sub>2</sub> corrosion in multiphase flow. Little information on this topic can be found in the open literature.

Nesic and Carroll (2003) designed a horizontal rotating cylinder apparatus (Figure 5) for studying phase wetting and CO<sub>2</sub> corrosion in oil-water two-phase flow. The carbon steel coupon mounted on the rotating shaft is cyclically exposed to each phase. With increasing rotating speed, either water or oil phase can be dragged up or down to replace another phase covered on the steel surface. The corrosion measurements and visualization were conducted in water-hexane mixture with water cut between 5 to 50%. Their tests showed that the steel surface is hydrophilic under stagnant condition and preferentially

wetted by water at low velocity and high water cut. A critical velocity was found for full oil wetting. When the full oil wetting is reached, water is unlikely to replace the oil on the steel surface. It is clear that there are big differences between this small scale apparatus and a large scale flow loop, such as different flow patterns, rotating steel surface, hydrodynamic water entrainment, *etc.*, and this makes the knowledge transfer between the two systems unlikely. The authors claimed that the purpose of their work is to provide a preliminary and simple idea to stimulate other engineers for further development.

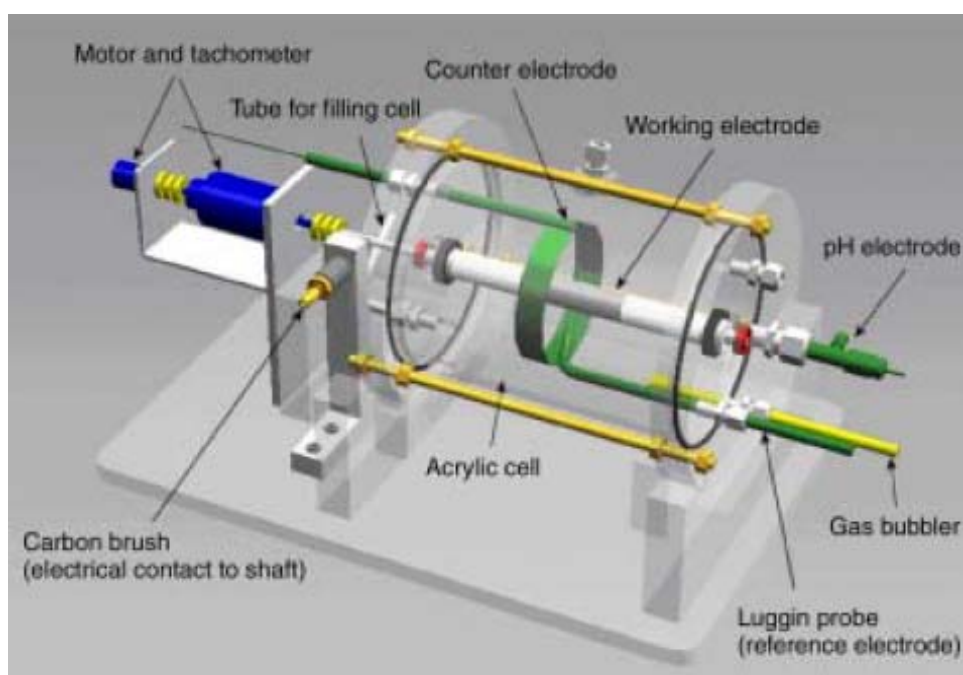


Figure 5 3D rendering of a horizontal rotating cylinder apparatus for studying effect of water wetting on CO<sub>2</sub> corrosion (Nesic and Carroll, 2003).

Cai *et al.* (2005b) updated the horizontal rotating cylinder apparatus with magnetic driving system (Figure 6) for high pressure application. The emulsion stability and phase inversion point for different crude oils was studied using this apparatus.

However, no further design improvement was made on determinations of water wetting and water entrainment.

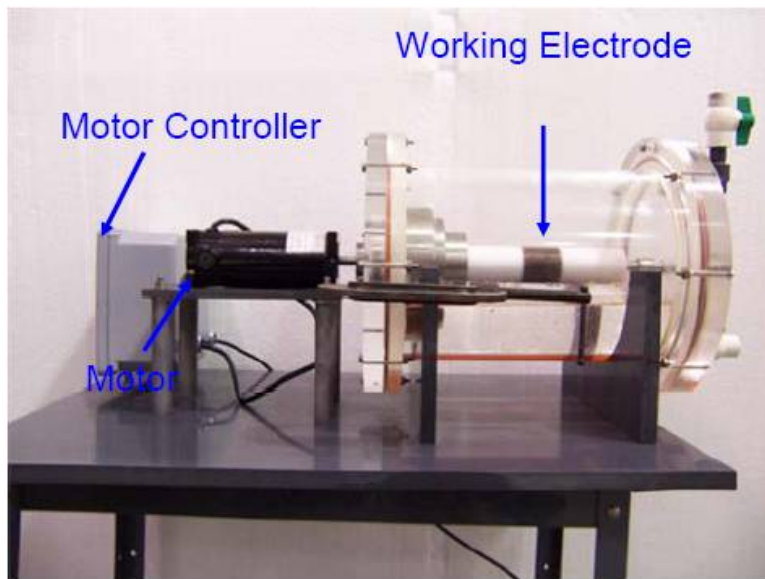


Figure 6 Real view of updated horizontal rotating cylinder apparatus (Cai *et al.*, 2005b).

Pots *et al.* (2006) published descriptions on a small scale apparatus, called a carousel (Figure 7), which was developed in their laboratory to study water entrainment and breakout in crude oils. Crude oil and water are held in a circular flow channel. A rotating wheel on top brings the oil into circular motion with shearing and water is sheared by the oil into circular motion. The apparatus only requires a few liters of liquid. The authors found that even with the help from Computational Fluid Dynamics (CFD) simulation, the carousel only produced qualitative results for water breakout tendency and no absolute value of critical water entrainment velocity could be obtained. The main drawbacks of the carousel were summarized by the authors as follows: the Reynolds number for laminar to turbulent flow transition in carousel is much larger than in pipes

(11000 *versus* 2100); secondary flow came from the velocity gradient within the rectangle-shaped cross section and influenced the motion of entrained water droplets in the flowing oil phase.

The intensity of a secondary flow can be minimized by optimizing the dimensions (height and width) of the flow channel. The small scale apparatus designed in the present work, which will be described in Chapter 7, is based on the same theory of carousel but with major improvements. It should be pointed out that little information on the details of the design of carousel is available and no test results from carousel can be found in the open literature.



Figure 7 Small scale apparatus, carousel, used for studies of water entrainment and breakout in crude oil (Pots *et al.*, 2006).

## 2.3 Corrosion inhibitors

### 2.3.1 Surface active properties

Most corrosion inhibitors used in oilfields are organic compounds, containing nitrogen or sulfur functionalities. They belong to the surfactant category of molecules (surface active agents), which preferentially adsorb onto any surface or interface in a system and alter the surface and interfacial free energies, even at low concentration (usually referring to ppm level) (Rosen, 2004, p. 1). The surface active properties come from their amphipathic, lipid like, molecular structure which contains a polar head group having strong attraction to water, referred to as a hydrophilic head and a non-polar hydrocarbon chain having little attraction to water, called a hydrophobic tail. The way organic corrosion inhibitors inhibiting CO<sub>2</sub> corrosion of carbon steel is related to their surface active properties can be described in three parts: adsorption onto the steel surface (diffusion or protective layer), changing the wettability of the steel surface (so it is not wetted with water), and accumulation at the oil-water interfaces (changing the oil-water interfacial tension and making it easier for the oil to entrain the water).

It is accepted that organic corrosion inhibitors adsorb onto the steel surface to inhibit corrosion processes. The types of adsorption can be distinguished by the mechanisms: physical (electrostatic) adsorption involves an electrostatic attractive force between ionic charges on inhibitor molecules and electric charged steel surface; chemisorption results from sharing free electron pairs or charge transfer to form strong chemical bonds between nonionic inhibitor molecules and steel (Papavinasam, 2000, p. 1091). The examples of ionic type and nonionic type inhibitors are quaternary

ammonium chloride,  $RN(CH_3)_3^+ Cl^-$  (Rosen, 2004, p. 3) and imidazoline,  $R_1N(CH_2)_2NR_2$  (Gusmano *et al.*, 2006).

Independent on the adsorption mechanisms, the attractions or chemical bonds are between the hydrophilic head of inhibitor molecule and the steel surface. In a layer of adsorbed inhibitor molecules, the hydrophobic tail on the inhibitor molecules face toward the bulk solution and have a strong tendency for self-assembly to form a hydrophobic barrier for corrosive water (Ramachandran *et al.*, 1996). It is believed that by forming the hydrophobic barrier, surfactants can alter the surface wettability of carbon steel. The wettability of a steel surface in oil-water two-phase system involves the interaction between oil-water, oil-steel and water-steel interfacial tension. Since liquid-steel interfacial tension is not easy to measure directly, the contact angle of a liquid droplet on steel surface has been used to indicate surface wettability (Rosen, 2004, p.246). An illustration of water-in-oil contact angle is shown in Figure 8. The force balance of three interfacial tensions acting on the droplet is shown in Equation (2-68), called Young's equation. An angle of  $90^\circ$  or greater indicates that the surface is hydrophobic and an angle less than  $90^\circ$  indicates that the surface is hydrophilic.

$$\sigma_{oil-water} \cos \alpha = \sigma_{water-steel} - \sigma_{oil-steel} \quad (2-68)$$

Schmitt and Stradmann (1998) conducted contact angle measurements by placing oil and water droplets on carbon steel specimens in a high pressure test apparatus. The tests were performed under 75 and 80°C and 5 bar CO<sub>2</sub>. The testing fluids are different crude oils, a synthetic oil and brine with surfactants (inhibitors and deemulsifiers) added into the system. The contact angle measurements were made on the clean surface and

pre-corroded (6, 24, 48 and 72 hours) surface. It was found that clean carbon steel surface and pre-corroded surface covered with  $\text{FeCO}_3$  scale both show hydrophilic wetting property. The addition of quaternary ammonium inhibitor under  $\text{FeCO}_3$  scale formation conditions results in a hydrophilic surface, however fatty amine and imidazoline based inhibitors produce a hydrophobic surface.

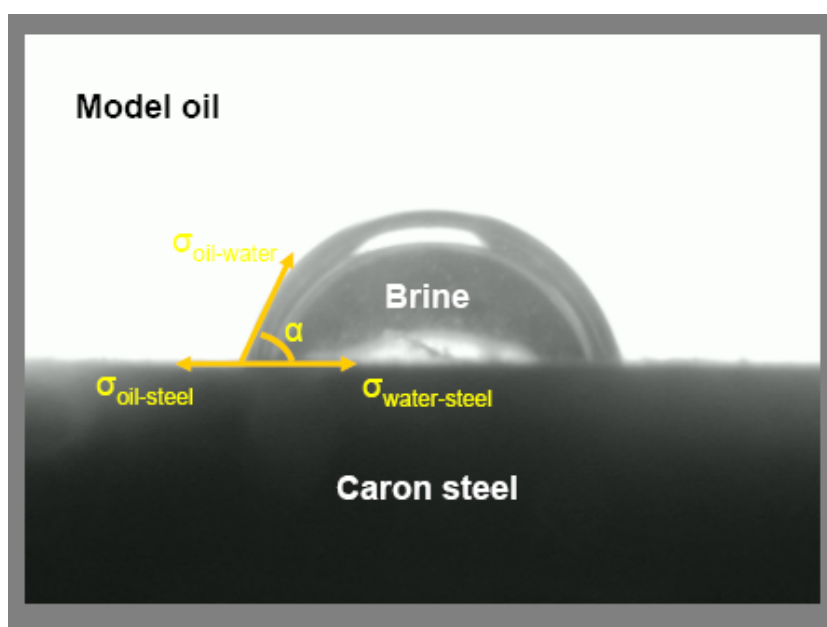


Figure 8 Contact angle of a water droplet on carbon steel surface immersed in a continuous oil phase, showing how the interfacial tension at oil-water, oil-steel and water-steel determine the shape of the droplet (Li *et al.*, 2008).

Foss *et al.* (2008) investigated the effect of corrosion inhibitors on the wettability of the steel surface covered by  $\text{FeCO}_3$  protective scale. The wettability tests were conducted with contact angle measurements in refined oil-brine system. The authors found that oleic imidazoline and phosphate ester promote oil wetting for clean steel surface and  $\text{FeCO}_3$  covered steel surface. The initially oil wetted steel surface becomes water wetted with the addition of cetyltrimethylammonium bromide (ionic surfactant).

The corrosion tests on a stationary electrode in a 3-liters glass cell showed that the inhibition performances of oleic imidazoline and phosphate ester were greatly enhanced after a direct contact of the test electrode to the oil phase. Without a direct contact (*i.e.*, the test electrode is wetted by the brine phase), the presence of an oil phase on the top of brine phase can also improve the inhibition performances of two inhibitors. The authors assumed that the structure of adsorbed inhibitor molecules layer was altered by the dissolved hydrocarbon in brine (micro-liter solubility) to have better protectiveness.

It is well known that corrosion inhibitors partition between the oil and water phases. The concentrations of inhibitor in oil and water depend on the solubility of specific inhibitor. Some inhibitor molecules are also present at the oil-water interface, with their hydrophilic heads facing to water and hydrophobic tails orienting to oil. This behavior minimizes the contact area of oil-water two-phase, which results in a reduction of oil-water interfacial tension. The oil-water interfacial tension has a significant effect on the water entrainment in oil-water two-phase flow, which can be seen from maximum droplet size calculation, Equations (2-33) and (2-43). With increasing surfactant concentration in a media, at one point, which is called critical micelle concentration (CMC), colloidal-sized clusters (micelles) of surfactant molecules form. A reduction break point of oil-water interfacial tension up to the CMC can be found for some corrosion inhibitors. Micelle formation of corrosion inhibitors in oil-water two-phase flow promotes oil-in-water or water-in-oil emulsion, which is the stable dispersion of one liquid phase in another immiscible liquid phase.

Moon and Horsup (2002) measured the changes of a model oil-brine interfacial tension with five different corrosion inhibitors with a tensiometer. A great reduction of oil-water interfacial tension was found for even a low concentration of inhibitor. Above the CMC point the interfacial tension becomes stable and full dispersion begins to form. The emulsion stability tests were performed by mixing and separating oil and water in sampling tubes. It was found that inhibitors enhance stability of oil-water emulsions due to a lower interfacial tension. A dramatic increase of oil-water interface area during emulsion formation can trap appreciable amounts of inhibitor molecules. The authors claimed that loss of inhibitor at the oil-water emulsion interface can cause corrosion inhibition failure. Similar findings were reported by Knag *et al.* (2006).

McMahon (1990 and 1991) studied adsorption, interfacial phenomenon and wettability by testing sodium alkylethoxyphosphate (water soluble), oleic imidazoline and oleic amide (oil soluble) corrosion inhibitors. All the tested inhibitors have a significant affinity for the oil-brine interface. The reductions of interfacial tension measured by a Wilhelmy plate exist up to the CMC points. The author conducted adsorption tests by using iron powder. The adsorption of inhibitors from either the oil or brine phase was proved to be fast enough to form a molecule monolayer fitting a Langmuir isotherm. The corrosion inhibition was proportional to the measured surface coverage. The contact angle measurements of oil-in-water and water-in-oil indicated that the surface became hydrophobic and oil wetting is enhanced after inhibitor adsorption.

### 2.3.2 Modeling of corrosion inhibition

One key concept for all kinds of corrosion inhibitors is the inhibition efficiency (IE) shown in Equation (2-69), in which  $CR_{\text{uninhibited}}$  is a corrosion rate without inhibition and  $CR_{\text{inhibited}}$  is a corrosion rate under inhibition. Inhibition efficiency is used in every stage from laboratory testing and modeling to final deployment in oilfield. The inhibition mechanism of an inhibitor is not well understood. The proposed mechanisms suggest that the adsorbed inhibitor molecules may change the anodic or cathodic reaction rates, or affect mass transfer of the corrosive species, or simply block the steel surface to make areas less available for corrosion process, or displace the water molecules on the surface with the hydrophilic heads and repel the water with the hydrophobic tails. Since it is not straightforward to predict the inhibition efficiency, inhibitor factors obtained from experimental work has been used in empirical CO<sub>2</sub> corrosion inhibition models.

$$IE = \frac{CR_{\text{uninhibited}} - CR_{\text{inhibited}}}{CR_{\text{uninhibited}}} \quad (2-69)$$

Complex molecular modeling has been applied to simulate the interaction between individual inhibitor molecule and steel surface and the interaction between inhibitor molecules with each other (Ramachandran *et al.*, 1996). Durnie (2000) applied a molecular modeling method to calculate thermodynamic parameters of adsorption, such as enthalpy and entropy, to predict inhibition efficiency. However, the performance of an inhibitor depends not only on molecular structure, but also on the steel surface conditions and environmental conditions (pH, temperature, water chemistry, *etc.*).

Equivalent circuit has been built based on electrochemical impedance spectroscopy (EIS) measurements to explain adsorption molecules layer formation and

inhibition mechanism. Examples of equivalent circuits proposed by Gusmano *et al.* (2006) for corrosion process with and without inhibitor are shown in Figure 9. In the Figure,  $R_s$  is the solution resistance,  $R_{ct}$  is the charge transfer resistance,  $C_{dl}$  is the double layer capacitance,  $C_f$  and  $R_f$  are the capacitance and resistance of the inhibitor adsorption layer.

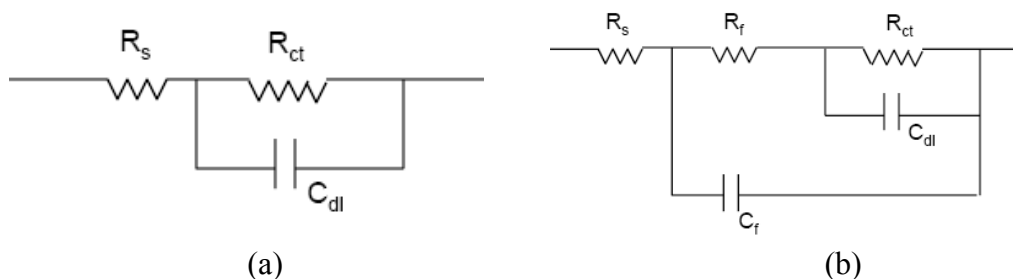


Figure 9 Equivalent circuits for CO<sub>2</sub> corrosion: (a) without inhibitor; (b) with inhibitor. The addition of inhibitor adds another time constant to the Equivalent circuit.

A simple and common approach is to assume that the inhibition efficiency is equivalent to the surface coverage of the inhibitor molecules, *i.e.*, the corrosion rate under inhibitor protection,  $CR_{inhibited}$ , is proportional to the steel surface covered by inhibitor,  $\theta$  (2-70). Since an inhibitor is a kind of surfactant, adsorption isotherms, which describe the concentration of adsorbed surfactant on the surface compared to its equilibrium concentration in bulk solution, have been applied for inhibitors to calculate the surface coverage  $\theta$ .

$$CR_{inhibited} = (1 - \theta) \cdot CR_{uninhibited} \quad (2-70)$$

Table 1 shows different types of adsorption isotherms found in the literature related to surfactant adsorption at medium-solid interface (Papavinasam, 2000, p. 1096

and Chokshi, 2004). The basic form is a Langmuir isotherm. It assumes that monomolecular layer forms and no interactions occur between the adsorbed inhibitor molecules. The Temkin and Frumkin isotherms consider the molecule interactions by adding an interaction factor,  $f$ . Positive value of  $f$  indicates an attraction and a negative value indicates a repulsion. Flory-Huggins isotherm assumes that organic molecules from the solution replace adsorbed water molecules on the steel surface. The molecular size ratio is accounted by a steric/size factor,  $x$ , which is the number of water molecules substituted by one organic molecule. Dhar *et al.* (1973) proposed a modified Flory-Huggins isotherm. To evaluate several parameters in different adsorption isotherms, corrosion experiments need to be conducted to obtain corrosion rate with and without inhibition under varied inhibitor concentrations in bulk solution ( $c_{inh}$ ). The surface coverage ( $\theta$ ) in percentage can be calculated by Equation (2-70). The best-fit values of the adsorption/desorption equilibrium constant ( $K_{a/d}$ ), interaction factor ( $f$ ) or steric/size factor ( $x$ ) can be calculated with the values of slope and intercept obtained from the data fitting plots shown in Table 1. Once these constants are known, the inhibition efficiency can be predicted for any given inhibitor concentration. It should be noted that the experimental best-fit constants work only for the specific tested corrosion inhibitor under the testing conditions. If inhibitor structure and environments are altered, new values of constants should be derived from experimental data.

Table 1 List of adsorption isotherms.

Adsorption isotherm	Equation	Data fitting plot
Langmuir	$K_{a/d}c_{inh} = \frac{\theta}{1-\theta}$	$\log \frac{\theta}{1-\theta}$ vs. $\log c_{inh}$
Temkin	$K_{a/d}c_{inh} = e^{f\theta}$	$\theta$ vs. $\ln c_{inh}$
Frumkin	$K_{a/d}c_{inh} = \frac{\theta}{1-\theta} e^{-f\theta}$	$\ln \frac{\theta}{(1-\theta)c_{inh}}$ vs. $\theta$
Flory-Huggins	$K_{a/d}c_{inh} = \frac{\theta}{x(1-\theta)^x}$	$\log \frac{\theta}{c_{inh}}$ vs. $\log(1-\theta)$
Modified Flory-Huggins	$K_{a/d}c_{inh} = \frac{\theta}{e^{x-1}(1-\theta)^x}$	$\ln \frac{\theta}{c_{inh}}$ vs. $\ln(1-\theta)$

### CHAPTER 3: RESEARCH OBJECTIVES

The carbon dioxide corrosion of carbon steel pipeline results from the co-production of corrosive water phase with crude oil and furthermore the direct water wetting of the inner wall pipe. The main motivation for investigating oil-water two-phase flow in the connection with CO<sub>2</sub> corrosion is to improve our knowledge of phase wetting regimes under different flow conditions and the corresponding transition between oil and water wetting. This will be achieved by:

- Investigation of flow patterns, phase wetting regimes and CO<sub>2</sub> corrosion in oil-water two-phase flow conducted in a 4 inch ID, horizontal and inclined flow loop.
- Construction of phase wetting maps for a model oil and specific crude oils provided by the project sponsoring companies.
- Comparison of phase wetting transitions from corrosion to corrosion free condition for model oil and different crude oils and to identify important parameters influencing water entrainment and water breakout.

Another part of the work presented here connects the surface active properties of corrosion inhibitors to their corrosion inhibition performance in oil-water two-phase systems. The interactions between steel surface, corrosion inhibitor, oil and water have been focused on:

- Study of inhibition performance of CO<sub>2</sub> corrosion inhibitor in oil-water two-phase system by using a three-electrode setup with electrochemical measurements in a glass cell.

- Investigation of the wettability of carbon steel surface by employing contact angle measurements with inhibitor present.
- Determination of the changes of oil-water interfacial tension in the presence of inhibitor and conductance of emulsion formation and stability tests.

One of the challenging problems of the investigation of the phase wetting of oil-water two-phase flow is how to conduct quick response tests in small scale apparatus. A critical requirement for designing a small scale apparatus is that the processes of water droplet entrainment, coalescence and breakout should be achieved as is the case for pipe flow. The goal of this part of work is achieved by doing the following:

- Design and construct a prototype small scale apparatus, called a doughnut cell, and transplanting technologies used to determine phase wetting regimes in flow loop tests.
- Investigating phase wetting transitions of model oil and different crude oils in the doughnut cell.
- Propose a scale-up method from doughnut cell test to flow loop test conditions.
- Study the effect of corrosion inhibitor on phase wetting regimes in the doughnut cell.

One of the most important goals in this work is to enhance our capability to predict the transition of phase wetting regimes (water entrainment and water breakout)

and corrosion inhibition by inhibitors in oil-water two-phase pipe flow. The modeling work is achieved by:

- Development of a phase wetting prediction model for oil-water two-phase pipe flow.
- Verification of the phase wetting model with experimental data from flow loop and doughnut cell tests.
- Development of a corrosion inhibition model by fitting an adsorption isotherm with experimental data from corrosion inhibition tests.
- Linkage of the phase wetting model, a three-layer stratified flow model, mechanistic corrosion prediction models, and the corrosion inhibition model to predict uninhibited and inhibited CO<sub>2</sub> corrosion rates in oil-water two-phase pipe flow. The proposed method includes effect of corrosion inhibitor on phase wetting and CO<sub>2</sub> corrosion inhibition.

## CHAPTER 4: EXPERIMENTAL STUDY OF OIL-WATER PIPE FLOW

### 4.1 Experimental setup and procedure

In order to understand the experimental results, a detailed description of flow loop facilities and instrumentation along with test procedure is given here.

#### 4.1.1 Multiphase flow loop

All large scale experiments have been conducted in a 200 feet long, 4 inch internal diameter (ID) multiphase flow loop mounted on a fully inclinable rig. Three main feed lines, oil, water, CO<sub>2</sub> gas lines and one oil-water mixture flowline are shown in Figure 10. The main components in this flow loop system are marked by numbers in the figure and listed in Table 2.

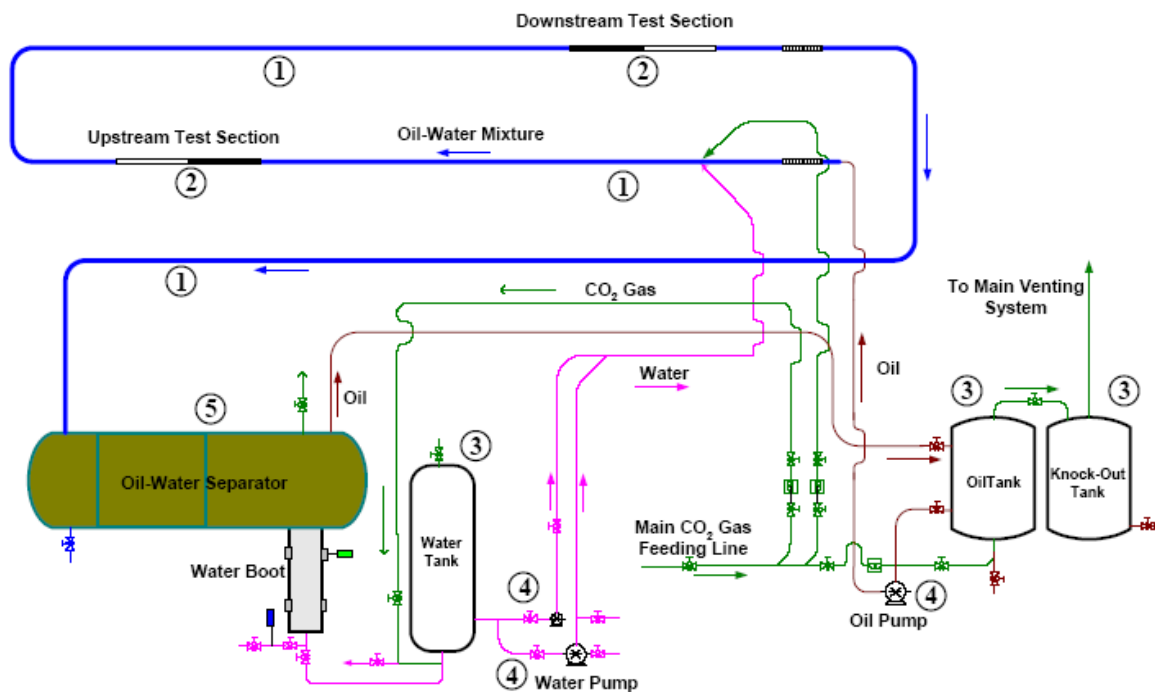


Figure 10 Schematic of multiphase flow loop used for large scale oil-water two-phase investigation (Courtesy of Jiyong Cai).

Table 2 Main components in multiphase flow loop system displayed in Figure 10.

	<b>Name</b>	<b>Comments</b>
1	Acrylic, PVC and stainless steel pipes	<ul style="list-style-type: none"> <li>• Corrosion-free materials</li> </ul>
2	2 test sections	<ul style="list-style-type: none"> <li>• Made from carbon steel</li> </ul>
3	3 storage tanks	<ul style="list-style-type: none"> <li>• Water, oil storage tanks and oil knock-out tank</li> </ul>
4	3 Moyno pumps	<ul style="list-style-type: none"> <li>• Oil pump pumps oil from oil storage tank</li> <li>• Small water pump pumps water from water storage tank for water cuts lower than 20% at low flow rates</li> <li>• Bigger water pump is used for water cuts higher than 20% at high flow rates</li> </ul>
5	Oil-water separator	<ul style="list-style-type: none"> <li>• 500 gallon volume</li> </ul>

Oil and water are stored in 1.2 m<sup>3</sup> stainless steel tanks. They are pumped separately by Moyno positive displacement pumps equipped with a variable speed motor. The flow rates of oil and water are controlled by motor controllers. The oil pump (model APG type 320DM6A) has a maximum pumping error of  $\pm 0.4\%$  in flow rate within the test oil velocity of 0.5 to 3.0 m/s. The small water pump has an error of  $\pm 0.13\%$  in flow rate, which is calibrated by an OMEGA FP-5300 flow sensor. Oil and water are mixed in a T-shape section. The mixture flows through a 3-meter long flexible rubber hose, which allows flow loop inclining by hydraulic lifting to be set at any angle from horizontal to vertical. Following the rubber hose, a 14-meter total length of PVC pipe and stainless steel pipe are used to fully develop and stabilize the oil-water flow pattern and phase wetting. The fluids then flow through a 2-meter long upstream carbon steel test section followed by a 2-meter long transparent acrylic pipe used for flow pattern visualization. After that the fluids flow through a 180-degree U-shape bend and enter into another 14-

meter total length of PVC pipe and stainless steel pipe. The downstream carbon steel test section and another 2-meter long acrylic pipe follow. The mixture flows through a 20-meter long PVC pipe to enter into oil-water separator. After separation, oil flows back to the oil storage tank through an outlet pipe on the top of the separator. Water accumulates in the water boot and flows back to the water storage tank through an outlet pipe on the bottom of the separator. Experimental measurements are conducted in the test sections. The same phase wetting regime is expected in both the test sections during horizontal flow. However, for inclined flow the two test sections can distinguish different flow patterns and phase wetting regimes in upward and downward flows.

The oil-water separator is a key component in the whole system. It enables circulation of pure oil and water during the test without mixing or emulsion formation. Figure 11 shows a schematic of the internal structure of the separator. A liquid distributor near the inlet side is used to uniformly distribute the mixture on the cross section of the separator. Following the distributor a droplet coalescer made from two dissimilar wettability materials, stainless steel and plastic, allows more effective coalescence of dispersed droplets. Four sets of enhanced plate separators after the coalescer separate oil and water due to density differences. During testing samples from sampling ports of oil outlet and water outlet pipes demonstrate that a good separation efficiency is achieved.

Since CO<sub>2</sub> corrosion is studied in large scale pipe flow, the oil and water need to be deoxygenated by purging CO<sub>2</sub> gas in water and oil storage tanks. The oil and water are also circulated in the flow loop system while CO<sub>2</sub> gas is flushing to deoxygenate for fluids in the separator. The deoxygenation process usually takes three hours to achieve

oxygen concentration below 25 ppb. The oxygen concentration in the water phase is measured by using Oxygen CHEMets test kit at the water sampling port on the water boot (Figure 12). When the oxygen concentration is below 25 ppb, the CO<sub>2</sub> gas supply valve and venting valves have to be closed to maintain an “oxygen free” closed system.

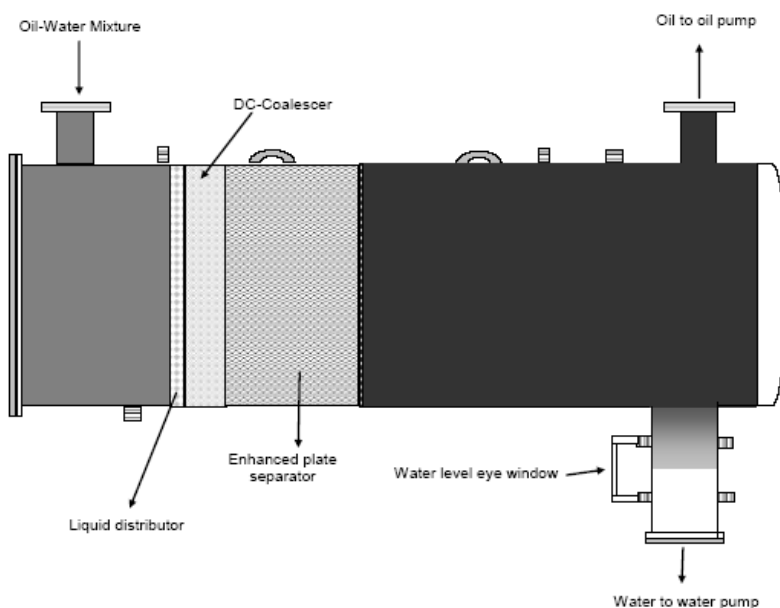


Figure 11 Schematic of the internal structure of oil-water separator, which is a part of the inclinable flow loop system used in this study (Courtesy of Jiyong Cai).

Water samples are collected in sampling tubes during tests for total iron concentration analysis by using a standard colorimetric technique with a Turner SP-870 spectrophotometer. A FerroVer reagent is added into the water samples, which allows insoluble iron oxides to be reduced to ferrous state. Ferrous irons react with the reagent to form an orange-red complex for spectrophotometer analysis. The total iron concentration allows the calculation of the average corrosion rate under different flow conditions. It should be noted that only two carbon steel test sections in the flow loop can be corroded

during experiments. Other components in the system are made of corrosion-free materials, such as PVC and stainless steel. The oil-water separator is made of carbon steel, coated with corrosion resistant epoxy on both the internal and external surfaces. A baseline test for checking the coating efficiency showed that no obvious corrosion can be found after 1 wt% NaCl aqueous electrolyte settled in the separator over 24 hours. A pH probe was installed at the access port on the water boot (Figure 12) to monitor the pH of the water phase.

Safety issues are addressed in the author's work by wearing safety glasses, oil-protected shoes and uniform. A flow loop operating procedure, which includes filling, system deoxygenation, startup, shutdown, draining and emergency, is strictly obeyed. The model oil and crude oils are stored in steel barrels. In case of an oil spill, oil dry sand is used to contain the spill area and to absorb the oil.

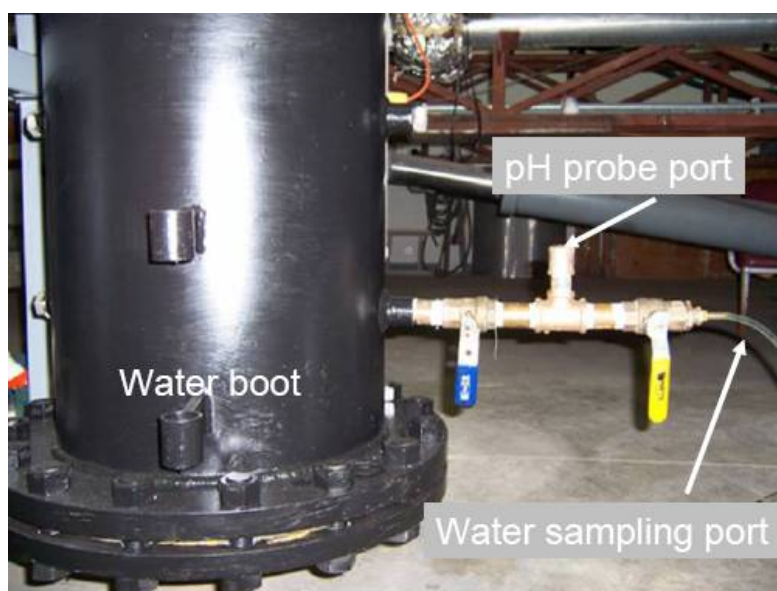


Figure 12 pH probe port and water sampling port on the water boot of the separator, which is a part of the inclinable flow loop system used in this work.

#### 4.1.2 Test sections and instrumentation

Figure 13 shows a real view picture of the upstream test section. Since it is made out of carbon steel, when corrosion occurs due to water wetting the inner wall of the pipe, an increase of  $\text{Fe}^{2+}$  concentration is expected. The water sampling and  $\text{Fe}^{2+}$  concentration measurements can give corrosion rates at each test condition. The external surfaces of the two test sections are coated with corrosion resistant epoxy.

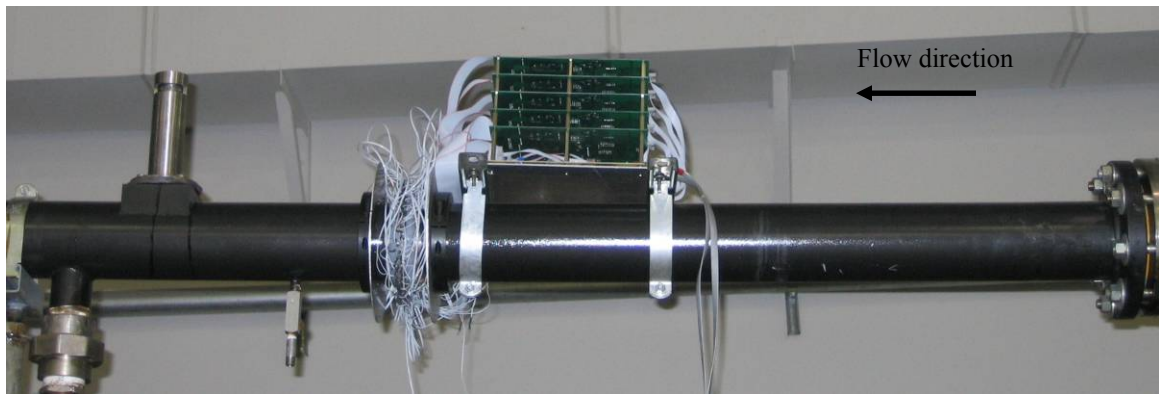


Figure 13 Upstream test section of the inclinable flow loop system used in this work.

Four techniques were applied during the experiments to determine phase wetting regimes on the pipe inner wall. A schematic view of the developed techniques in this work are (Figure 14): wall conductance probes, wall sampling, traversing conductance probes, corrosion rate monitoring by electrical resistance probe,  $\text{Fe}^{2+}$  concentration measurement, and flow pattern visualization.

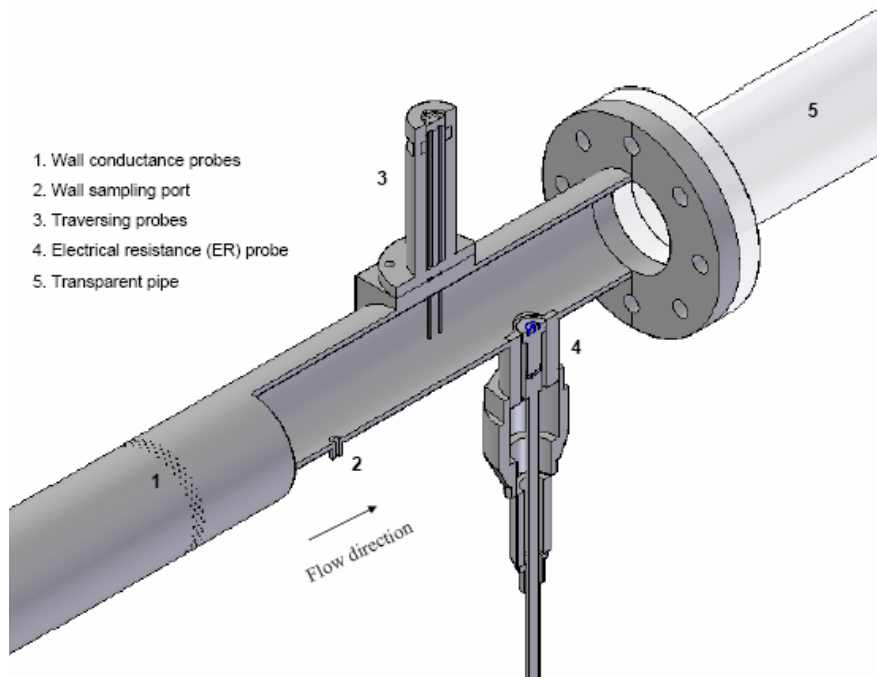


Figure 14 Schematic of a test section with the instrumentation marked (Courtesy of Joshua Addis).

The wall conductance probes are a crucial measurement technique in this work. The probes consist of an epoxy coated 0.018-inch diameter stainless steel wire in a 0.0625-inch stainless steel socket with an electrical pin. Holes of 0.0625-inch diameter are drilled in the test sections. The probes are flush mounted at the pipe inner surface through the drilled holes and insulated with epoxy from the pipe wall. The two test sections are not the same. Five staggered rows of 32 probes in a row (total of 160 probes) are set around the whole circumference of the upstream test section, while three rows of 19 probes in a row and two staggered rows of 18 probes in a row (total of 93 probes) are installed on the bottom half only of the downstream test section pipe circumference. The staggered spatial arrangement (shown in Figure 15) for conductance probes helps to

minimize the effect of water phase “snaking” behavior around/between probes (0.25-inch equal distance between each probes).

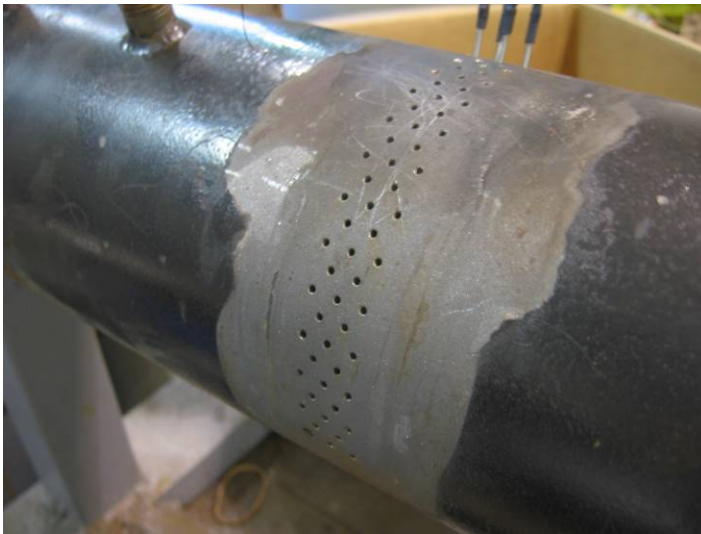


Figure 15 Staggered spatial arrangement on the upstream test section for wall conductance probes.

Each probe is connected to a 100k $\Omega$  resistor, which is connected to circuit boards (can be seen in Figure 13). During measurements, the circuit switches from +12 volts to -12 volts in 20 micro-seconds. In this way, if water wets the tip of one probe and the pipe wall near it, 0 to 1.5-volt potential between the probe and the resistor can be observed due to a short circuit developing due to water conductivity. If oil covers the probe and the pipe wall, the voltage between the probe and the resistor is between 3.5 to 5 Volts because non-conductivity of the oil causes an open circuit at the probe. This measurement is taken on all conductance probes simultaneously. The results are stored as binary data (0 means oil wetting and 1 means water wetting) and read into a data acquisition software installed on a computer. The data acquisition software, which was developed by Mr.

Albert Schubert and this author, can monitor the phase wetting state of each probe (the details and interfaces of this software will be described in Appendix A).

Wall sampling method is a method used to extract fluid from the bottom surface of the test section into sampling tubes. The oil and water ratio in the sample reflects the fluid content very close to the bottom pipe surface. The extraction rate is controlled by a needle valve and a solenoid valve on the sampling port. Too slow sampling can cause separation of oil and water during the sampling process and too fast sampling can suck the fluid from bulk flow.

CO<sub>2</sub> corrosion rate is measured with a flush mounted electrical resistance probe and Fe<sup>2+</sup> concentration count (mentioned above). Both of these two techniques take much longer measurement time (typically a few hours) than other techniques used for phase wetting regime determination (usually a few minutes) under a fixed test condition.

Flow pattern visualization (both digital photos and videos) is conducted through the acrylic pipe just following the test section. Water dyed with red food color is used to enhance the contrast between the transparent model oil and water. In another test series, fluorescein dyed water is used with a UV light placed at the bottom of the acrylic pipe to observe flowing of the water phase with a crude oil contaminated model oil, which was no longer transparent.

It should be noted that there are application limitations for each technique used in the flow loop tests. However, it was expected that the overlapping and cross checking information obtained from all techniques can assure the accuracy of the test results and provide more confidence on model validation.

#### 4.1.3 Experimental procedure

16 barrels of oil and 400 gallons of deionized water with 1wt% NaCl are loaded into the storage tanks and the separator. The fluids are deoxygenated with CO<sub>2</sub> gas until the oxygen concentration is below 25 pbb. The experiments start with lowest water cut (1% or 2%) at minimum value of superficial oil velocity (0.5 m/s). There is a gradual increase in water cut up to 20% at constant superficial oil velocity or mixture velocity. After that, the superficial oil velocity is increased and the water cut is gradually increased from 1% to maximum value 20%. The maximum superficial oil velocity is set as 2 m/s in this work. After horizontal tests are complete, inclination is studied at 2°, 5°, 45° and 90°. Measurements by wall conductance probes, wall sampling and flow pattern visualization were conducted under each flow condition. Since corrosion monitoring technique takes longer time, only a part of tested flow conditions are selected to measure CO<sub>2</sub> corrosion rate.

#### 4.1.4 Test matrix

Table 3 shows the test matrix for oil-water two-phase flow loop tests. Seven different crude oils provided by project sponsored companies are re-named in cryptonym. Some of them are received in quantities insufficiently large to conduct flow loop tests, but are sufficient for small scale tests. The physical properties of the model oil and the seven crude oils are listed in Table 4. The density is measured by weighing 50-milliliter of liquid in a volumetric flask. HAAKE falling ball viscometer and CSC-DuNouy tensiometer are used to measure viscosity of fluid and oil-water interfacial tension. All the physical properties were measured at room temperature and atmosphere pressure.

Table 3 Test matrix for oil-water two-phase flow loop tests.

<b>Oil phase</b>	Model oil (LVT 200) and Crude oils (C1, C2, C3, C4, C5)
<b>Water phase</b>	De-ionized water with 1 wt% NaCl (dyed with red food color or fluorescein for model oil tests)
<b>Superficial oil velocity</b>	0.5 – 2.5 m/s
<b>Superficial water velocity</b>	0 – 0.22 m/s
<b>Water cut</b>	0 – 20%
<b>Pipe inclination</b>	Horizontal, $\pm 2^\circ$ , $\pm 5^\circ$ , $\pm 45^\circ$ and $\pm 90^\circ$
<b>Pipe diameter</b>	4-inch
<b>System temperature</b>	Room temperature (25°C)
<b>System pressure</b>	Atmospheric pressure (1.013 bar)

Table 4 Physical properties of model oil and seven crude oils tested in this research work.

<b>Oil phase</b>	<b>Density / (kg/m<sup>3</sup>)</b>	<b>API</b>	<b>Viscosity / (cp)</b>	<b>Oil-water interfacial tension / (dyne/cm)</b>
Model oil	825	40.1	2.0	40.0
C1 crude	778	50.3	1.6	25.2
C2 crude	830	39.1	4.7	26.2
C3 crude	853	34.5	9.1	28.1
C4 crude	879	29.6	22.2	23.2
C5 crude	891	27.5	35.8	26.5
C6 crude	849	35.3	8.4	28.0
C7 crude	838	37.5	5.1	31.0

## 4.2 Results and discussion

Flow patterns of model oil-brine two-phase pipe flow are identified at different flow conditions. Depending on the oil-water mixture velocity and the water cut, two main flow patterns are found, stratified and dispersed. There are three subcategories under stratified flow and two subcategories under dispersed flow. A flow pattern map is built and shown in Figure 16 to indicate flow patterns under each test condition. It should be pointed out that oil-water mixture velocity and calculated water cut at each test condition have errors of  $\pm 0.4\%$  and  $\pm 0.13\%$ , respectively, due to pumping errors in flow rate of oil

and water pumps. The same values of experimental errors are applied for phase wetting maps shown below.

Stratified flow with water-in-oil droplets flowing at the bottom of pipe (called “ST with water droplets”) prevails between 0.5 to 1.5 m/s mixture velocity and water cut below 10%. Figure 17 shows example images of this flow pattern. With increasing water cut from 10% to 12%, a thin continuous water layer is found at the bottom of pipe and flow pattern becomes smooth stratified flow (“smooth ST”). If water cut further increases up to 20%, a clear and thick water layer forms and a mixing layer (oil-in-water and water-in-oil dispersions at the interface of stratified oil and water layers) appears at the interface between the continuous water layer at the bottom and the continuous oil layer at the top portion of pipe. The images of flow pattern of stratified flow with mixing layer (“ST with mixing layer”) are shown in Figure 18. The size of the water droplets depends on the mixture velocity. Smaller water droplets are observed when the mixture velocity is increased at constant water cut. The transition from stratified flow to dispersed flow occurs at mixture velocity of 1.5 m/s. Semi-dispersed flow takes place when the mixture velocity is above 1.5 m/s and water cut is greater than 6%. Under such flow conditions, water droplets float in the oil phase and the concentration of dispersed water droplets is not uniform. More water concentrates towards the bottom of the pipe since the gravity force is greater than the turbulent lifting force. In the dispersed region, water cut less than 5% or mixture velocity greater than 2.5 m/s leads to fully dispersed water-in-oil flow. The distribution of dispersed water droplets is quite uniform on the cross section of the pipe.

Flow pattern map gives a macroscopic scale spatial distribution of the fluids in the pipe. The interaction between fluids and pipe inner wall is referred to as phase wetting, which is a link between internal corrosion and multiphase flow. The flush-mounted wall conductance probes are very useful for phase wetting studies. Three main phase wetting regimes are identified through all the tests. It is found that water wetting, where the water phase continuously wets the pipe wall; oil wetting, where oil phase constantly wets the pipe wall and the water is fully entrained in the oil phase; intermittent wetting, where oil and water periodically wet the pipe wall. Based on cross checking results from various measurement techniques, a comprehensive phase wetting map of model oil- brine in horizontal, 4-inch pipe flow is built (Figure 19).

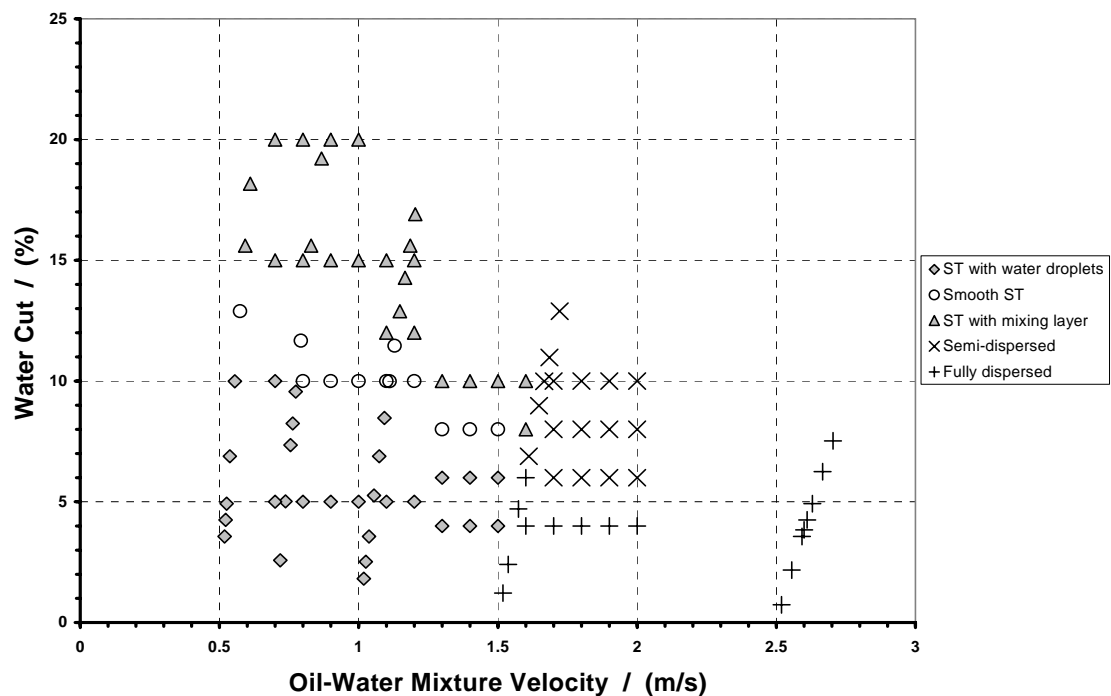
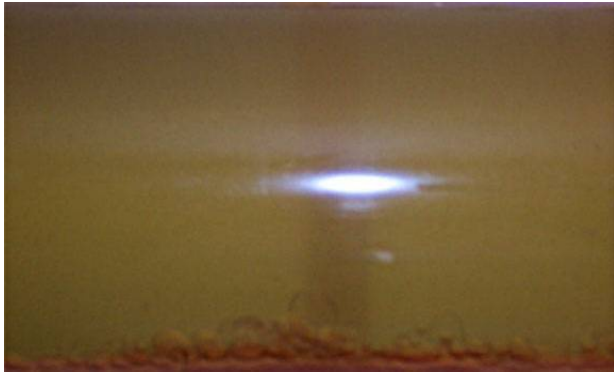


Figure 16 Flow pattern map of model oil-brine in horizontal pipe flow.

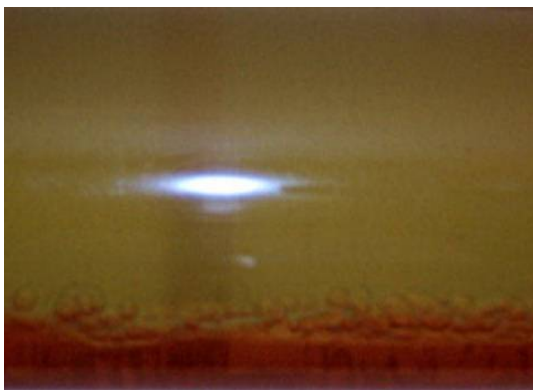


(a)



(b)

Figure 17 Flow pattern of stratified flow with water droplets: (a) red food color dyed water and model oil at mixture velocity of 0.52 m/s and water cut of 4.9%; (b) fluorescein dyed water and model oil at mixture velocity of 0.5 m/s and water cut of 5%.



(a)



(b)

Figure 18 Flow pattern of stratified flow with mixing layer: (a) mixture velocity of 0.61 m/s and water cut of 18%; (b) mixture velocity of 0.75 m/s and water cut of 20%.

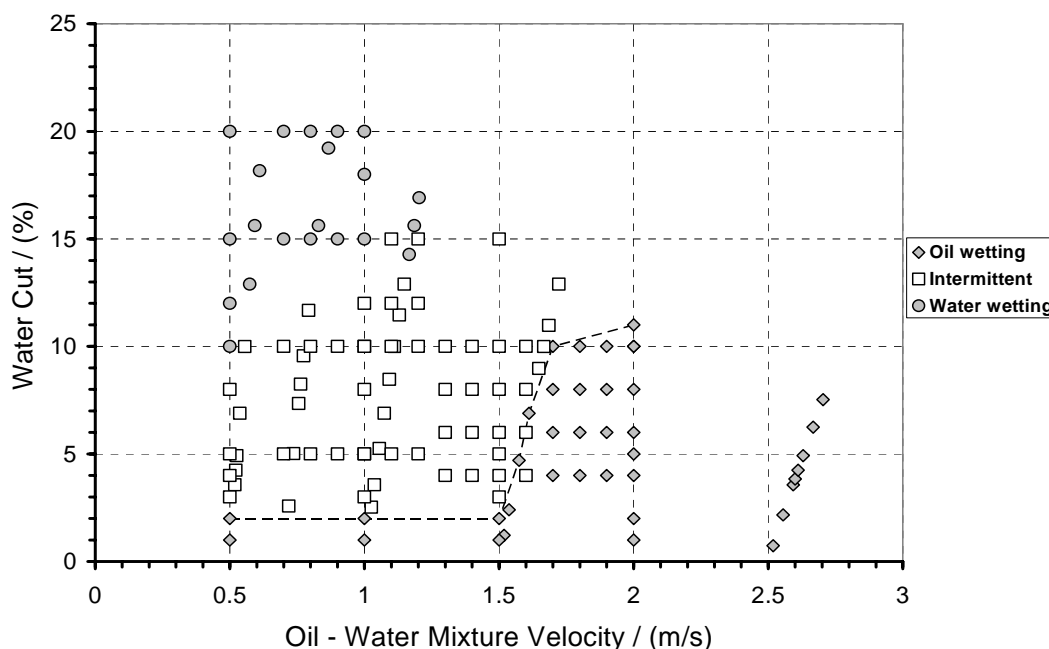


Figure 19 Phase wetting map of model oil-brine in horizontal, 4 inch pipe flow. The dotted line shows a transition from intermittent to oil wetting.

Water wetting prevails at water cut higher than 10% and oil-water mixture velocity less than 1.5 m/s. It can be seen that the higher mixture velocity requires higher water cut to give stable water wetting. At the same mixture velocity range, intermittent wetting is dominant at water cut less than 10%. Under such flow conditions, there is insufficient turbulent oil flow to sustain all the water droplets in the oil and not enough water to coalesce between droplets and break out from the oil phase to form a continuous water layer. Oil wetting occurs at mixture velocity higher than 1.5 m/s, which gives sufficient turbulent kinetic energy to entrain the water phase. It is interesting to see that it requires much lower mixture velocity, 0.5 m/s to produce oil wetting when the water cut is 2% or lower. Comparing flow pattern map (Figure 16) and phase wetting map (Figure 19), oil wetting can only happen when water-in-oil fully dispersed flow

forms. Water wetting is observed under stratified flow and intermittent wetting can occur under every flow pattern except for fully dispersed flow.

The phase wetting map is very useful as a guideline to assess the risk of internal corrosion in oil transportation pipeline. It also proves that some empirical rules practically used in the oil and gas industry are invalid, such as 1 m/s oil velocity can entrain and carry water up to 20% (Smith *et al.*, 1987) and oil wetting prevails at water cut lower than 30% (Adams *et al.*, 1993). It should be noted that the phase wetting map shown in Figure 19 is not universal. It is obtained for the specific model oil (LVT 200) and brine (1 wt% NaCl water) in horizontal, 4 inch pipe flow. No chemical additives have been applied into either water or oil phase. The internal wall of test section has been polished to maintain clean steel surface. The effects of oil properties, pipe inclinations and chemicals (corrosion inhibitors) will be discussed later in this work.

The accuracy of results obtained from flow pattern visualization and wall conductance probes is cross checked by wall sampling measurements. Table 5 shows wall sampling results compared with flow patterns and phase wetting under different flow conditions.

In Table 5 the wall fluid samples, which contain pure water (100%), indicate a continuous water layer flowing at the bottom of the pipe. It is consistent with the water wetting regime determined by wall conductance probes and stratified with a mixing layer found by flow pattern visualization. Even if only 1% oil and 99% water are in the wall fluid samples, the occurrence of intermittent wetting is identified by wall conductance probes. Under such flow conditions, oil occasionally wets the bottom of the pipe wall

since the water phase flows as droplets at the bottom and no continuous water layer exists (see Figure 17). As the water cut increases, a higher water volume percentage in the wall fluid samples can be seen due to coalescence of water droplets, which sink towards the bottom of the pipe. Increasing oil-water mixture velocity leads to decreasing water volume percentage in the wall fluid samples. At higher oil flow more water is entrained in the continuous oil phase and more oil penetrates towards the bottom of the pipe. When the mixture velocity is higher than 1.5 m/s, an unstable water-in-oil dispersion is found in the wall fluid sample. It is consistent with semi-dispersion found by flow pattern visualization. The water concentration is measured after complete sample separation. It is found that when the water concentration in the sample is 20% or lower, the water-in-oil dispersion at the bottom of pipe agrees well with the oil wetting indicated by wall conductance probes. However, when the water concentration in the sample is 40% or higher, the local flow pattern at the bottom of pipe becomes the transition zone between water-in-oil dispersion and oil-in-water dispersion since the phase inversion point for this particular model oil (LVT 200) is around 45% to 50% (Shi, 2001). The bottom of the pipe is periodically wetted by oil and water, which is consistent with the intermittent wetting regime measured with wall conductance probes. Oil wetting and fully dispersed flow are achieved when the water volume percentage is 10% or less in the sample. The *in situ* water cut in the sample is close to the input water cut, which confirms the uniform distribution of water concentration in the fully dispersed flow.

Table 5 Comparison of wall sampling results with flow patterns and phase wetting regimes obtained in the model oil-brine horizontal pipe flow.

Mixture velocity / (m/s)	Water cut / (%)	Flow pattern	Phase wetting	Wall sampling / (% water)
0.519	3.6	ST w/ water droplets	Intermittent	99
0.556	10	ST w/ water droplets	Intermittent	99
0.719	2.6	ST w/ water droplets	Intermittent	99
0.774	9.6	ST w/ water droplets	Intermittent	99
1.019	1.8	ST w/ water droplets	Intermittent	5
1.093	8.5	ST w/ water droplets	Intermittent	99
0.574	12.9	Smooth stratified	Water wetting	100
0.793	11.7	Smooth stratified	Intermittent	100
1.11	10	Smooth stratified	Intermittent	99
0.593	15.6	ST w/ mixing layer	Water wetting	100
0.61	18.2	ST w/ mixing layer	Water wetting	100
0.83	15.6	ST w/ mixing layer	Water wetting	100
0.87	19.2	ST w/ mixing layer	Water wetting	100
1.13	11.5	ST w/ mixing layer	Intermittent	99
1.15	12.9	ST w/ mixing layer	Intermittent	99
1.2	16.9	ST w/ mixing layer	Water wetting	100
1.61	6.9	Semi-dispersed	Oil wetting	20
1.65	9	Semi-dispersed	Intermittent	40
1.72	12.9	Semi-dispersed	Intermittent	60
1.519	1.2	Fully dispersed	Oil wetting	1
1.574	4.7	Fully dispersed	Oil wetting	10
2.556	2.2	Fully dispersed	Oil wetting	5
2.7	7.5	Fully dispersed	Oil wetting	2

The phase wetting regime in oil-water two-phase pipe flow can also be indicated by the corrosion rate. Since the water phase is saturated with CO<sub>2</sub> and CO<sub>2</sub> corrosion causes the corrosion product Fe<sup>2+</sup> concentration to increase in the water phase, when the carbon steel test section inner surface is wetted by either continuous water layer or water droplets. Therefore, Fe<sup>2+</sup> concentration monitoring is conducted to check and confirm the phase wetting regimes found by wall conductance probes. A few flow conditions with known phase wetting regimes measured by other techniques are selected to measure the

corrosion rate. For each test condition, water samples are collected at water boot (see Figure 12) every 30 minutes in a 2.5-hour test under constant mixture velocity and water cut. The water phase pH is around 4.8. Figure 20 shows the results of CO<sub>2</sub> corrosion under different phase wetting regimes in model oil-brine horizontal pipe flow. It is found that a complete absence of corrosion is guaranteed only when oil wetting occurs. At the same mixture velocity, corrosion rate under water wetting is higher than that under intermittent wetting. The results demonstrate that phase wetting regime significantly affects the internal pipe corrosion rate and further confirm the accuracy of phase wetting regime measured by other techniques.

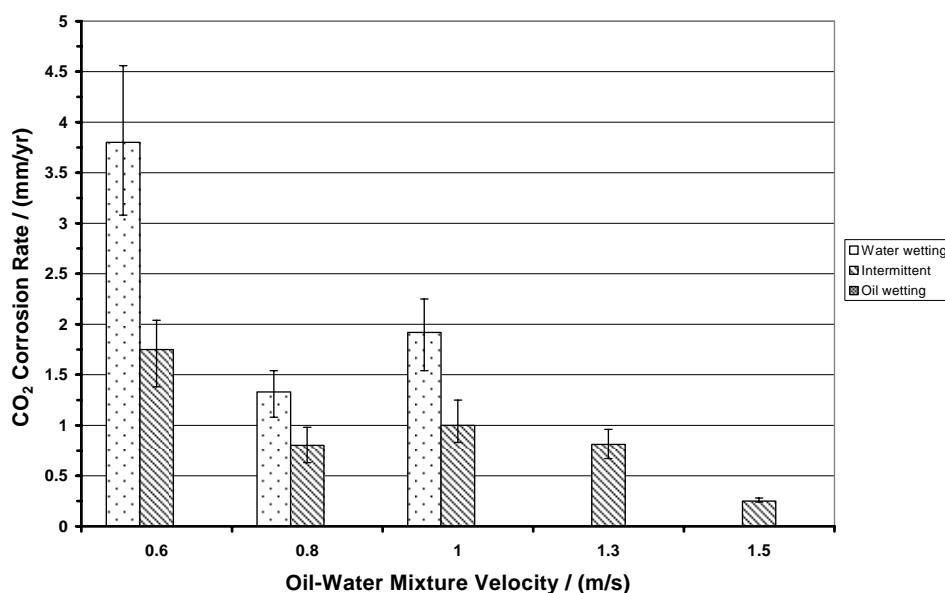


Figure 20 CO<sub>2</sub> corrosion rate measured with Fe<sup>2+</sup> concentration monitoring under different phase wetting regimes in model oil-brine horizontal pipe flow.

Five different crude oils (C1 to C5) were tested in the multiphase flow loop following the same test method as for model oil. All measurements by different test

techniques are cross checked with each other to strengthen confidence on the phase wetting map results. Since no flow pattern visualization is conducted for crude oil tests, the water phase is not dyed with either red food color or fluorescein.

Figure 21 shows the phase wetting map of C1 crude oil-brine in horizontal pipe flow. It is seen that intermittent wetting occurs in the range of mixture velocity 0.6 to 0.8 m/s even when the water cut is as low as 1%. For this water cut, the transition between oil wetting and intermittent wetting takes place at 0.9 m/s. Water wetting prevails at water cut higher than 10% and mixture velocity of 1 m/s or less. It is interesting to see that even 2 m/s mixture velocity is unable to fully entrain 10% water cut and still leads to intermittent wetting. The comparison of wall sampling results with phase wetting regimes obtained from wall conductance probes for C1 crude-brine pipe flow is shown in Table 6. The interpretation of this table is the same as for model oil-brine pipe flow tests (Table 5). The measured CO<sub>2</sub> corrosion rate for C1 crude-brine under water wetting (0.7 m/s mixture velocity and 15% water cut) is 2.3 mm/yr. The results from these three different measurement techniques are consistent with each other.

Figure 22 shows the phase wetting map of C2 crude oil-brine in horizontal pipe flow. No oil wetting is observed at mixture velocity of 0.6 m/s and water cut of 1% or higher. However, by increasing the mixture velocity from 0.6 to 0.7 m/s, up to 3% water can be entrained to achieve oil wetting. Table 7 shows the comparison of wall sampling results with phase wetting regimes indicated by wall conductance probes under different flow conditions. At 0.7 m/s mixture velocity and 3% water cut, where oil wetting occurs according to wall conductance probe measurement, only 5% water is observed in the

sample. However, by increasing the water cut to 5% at the same mixture velocity, the water concentration in the sample increases to 90%, which indicates intermittent wetting. Further increase in water cut up to 8%, water wetting occurs and leads to 99% water concentration in the sample. The results between wall conductance probes and wall sampling are cross validated to give consistent information. It also indicates that the transition of phase wetting regime highly depends on hydrodynamic parameters, like water cut and mixture velocity. The CO<sub>2</sub> corrosion rate for C2 crude-brine pipe flow under water wetting is double of that under intermittent wetting (Table 8).

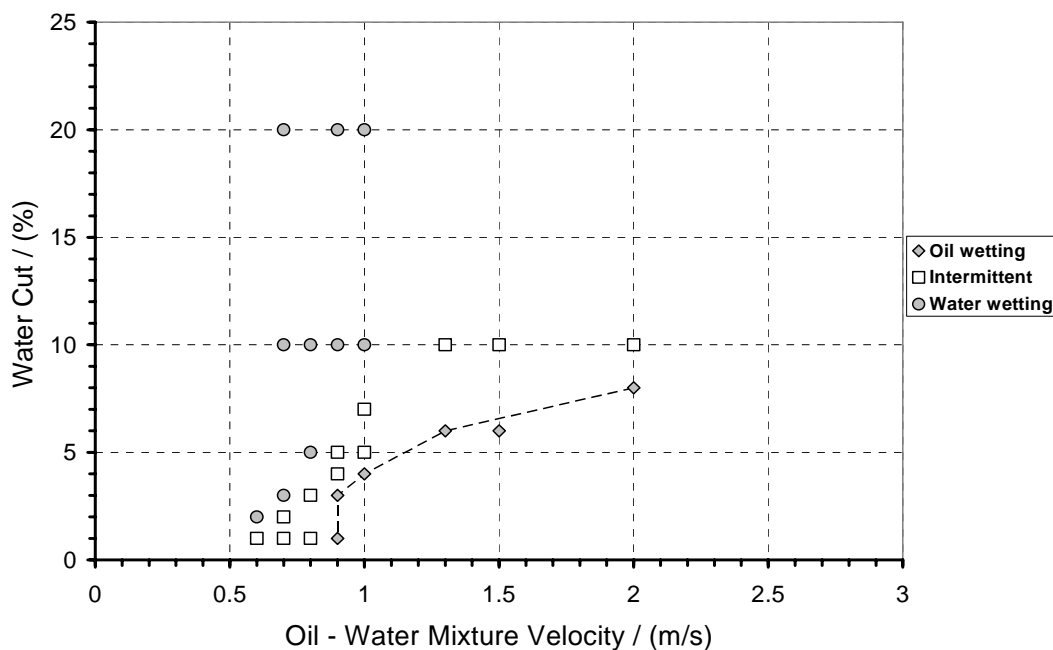


Figure 21 Phase wetting map of C1 crude oil-brine in horizontal pipe flow. The dotted line shows a transition from intermittent to oil wetting.

Table 6 Comparison of wall sampling results with phase wetting regimes obtained in the C1 crude oil-brine horizontal pipe flow.

Mixture velocity / (m/s)	Water cut / (%)	Phase wetting	Wall sampling / (% water)
0.8	1	Intermittent	60
0.8	4	Intermittent	80
0.8	5	Water wetting	90
0.8	10	Water wetting	99
0.9	3	Oil wetting	10
0.9	5	Intermittent	80
0.9	10	Water wetting	99
1	4	Oil wetting	5
1	7	Intermittent	80
1	10	Water wetting	95
1.3	6	Oil wetting	5
1.3	10	Intermittent	70
1.5	6	Oil wetting	5
1.5	10	Intermittent	70
2	8	Oil wetting	5
2	10	Intermittent	50

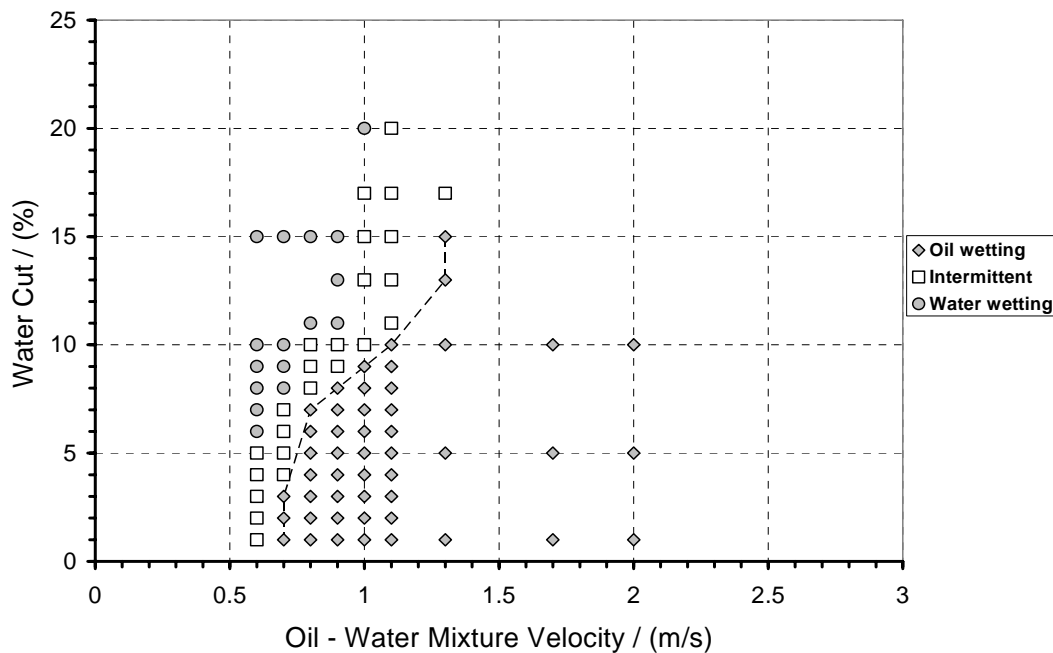


Figure 22 Phase wetting map of C2 crude oil-brine in horizontal pipe flow. The dotted line shows a transition from intermittent to oil wetting.

Table 7 Comparison of wall sampling results with phase wetting regimes obtained in the C2 crude oil-brine horizontal pipe flow.

Mixture velocity / (m/s)	Water cut / (%)	Phase wetting	Wall sampling / (% water)
0.6	5	Intermittent	90
0.6	8	Water wetting	99
0.7	3	Oil wetting	5
0.7	5	Intermittent	90
0.7	8	Water wetting	99
0.8	5	Oil wetting	5
0.8	8	Intermittent	90
0.8	15	Water wetting	99
0.9	8	Oil wetting	10
0.9	10	Intermittent	90
0.9	15	Water wetting	99
1	8	Oil wetting	10
1	10	Intermittent	80
1	20	Water wetting	99
1.3	15	Oil wetting	8
1.3	17	Intermittent	80

Table 8 CO<sub>2</sub> corrosion rate under different phase wetting regimes in C2 crude oil-brine horizontal pipe flow.

Mixture velocity / (m/s)	Water cut / (%)	Phase wetting	Corrosion rate / (mm/yr)
0.9	4	Oil wetting	0
0.9	8	Intermittent	1.8
0.9	12	Water wetting	3.9

The phase wetting map of C3 crude oil-brine horizontal pipe flow is shown in Figure 23. It can be seen that the low water cut region (<5%) is not covered in the tests since at 7% the water is already fully entrained at mixture velocity of 0.5 m/s. The wall sampling and CO<sub>2</sub> corrosion rate results are shown in Table 9 and Table 10, respectively.

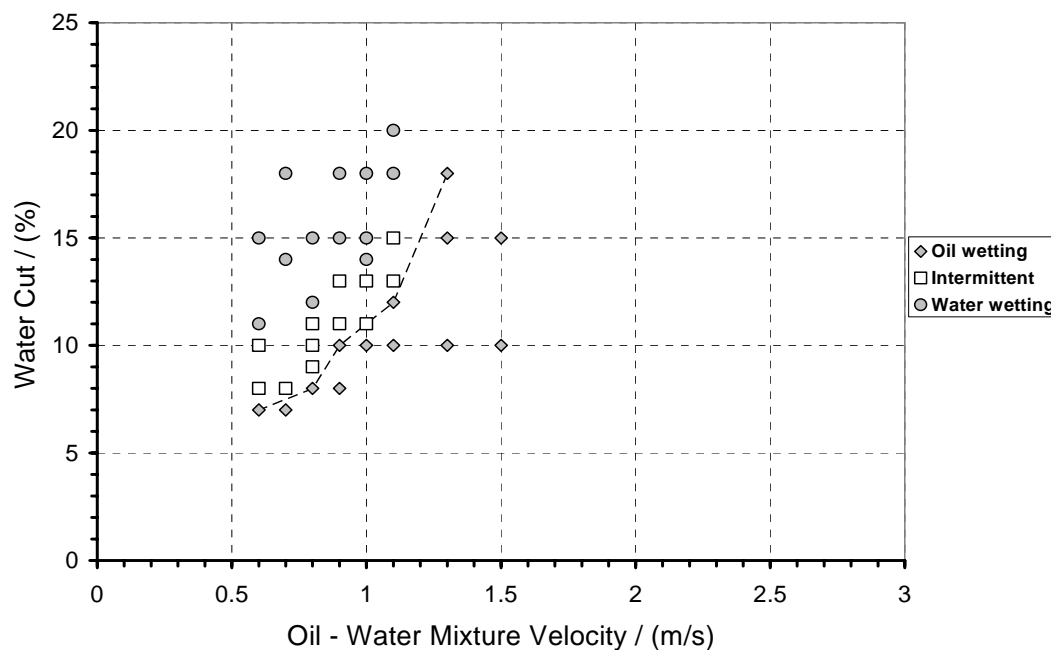


Figure 23 Phase wetting map of C3 crude oil-brine in horizontal pipe flow. The dotted line shows a transition from intermittent to oil wetting.

Table 9 Comparison of wall sampling results with phase wetting regimes obtained in the C3 crude oil-brine horizontal pipe flow.

Mixture velocity / (m/s)	Water cut / (%)	Phase wetting	Wall sampling / (% water)
0.6	7	Oil wetting	5
0.6	10	Intermittent	70
0.6	15	Water wetting	99
1	10	Oil wetting	5
1	13	Intermittent	80
1	15	Water wetting	95

Table 10 CO<sub>2</sub> corrosion rate under different phase wetting regimes in C3 crude oil-brine horizontal pipe flow.

Mixture velocity / (m/s)	Water cut / (%)	Phase wetting	Corrosion rate / (mm/yr)
0.6	5	Oil wetting	0
0.6	8	Intermittent	1.3
0.6	15	Water wetting	2.8

Figure 24 shows the phase wetting map of C4 crude oil-brine in horizontal pipe flow. It is shown that oil wetting dominates in the whole test range of the water cut when the mixture velocity is over 1 m/s. During the tests, it is found that oil-water emulsion forms at mixture velocity of 1.1 m/s and higher. The oil-water separator gives the separation efficiency is too low for this tight oil-water emulsion. Once this emulsion flows through the test sections, wall conductance probes always indicate oil wetting regime, which identify the type of emulsion as water-in-oil. The wall sampling results confirm the conclusion from wall conductance probes, shown in Table 11. The samples obtained under 1.3 m/s mixture velocity need to sit for a few days to allow the oil and water to completely separate.

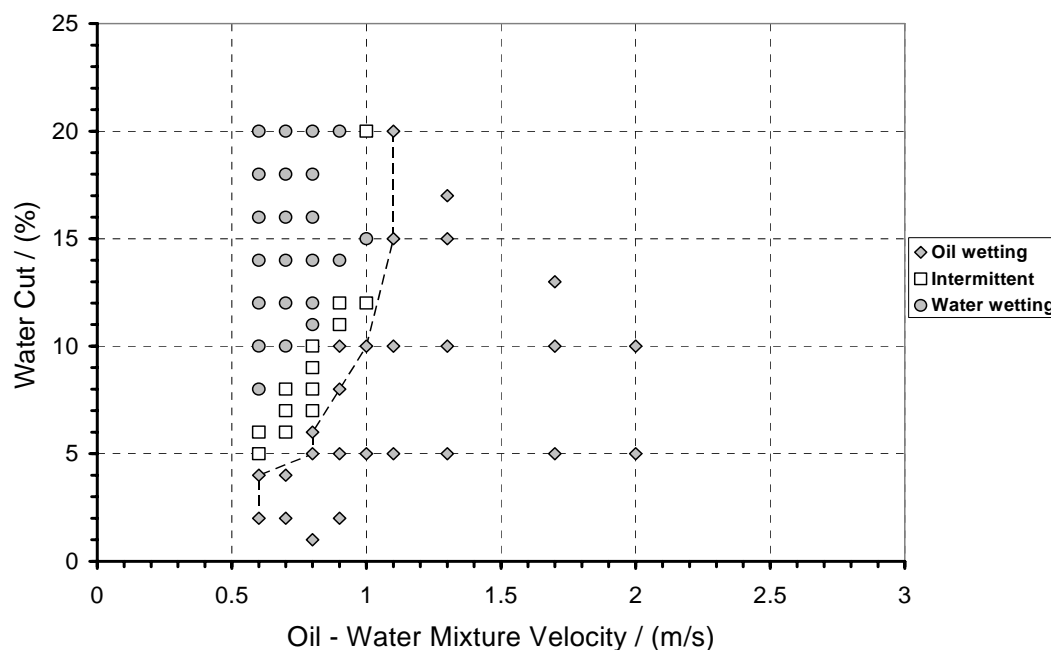


Figure 24 Phase wetting map of C4 crude oil-brine in horizontal pipe flow. The dotted line shows a transition from intermittent to oil wetting.

Table 11 Comparison of wall sampling results with phase wetting regimes obtained in the C4 crude oil-brine horizontal pipe flow.

<b>Mixture velocity / (m/s)</b>	<b>Water cut / (%)</b>	<b>Phase wetting</b>	<b>Wall sampling / (% water)</b>
0.6	2	Oil wetting	1
0.6	5	Intermittent	50
0.6	15	Water wetting	99
0.9	10	Oil wetting	5
0.9	12	Intermittent	60
0.9	15	Water wetting	95
1	10	Intermittent	60
1	15	Intermittent	70
1.3	15	Oil water	5

The corrosion measurement for C4 crude oil with brine at mixture velocity of 1 m/s and water cut of 5%, shows that absence of corrosion is achieved due to being under an oil wetting condition. Electrical resistance (ER) probe is mounted on the upstream test section to monitor CO<sub>2</sub> corrosion rate under C4 crude oil-brine emulsion formation conditions. In emulsion tests, oil and water are all stored in the oil tank with desired water cut. Bypass tubing is used to let the mixture circulate in the flow loop to create oil-water emulsion bypassing the oil-water separator. Table 12 shows the corrosion rates in emulsion tests at different mixture velocities, water cuts and pipe inclinations. It is clear that negligible corrosion rates are found at all test conditions. No effect of pipe inclination and mixture velocity on corrosion rate under emulsion formation condition is observed. From the corrosion point of view, it is important to identify the transition from negligible corrosion to moderate corrosion. Table 13 shows C4 crude oil-brine emulsion corrosion rates at high water cut (40% to 60%) measured by ER probe horizontal pipe

flow. Under emulsion formation, even up to 50% water it only finds negligible corrosion rate. The transition from oil wetting to intermittent occurs at water cut of 50 to 55%.

Table 12 CO<sub>2</sub> corrosion rate measured by ER probe under C4 crude oil-brine emulsion formation in flow loop tests with pipe inclinations.

Mixture velocity / (m/s)	Water cut / (%)	Corrosion rate / (mm/yr)			
		horizontal	+5°	+25°	+45°
1	10	0.02	0.05	0	---
1	15	0	0.05	0.1	---
1	20	---	0.1	0	0.1
2	10	0.02	0.01	---	---
2	15	0	0	0.07	---
2	20	---	---	0.01	0.1

Table 13 CO<sub>2</sub> corrosion rate measured by ER probe under C4 crude oil-brine emulsion formation in horizontal flow loop tests with high water cut.

Mixture velocity / (m/s)	Water cut / (%)	Corrosion rate / (mm/yr)
1	40	0
1	50	0.08
1	55	0.34
1	60	0.36

Figure 25 shows the phase wetting map of C5 crude oil-brine in horizontal pipe flow. Small scale tests indicate that emulsion forms for this C5 crude in a similar way as for C4 crude around mixture velocity of 1 m/s (Cai *et al.*, 2005b) and therefore no measurements were made at mixture velocity higher than 1 m/s. Full phase wetting map is achieved nonetheless since full oil wetting is achieved at mixture velocities below 1 m/s. Water wetting only occurs at 15% to 20% water cut in the range of mixture velocity 0.5 to 0.6 m/s. Table 14 shows wall sampling results for C5 crude oil. CO<sub>2</sub> corrosion rates

under emulsion free conditions for C5 crude oil-brine pipe flow are shown in Table 15. The corrosion rates measured by ER probe in horizontal pipe flow under C5 crude oil-brine emulsion forming conditions are shown in Table 16. It is seen that low corrosion rate remains even up to water cut of 70%.

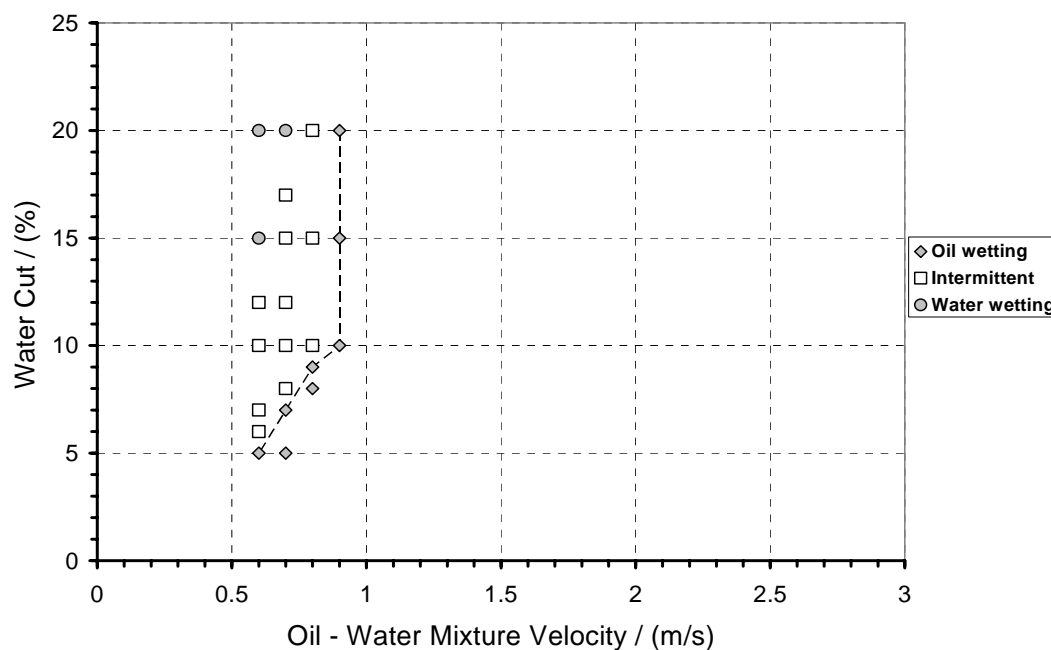


Figure 25 Phase wetting map of C5 crude oil-brine in horizontal pipe flow. The dotted line shows a transition from intermittent to oil wetting.

Table 14 Comparison of wall sampling results with phase wetting regimes obtained in the C5 crude oil-brine horizontal pipe flow.

Mixture velocity / (m/s)	Water cut / (%)	Phase wetting	Wall sampling / (% water)
0.6	5	Oil wetting	10
0.6	10	Intermittent	70
0.6	15	Water wetting	95
0.8	9	Oil wetting	5
0.8	15	Intermittent	80
0.9	15	Oil wetting	Stable emulsion

Table 15 CO<sub>2</sub> corrosion rate under different phase wetting regimes in C5 crude oil-brine horizontal pipe flow.

Mixture velocity / (m/s)	Water cut / (%)	Phase wetting	Corrosion rate / (mm/yr)
0.6	5	Oil wetting	0
0.6	10	Intermittent	1.3
0.6	15	Water wetting	2.7

Table 16 CO<sub>2</sub> corrosion rate measured by ER probe under C5 crude oil-brine emulsion formation in horizontal flow loop tests with water cut from 20 to 70%.

Mixture velocity / (m/s)	Water cut / (%)	Corrosion rate / (mm/yr)
0.9	20	0
0.9	40	0.01
0.9	50	0.02
0.9	60	0.05
0.9	70	0.1

The results of corrosion rates by both Fe<sup>2+</sup> concentration monitoring and ER probe measurements show that a complete absence of corrosion is guaranteed only when the oil wetting regime occurs. Under water wetting and intermittent wetting, internal pipe corrosion can happen. From the corrosion point of view, it is essential to determine the transition from intermittent to oil wetting, *i.e.*, from corrosion to corrosion-free condition. The effect of oil properties and pipe inclination on this transition will be discussed as in the following section.

A transition line from intermittent wetting to oil wetting on the phase wetting map of each tested oil is determined conservatively. The method consists of determining the transition points based on the oil phase velocities of a full water entrainment at a given water cut. In other words, the test points in the oil wetting region closest to the intermittent wetting are identified as the transition points. The transition line is composed

of the points, which are the boundary between intermittent wetting and oil wetting. As mentioned above, experimental errors are  $\pm 0.4\%$  in mixture velocity and  $\pm 0.13\%$  in water cut on each test point. Figure 26 shows the transition lines with the transition points from intermittent wetting to oil wetting for model oil and five different crude oils in horizontal pipe flow. It can be seen from the oil properties (Table 4) that the crude oils have lower oil-water interfacial tension (23-31 dyne/cm) than the model oil (40 dyne/cm). According to water entrainment theory (Chapter 2, Section 2.2), lower value of the oil-water interfacial tension leads to easier entrainment of the water phase in the flowing oil phase. It is verified with the results in Figure 26 since the transition lines of the crude oils are toward lower mixture velocity at a given water cut compared to the transition line of model oil. The transition line of C1 crude shows a tendency for entraining less water than the model oil when the mixture velocity is above 1.6 m/s. It could be explained by C1 crude oil being lighter (lower density and lower viscosity) than model oil. Comparing crude oils from C1 to C5, they are arranged from light crude to heavy crude (higher density and higher viscosity). High density oils, particularly when the density of oil is close to the density of water, will entrain water droplets more easily, since the gravity effect on the separation of water droplets from continuous oil phase is diminished (Equations 2-48 and 2-49). It is believed that the viscosity of the oil plays an important role in the momentum exchange between oil and water. Higher viscosity oil entrains the water more easily. Figure 26 shows that the transition lines shift to lower mixture velocity at a given water cut from C1 to C5 crude oils due to higher densities and viscosities. It is also interesting to note that transition lines of C2, C3, C4 and C5 crude

oils are overlapping with each other at water cut below 10% and mixture velocity between 0.5 to 0.8 m/s.

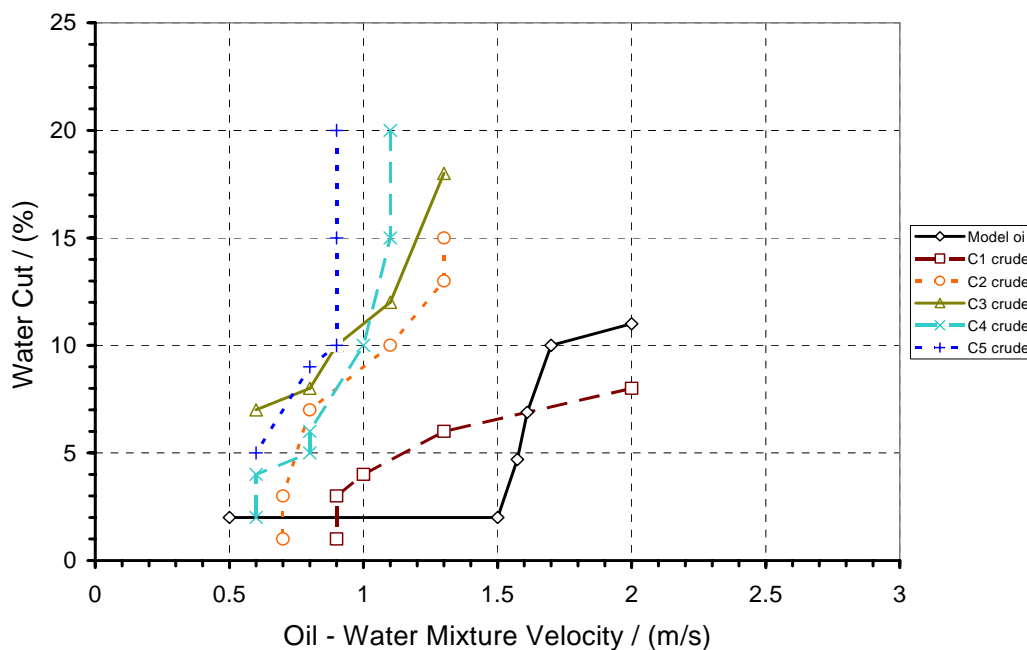


Figure 26 Comparison of transition lines from intermittent to oil wetting for model oil and five different crude oils in horizontal, 4 inch pipe flow.

In order to study the effect of pipe inclinations on phase wetting, a series of experiments were conducted with crude oils in inclined pipe flow. The phase wetting maps of each of the crude oils in the inclined pipe flow are built based on the measurements from wall conductance probes. The transition lines from intermittent wetting to oil wetting are determined in the same way as horizontal pipe flow. A positive value for pipe inclination represents results from upstream test section and a negative value denotes results from downstream test section. Figure 27 and Figure 28 show a comparison of transition lines including the transition points from intermittent to oil

wetting for C1 crude oil-brine in horizontal and inclined upstream and downstream pipe flows. For both upstream and downstream pipe flows, it is clear to see that no significant effect of pipe inclination on phase wetting transition is observed at near-horizontal (lower than  $5^\circ$ ) pipe flows. However, from  $5^\circ$  to  $45^\circ$  pipe inclination an obvious shift of the transition line to the higher water cut at a given mixture velocity can be seen. In the near-horizontal pipe flow the gravity force acting on the water phase tends to separate it from the oil phase; however, in inclined upstream or downstream pipe flow, the gravity force tends to pull the fluids back or to accelerate the flow. In either case, it causes smaller water droplets to be formed due to higher intensity of the turbulent energy. Similar effect of pipe inclination on phase wetting transition is observed for other crude oils. For example, Figure 29 and Figure 30 show comparisons of transition lines including transition points from intermittent wetting to oil wetting for C3 crude oil-brine in horizontal and inclined upstream and downstream pipe flows.

### **4.3 Summary**

Model oil and five crude oils have been tested in a large scale, 4-inch ID multiphase flow loop. Based on cross checking and overlapping results from four experimental techniques (wall conductance probes, flow pattern visualization, wall sampling and corrosion rate monitoring), phase wetting maps are built for each oil in horizontal and inclined pipe flows. The phase wetting maps can answer the key question of which phase (either water or oil) wets the bottom of pipe inner surface at different mixture velocities and water cuts in horizontal and inclined pipe flows.

Three types of phase wetting are found: water wetting, intermittent wetting and oil wetting. Flow pattern visualization results confirm two main categories of flow patterns (stratified and dispersed flows) as proposed by Trallero (1995). Three sub-categories in stratified flow have been determined stratified flow with water droplets flowing at the bottom, smooth stratified flow and stratified flow with mixing layer. Two sub-categories in dispersed flow are identified as semi-dispersed flow and fully dispersed flow. The results from different experimental techniques are consistent with each other. A complete absence of CO<sub>2</sub> corrosion is guaranteed when the oil wetting is achieved. Otherwise, water wetting and intermittent wetting lead to internal pipe corrosion. It is found that heavy crude oil (higher density and viscosity) has better entrainment capability compared to light crude oil. The transition line of heavy crude oil is shifted to the lower mixture velocity at given water cut on the phase wetting map. It is seen that low pipe inclinations (0° to ±5°) has no effect on phase wetting transition lines. However, water is easier to be entrained when the pipe inclination is over 45°.

Oil-water emulsion can be formed for C4 and C5 crude oils when the mixture velocity is higher than 1 m/s. The type of emulsion is determined by wall conductance probes and ER probe as water-in-oil. The minimum water cuts for transition from corrosion free to corrosion condition are identified by ER probe corrosion measurements.

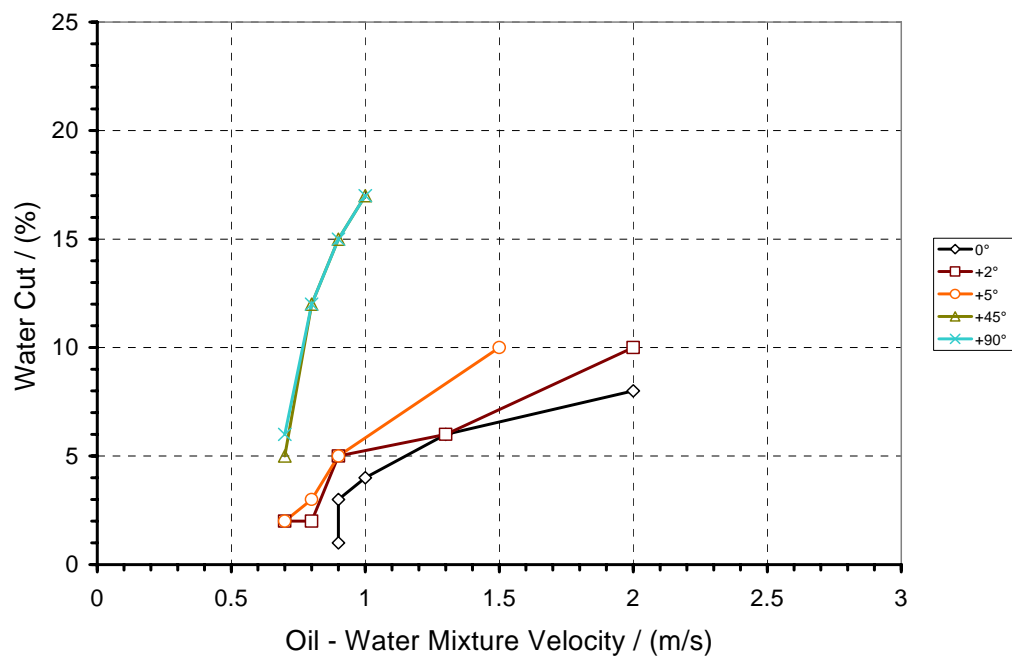


Figure 27 Comparison of transition lines from intermittent wetting to oil wetting for C1 crude oil-brine in horizontal and inclined upstream pipe flows.

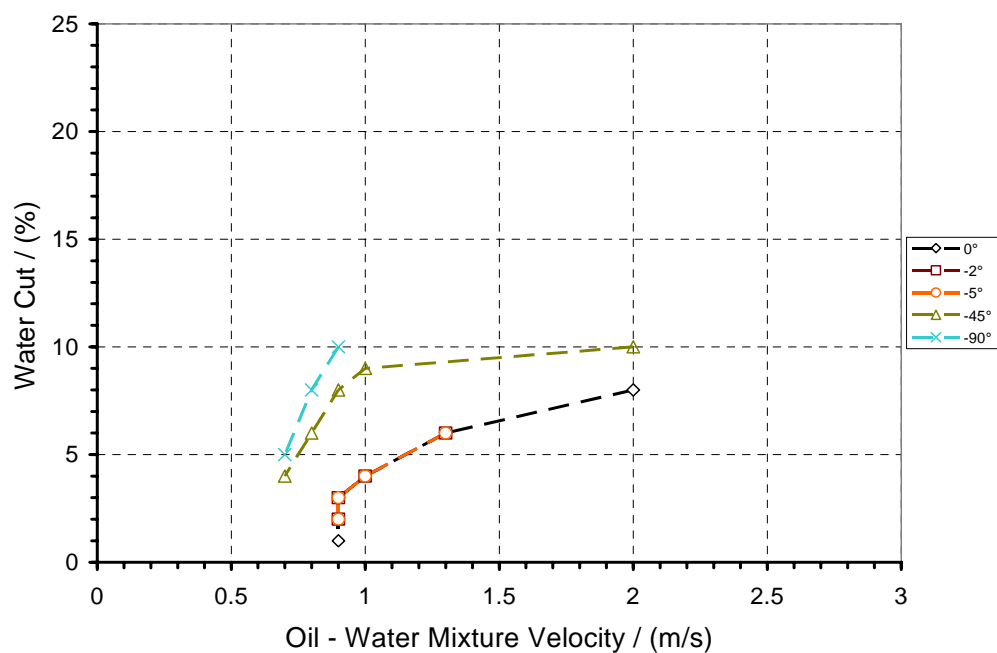


Figure 28 Comparison of transition lines from intermittent wetting to oil wetting for C1 crude oil-brine in horizontal and inclined downstream pipe flows.

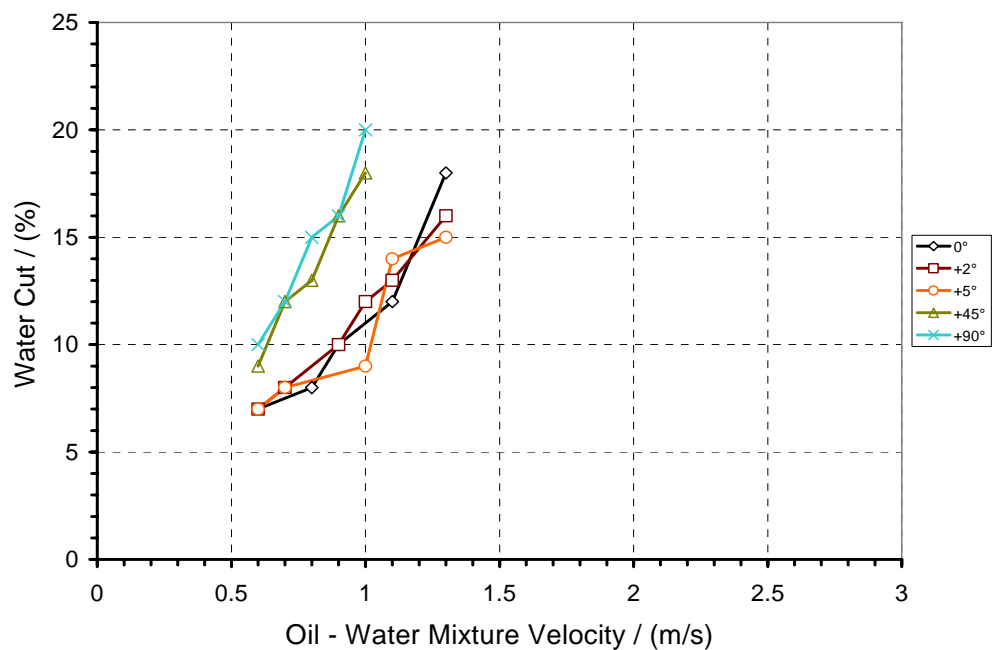


Figure 29 Comparison of transition lines from intermittent wetting to oil wetting for C3 crude oil-brine in horizontal and inclined upstream pipe flows.

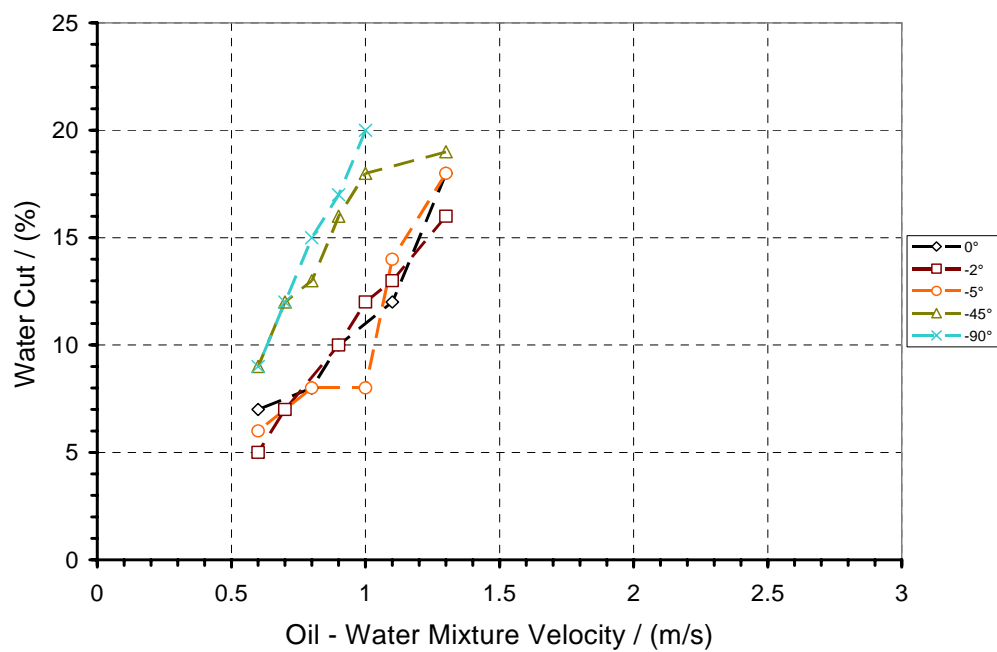


Figure 30 Comparison of transition lines from intermittent wetting to oil wetting for C3 crude oil-brine in horizontal and inclined downstream pipe flows

## CHAPTER 5: EXPERIMENTAL STUDY OF CARBON DIOXIDE CORROSION INHIBITION

### 5.1 Experimental setup and procedure

#### 5.1.1 Equipment

CO<sub>2</sub> corrosion inhibition experiments are conducted in a glass cell with a three electrode set-up (working, reference and counter electrodes). Figure 31 shows a schematic of glass cell test system set up with key components, marked and named. The fluid temperature is controlled by a thermocouple and a hotplate. A condenser is used to avoid loss of test fluid due to evaporation. CO<sub>2</sub> gas is continuously bubbled through a gas bubbler into the cell to keep the water phase saturated with CO<sub>2</sub>. CO<sub>2</sub> corrosion rates with and without inhibition are measured using an electrochemical technique and the baseline corrosion rate (without inhibition) is also checked using weight loss measurements. The electrochemical technique requires a three-electrode set-up. The working electrode made of ASTM 1018 carbon steel, which is representative of a pipeline material. The cylindrical shaped working electrode has a diameter of 1.18-cm, length of 1.46-cm and 5.41-cm<sup>2</sup> exposed area to fluid. The working electrode is also called a rotating cylinder electrode since it can be driven to rotate using a motor with adjustable speed controller. Faster rotation speed produces higher wall shear stress on the working electrode. A platinum ring is used as a counter electrode. A saturated Ag-AgCl connected with Luggin capillary serves as reference electrode. A pH probe is used to monitor the solution pH. A magnetic stirrer bar is used during the deoxygenation to mix the electrolyte.

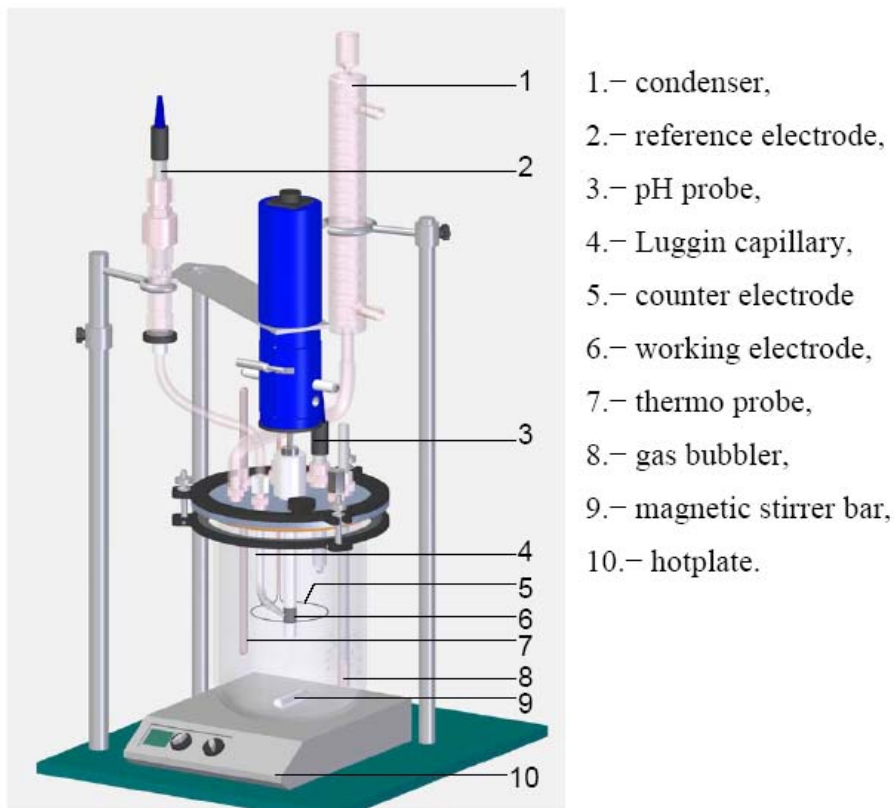


Figure 31 Schematic of glass cell set up (Courtesy of Jiabin Han).

### 5.1.2 Experimental procedure

Two-liters of deionized water with 1 wt% NaCl are put into the glass cell. Deoxygenation using CO<sub>2</sub> gas takes about 1.5 to 2 hours to reach oxygen concentration below 25-ppb. When the solution is saturated with CO<sub>2</sub>, the pH is between 3.8 and 3.9. Since pH of 5, which is in a typical range of pH found in oilfields, is selected in this work, sodium bicarbonate (NaHCO<sub>3</sub>) solution is added to adjust the pH. The working electrode is polished with 400- and 600-grit silicon carbide paper, while at the same time being rinsed with isopropanol. After polishing, it is cleaned with isopropanol in an ultrasonic bath, washed with isopropanol again and quickly dried with an air blower.

After being mounted on the working electrode holder, it is immediately immersed into the solution to avoid oxidation. The rotation speed is kept at 1000 rpm.

Initially, the open circuit potential (also called free corrosion potential) is monitored to allow stable conditions to be reached (usually in 5 to 10 minutes). The test duration is 20 to 30 hours. Linear polarization resistance (LPR) technique is conducted at 30 minute interval throughout the test to measure the corrosion rate. The polarizing range is  $\pm 5$  mV from the open circuit potential with scanning rate of 0.125 mV/s. The measured polarization resistance,  $R_p$ , is compensated with the solution resistance,  $R_s$ , measured by the electrochemical impedance spectroscopy (EIS) technique.

In the LPR technique, corrosion current density ( $i_{\text{corr}}$ , A/m<sup>2</sup>) is calculated using Equation (5-1), in which  $S_A$  is working electrode surface area (m<sup>2</sup>) and B is a constant (V). Corrosion rate (CR, mm/yr) can be calculated with corrosion current density using Equation (5-2), in which  $w$  is molecular weight of iron (56 g/mole), F is Faraday's constant (96485 C) and  $\rho_{Fe}$  is the density of material (7870 kg/m<sup>3</sup>). In the baseline tests (without inhibitor addition), the B value is obtained from the weight loss results. An initial weight of working electrode before putting into the solution and a final weight of it after taking out from the solution gives average corrosion rate in the test duration. In the corrosion inhibition tests (with inhibitor addition), the B value is determined from the Tafel slopes of anodic ( $\beta_a$ , mV) and cathodic ( $\beta_c$ , mV) polarization curves using Equation (5-3). To get Tafel slopes the potentiodynamic sweeps are conducted following the last measurement of LPR. The cathodic sweep starts from the open circuit potential and goes down to 300 or 400 mV below it where the sweep stops to allow corrosion potential to

reach to the open circuit potential. Then an anodic sweep is conducted from the open circuit potential to 150 mV above it. The scanning rate is 0.2 mV/s. All the electrochemical measurements are conducted using a Gamry Instrument connected to a laboratory computer.

$$i_{corr} = \frac{B}{S_A R_p} \quad (5-1)$$

$$CR = \frac{365 * 24 * 3600 * w * i_{corr}}{2 * F * \rho_{Fe}} = 1.16i_{corr} \quad (5-2)$$

$$B = \frac{\beta_a \beta_c}{2.303(\beta_a + \beta_c)} \quad (5-3)$$

In the inhibition test, a corrosion inhibitor is introduced into the cell with a syringe at 1.5 hour after the working electrode has been exposed to the solution. Three test series are conducted for the corrosion inhibition study:

1. Only the brine phase is present in the cell with no oil added. The performance of inhibitor is observed with different concentrations. This test is termed *pure corrosion inhibition* in this work.
2. The working electrode is immersed in the brine phase. The model oil is added on the top of the brine phase after injection of corrosion inhibitor into the cell. The volume ratio of model oil to brine is 1:9. The concentration of the inhibitor is calculated based on the total liquid volume of 2-liters. During experiments, the working electrode is periodically lifted up and stayed in the oil phase for 5 minutes keeping the 1000 rpm rotation. Then it is returned to the brine phase. Electrochemical

measurements can be only carried out in the brine phase. Since the electrode is wetted by an oil phase, this test series is referred to as *direct oil wet* in this work.

3. In this test series, after injection of corrosion inhibitor in the glass cell at test duration 1.5 hour, 5-mL and 20-mL of the model oil are separately added on the top of brine phase during the test duration. However, the working electrode is not lifted up in the experiments, *i.e.*, the electrode stays in the brine phase and is not physically exposed to the oil phase. It is called *partitioning test* in this work.

At the end of each experiment, the glass cell and other equipment are carefully washed with tap water, deionized water and isopropanol to avoid inhibitor contamination.

### 5.1.3 Test matrix

Two generic corrosion inhibitor packages provided by Champion Technologies are used in this study. The main active components in the two packages are quaternary ammonium chloride (“quat”) and fatty amino, respectively. Their general chemical structures are shown in Figure 32, but the details of their structures are proprietary. The formulations and solubility of two inhibitor packages are shown in Table 17 and Table 18. Acetic acid and methanol in the packages serve as solvent. Table 19 shows the test matrix of corrosion inhibition tests conducted in the glass cell. The chemical composition of ASTM 1018 carbon steel is shown in Table 20.

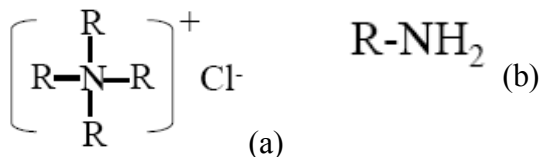


Figure 32 General chemical structures of the (a) quaternary ammonium chloride (“qua”) and (b) fatty amino compound. R represents a hydrocarbon chain in the structure.

Table 17 Compositions of fatty amino inhibitor package (as received from Champion Technologies).

Substance	Weight / (%)	Solubility
Fatty amino	60 - 80	Oil soluble/water dispersible
Acetic acid	10 - 30	
Methanol	5 - 10	

Table 18 Compositions of quaternary ammonium chloride inhibitor package (as received from Champion Technologies).

Substance	Weight / (%)	Solubility
Quaternary ammonium chloride	60 - 80	Water soluble
Methanol	10 - 30	

Table 19 Test matrix of corrosion inhibition test series conducted in glass cell.

<b>Working electrode material</b>	ASTM 1018 carbon steel
<b>Temperature / (°C)</b>	25
<b>Total pressure / (bar)</b>	1.013
<b>Partial pressure of CO<sub>2</sub> / (bar)</b>	0.96
<b>Brine solution</b>	Deionized water with 1 wt% NaCl
<b>Oil phase</b>	Model oil (LVT 200)
<b>pH of brine solution</b>	5.0
<b>Electrode rotating speed / (rpm)</b>	1000
<b>Inhibitor type</b>	Quaternary ammonium chloride and fatty amino
<b>Inhibitor concentration / (ppm)</b>	0 - 200

Table 20 Chemical composition of ASTM 1018 carbon steel.

C	Si	P	S	Mn	Al	Fe
0.21	0.38	0.09	0.05	0.05	0.01	Balance

## 5.2 Results and discussion

### 5.2.1 Pure corrosion inhibition tests

Two separate weight loss tests are conducted for measuring corrosion rates of the baseline tests (no inhibition). The measured corrosion rates of 1.29 and 1.38 mm/yr give an average B value of 20.7 mV, which is used in the LPR measurement results for baseline tests. The potentiodynamic sweeps for 100 ppm “quat” is shown in Figure 33. It gives corrosion current of 0.094 A/m<sup>2</sup> (square point) and B value of 20.7 mV with measured polarization resistance by LPR gives corrosion current of 0.141 A/m<sup>2</sup> (round point). It is acceptable to use the B value of 20.7 mV for LPR results obtained from “quat” inhibitor tests. Figure 34 shows the potentiodynamic sweeps for 100 ppm fatty amino from pure corrosion inhibition test. The corrosion current density of 0.042 A/m<sup>2</sup> (square point) is determined with Tafel slopes, which give the B value of 30.9 mV. The measured polarization resistance by LPR gives corrosion current density of 0.058 A/m<sup>2</sup> (round point). The difference is acceptable to allow the B value of 30.9 mV to be used for LPR results in the fatty amino inhibitor tests.

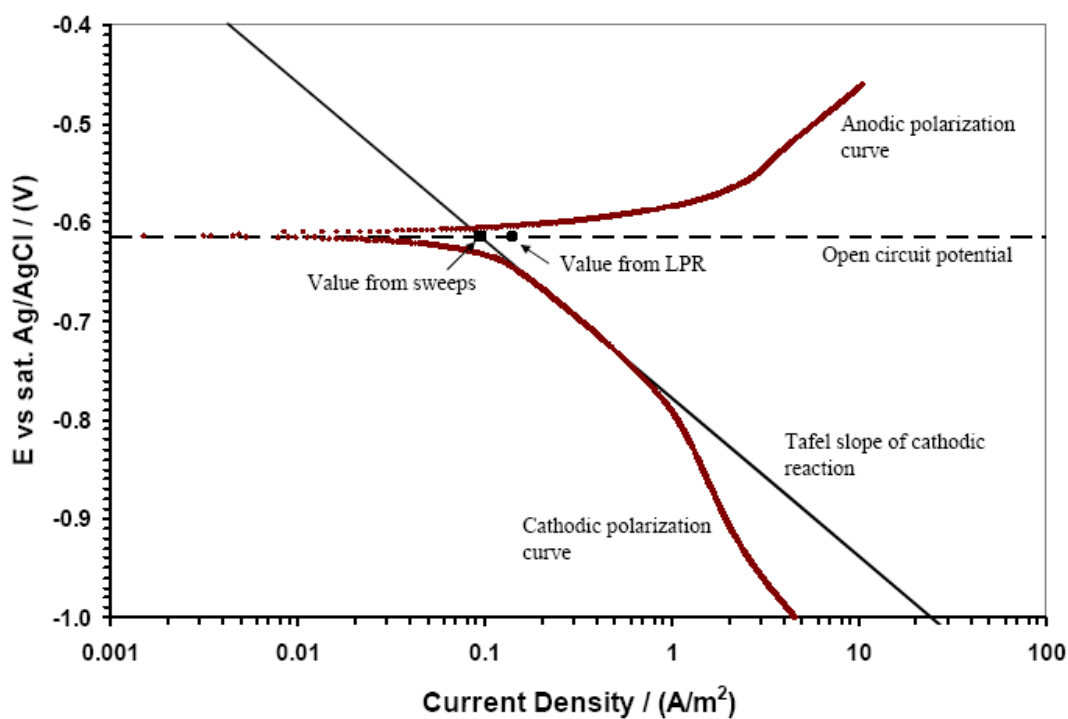


Figure 33 Potentiodynamic sweeps for 100 ppm "quat" pure inhibition test.

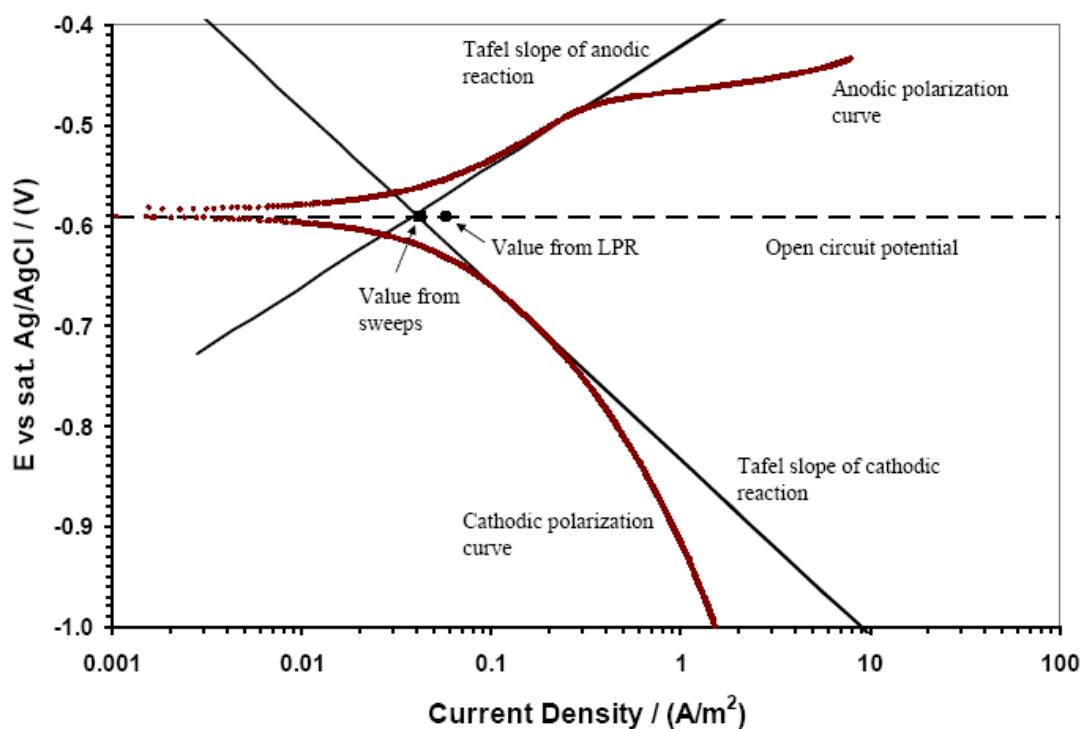


Figure 34 Potentiodynamic sweeps for 100 ppm fatty amino pure inhibition test.

Figure 35 and Figure 36 show corrosion rates obtained in the pure corrosion inhibition tests for “quat” and fatty amino at different addition concentrations, respectively. The vertical dotted lines in the figures indicate the time point (1.5h) of inhibitor added during the tests. In the baseline test (no inhibitor addition), CO<sub>2</sub> corrosion rate steadily increase with time since the corrosion process leaves iron carbide left on the working electrode surface, which increases surface area of cathodic reaction and further increases the corrosion rate. Figure 37 shows a summary of corrosion rate and inhibition efficiency vs. inhibitor concentration for “quat” and fatty amino in pure corrosion inhibition tests. Inhibition efficiency is found below 60% with addition of inhibitor “quat” up to 20 ppm. Increasing “quat” concentration to 30 ppm or 40 ppm, higher inhibition efficiency between 76 to 83% is achieved. Between 40 to 60 ppm, corrosion rate is not further decreased. But increasing the concentration from 100 to 200 ppm helps reduce CO<sub>2</sub> corrosion to 94% inhibition efficiency. It is found that fatty amino gives 85% inhibition efficiency when only 2 ppm is added in the brine phase. Over 90% efficiency can be obtained at 5 ppm and higher. It also takes shorter time for fatty amino to reach steady corrosion inhibition than the “quat”.

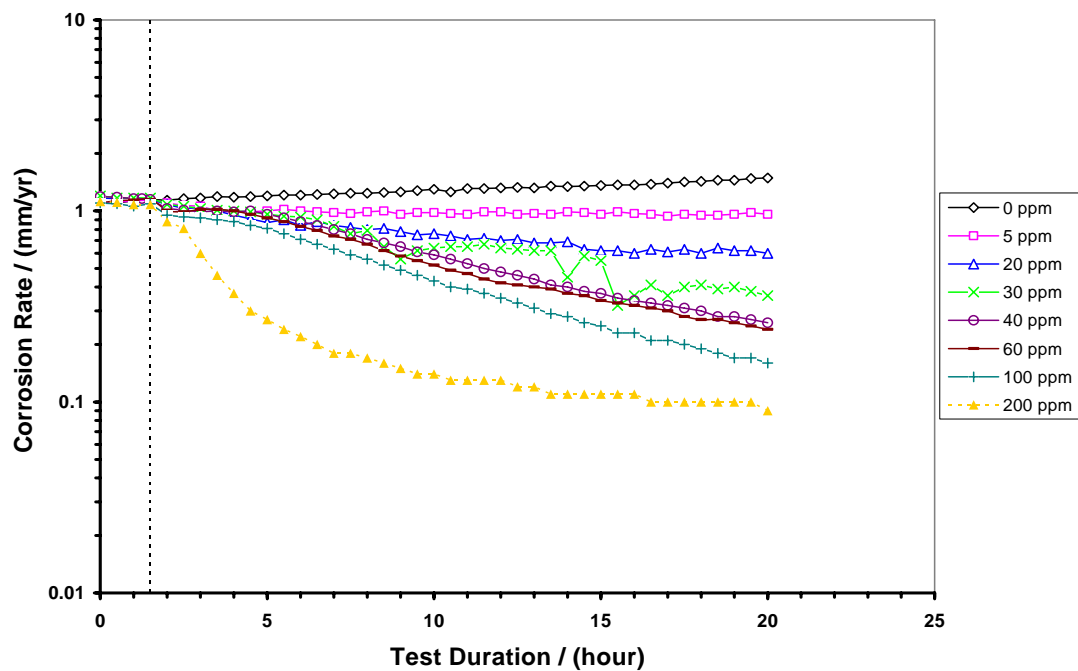


Figure 35 Corrosion rates measured by LPR for “quat” pure corrosion inhibition tests at different concentrations. The vertical dotted line indicates inhibitor addition time.

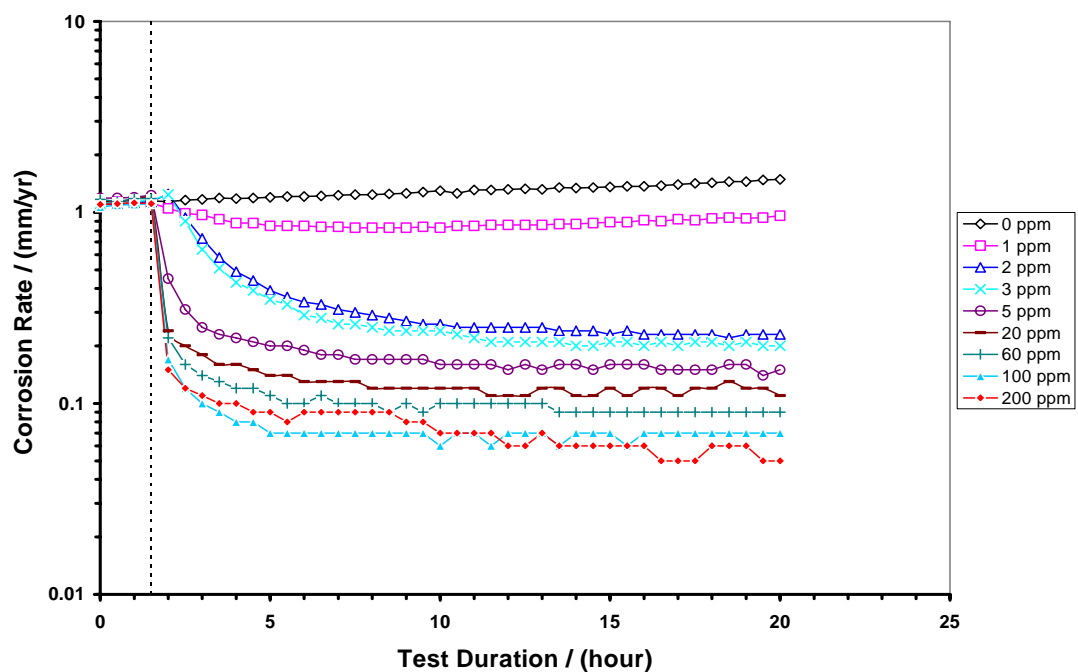


Figure 36 Corrosion rates measured by LPR for fatty amino pure corrosion inhibition tests at different concentrations. The vertical dotted line indicates inhibitor addition time.

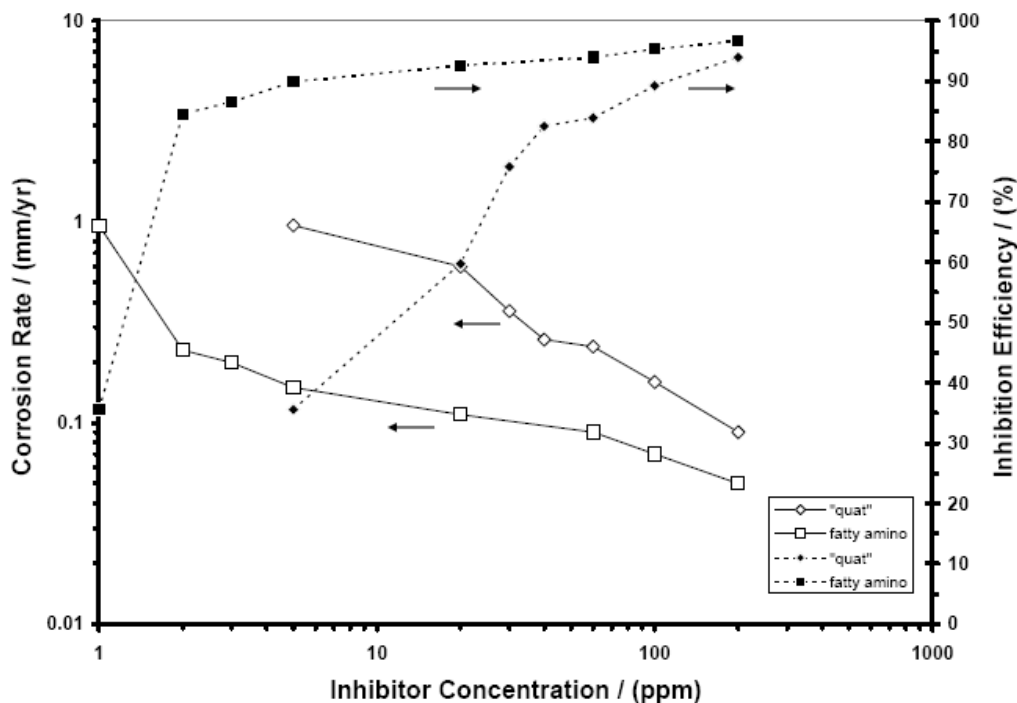


Figure 37 Summary of corrosion rate and inhibition efficiency versus inhibitor concentration for “quat” and fatty amino inhibitors in pure corrosion inhibition tests.

In Figure 38 potentiodynamic sweeps at different concentrations of “quat” inhibitor in pure corrosion inhibition tests are compared. As consistent with results gotten with the LPR technique, inhibition of anodic and cathodic reactions is not obvious to see at 5 ppm concentration of inhibitor. Increasing the concentration up to 30 to 60 ppm, one can see that the inhibitor is mostly affecting the anodic reaction by slowing it down. There is still no obvious inhibition on the cathodic reaction. When the concentration is increased from 60 to 200 ppm, the inhibition on the cathodic reaction is much stronger than on anodic reaction.

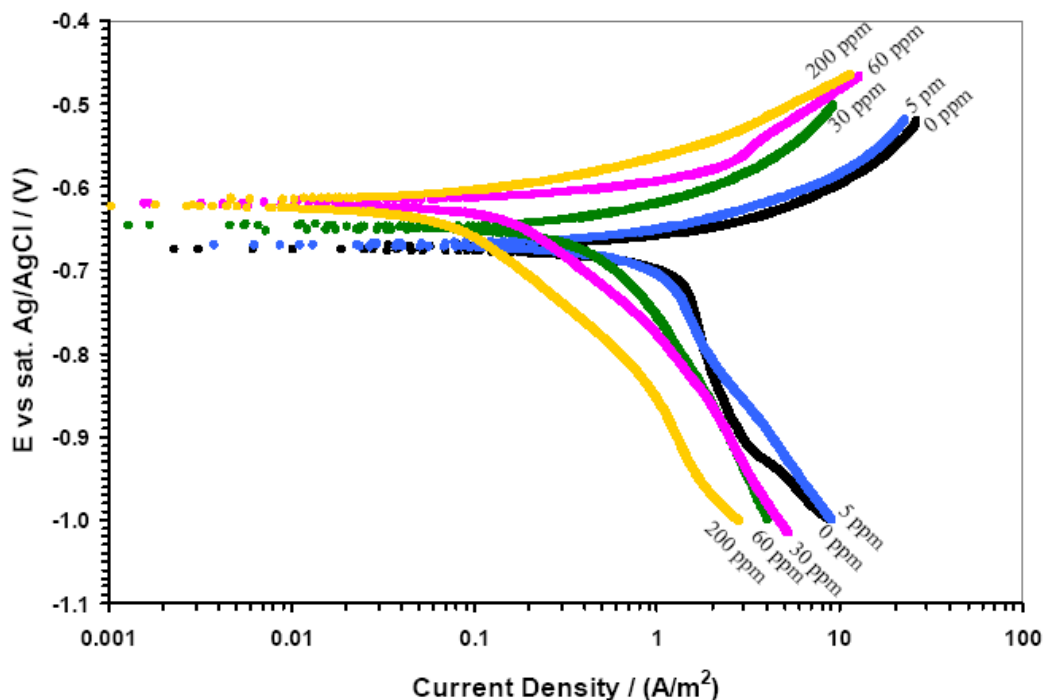


Figure 38 Comparison of potentiodynamic sweeps at different concentrations of “quat” in pure corrosion inhibition tests.

A plot of trajectory of the corrosion potential *versus* the corrosion current measured with the LPR technique at different test time points and the potentiodynamic sweeps for 200 ppm “quat” are shown in Figure 39. The initial point ( $t = 1.5\text{h}$ ) and the end point ( $t = 20\text{h}$ ) on the trajectory are the 200 ppm “quat” inhibitor addition time point (see the vertical dotted line on the Figure 35) and experiment finish time point, respectively. The potentiodynamic sweeps were conducted after the LPR measurement at time point  $t = 20\text{h}$ . The figure confirms that anodic reaction is mainly inhibited within the first 3 hours after inhibitor addition (from  $t = 1.5\text{h}$  to  $t = 4.5\text{h}$  on Figure 39), which leads to an increase in the corrosion potential and a drop in the corrosion current. This behavior could be explained by an adsorption of inhibitor molecules, which block the steel surface. A decrease of anodic reaction surface area then slows down the anodic reaction. After  $t =$

4.5h the corrosion potential becomes nearly constant, but the corrosion current keeps decreasing. It means that both the anodic and the cathodic reactions are gradually retarded due to a surface coverage effect and the transport of corrosive species is slowed down by a layer of adsorbed inhibitor molecules on the steel surface.

Similar plots of a comparison of potentiodynamic sweeps and a trajectory of the corrosion potential *versus* the corrosion current are shown in Figure 40 and Figure 41 for fatty amino inhibitor. It can be seen from Figure 40 that both the anodic and the cathodic reactions are retarded at 5 ppm addition of fatty amino. However, the cathodic reaction is not further inhibited from 5 to 200 ppm concentration, while the anodic reaction is slowed down further in that range. One can find from Figure 41 that the anodic reaction is rapidly inhibited within 30 minutes after the fatty amino addition, since a rapid increase in corrosion potential and a decrease in corrosion current are observed. After that, a gradual decrease in both corrosion potential and corrosion current are found in the remainder of the test duration, which means a gradual decrease in the cathodic reaction and at the same time the anodic reaction remains at the same inhibited reaction rate as it reached in the first 30 minutes.

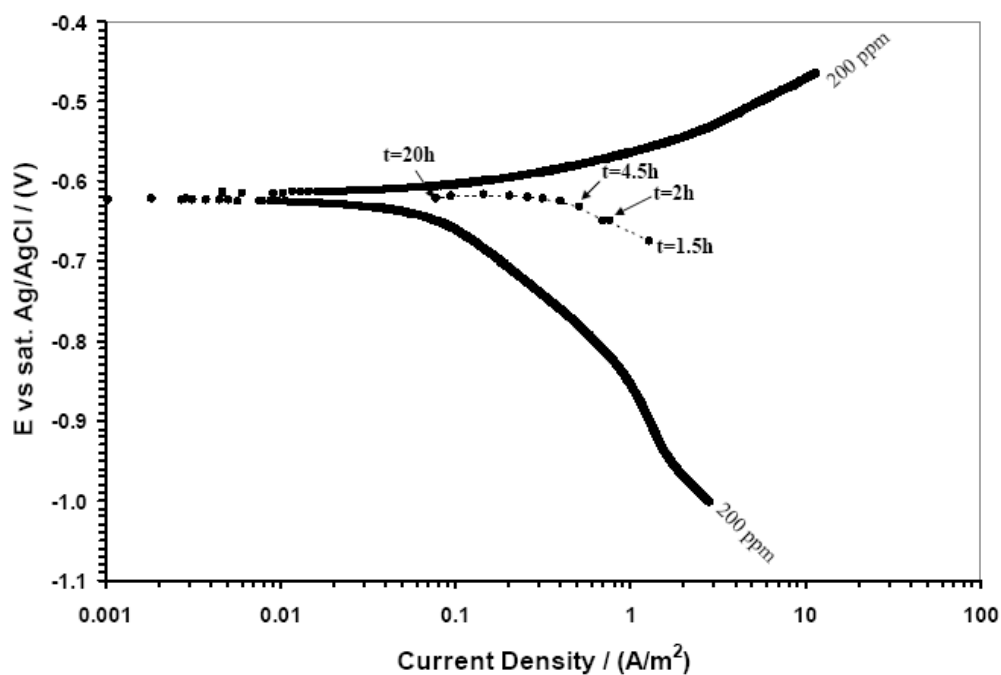


Figure 39 Corrosion potential *versus* corrosion current of corrosion points measured with the LPR at 200 ppm “quat” in pure corrosion inhibition tests.

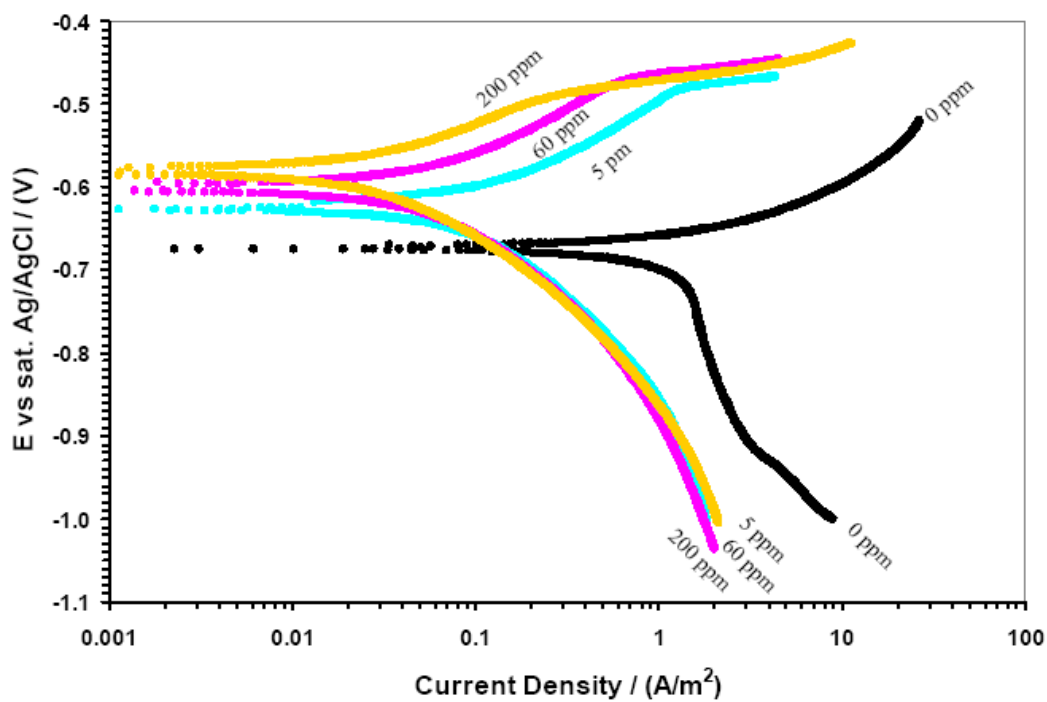


Figure 40 Comparison of potentiodynamic sweeps at different concentrations of fatty amino in pure corrosion inhibition tests.

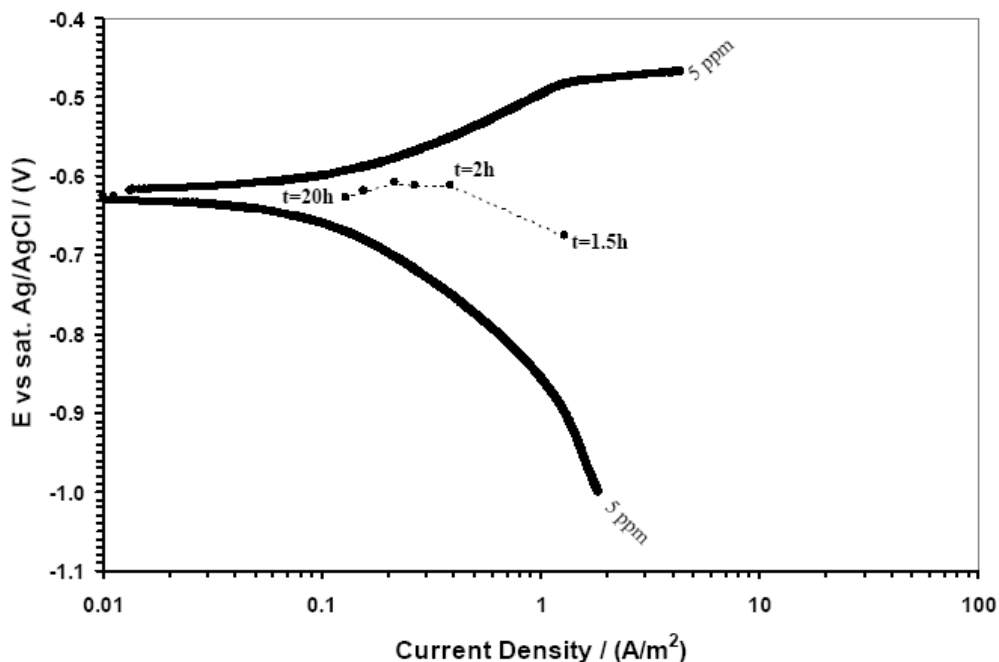


Figure 41 Corrosion potential versus corrosion current of corrosion points measured by LPR at 5 ppm fatty amino in pure corrosion inhibition tests.

### 5.2.2 Direct oil wet tests

Figure 42 and Figure 43 show the comparisons of corrosion rates in direct oil wet and pure corrosion inhibition tests (from Section 5.2.1) with 5 and 60 ppm “quat”, respectively. The vertical dotted lines on the figures indicate the time (1.5 hour after the beginning of each test) of inhibitor addition. The model oil is added to the top of brine phase immediately following the inhibitor injection into the brine phase. The vertical solid lines in the figures indicate the time where the working electrode was lifted up into the oil phase. For the 5 ppm “quat” test (Figure 42), one can see that after the first direct oil wet the corrosion rates decrease from 0.93 to 0.88 mm/yr and stabilize at this level. The corrosion rates gradually increases after the second direct oil wet until the end of test (30 hours duration). For 60 ppm “quat” (Figure 43), the corrosion rates measured in the

direct oil test show the same trend as in the pure corrosion inhibition test. No obvious improvement of inhibition efficiency is seen with direct exposure of the working electrode to the model oil phase at 5 and 60 ppm additions of “quat” inhibitor.

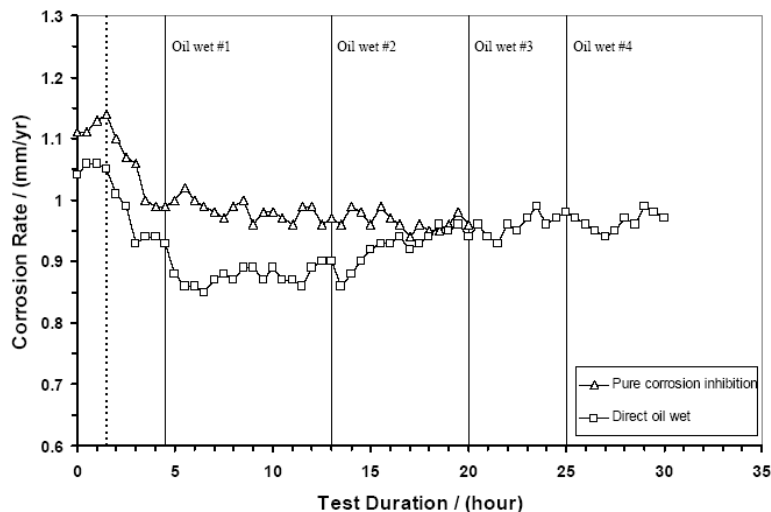


Figure 42 Comparison of corrosion rates in direct oil wet and pure corrosion inhibition tests for 5 ppm “quat” inhibitor. The vertical dotted line indicates inhibitor addition timeline and other vertical solid lines indicate oil wetting timelines.

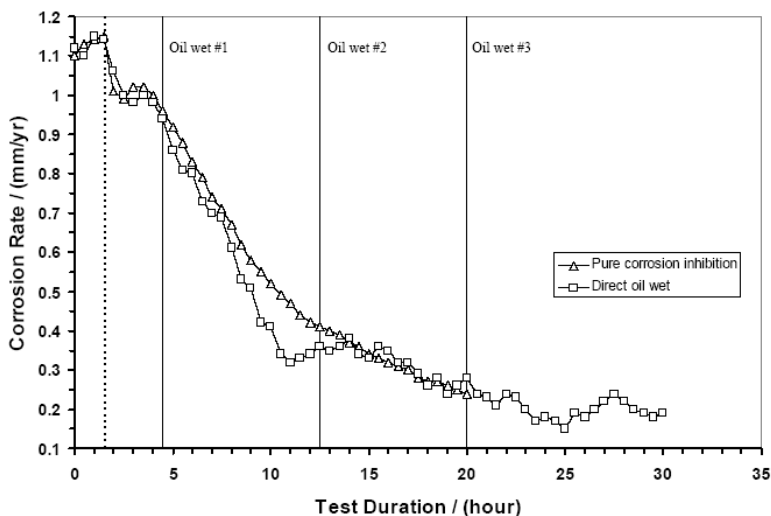


Figure 43 Comparison of corrosion rates in direct oil wet and pure corrosion inhibition tests for 60 ppm “quat” inhibitor. The vertical dotted line indicates inhibitor addition timeline and other vertical solid lines indicate oil wetting timelines.

The comparisons of corrosion rates in direct oil wet and pure corrosion inhibition tests with 1 and 5 ppm fatty amino are shown in Figure 44 and Figure 45, respectively. For 1 ppm fatty amino test, after the first point of direct oil wet at 6.4 hours the corrosion potential of working electrode greatly shifts to the positive direction. LPR measurement is unable to be conducted in the first 30 minutes following direct oil wet since the corrosion potential is very unstable. An obvious drop in the corrosion rate is observed after the corrosion potential becomes stable. The second and third direct oil wets only give a slight drop in the corrosion rate. Similar trends are found in 5 ppm fatty amino direct oil wet test (Figure 45). The inhibition efficiencies are enhanced from 36 to 90% for 1 ppm and from 90 to 99% for 5 ppm fatty amino additions. Two possible explanations can be deduced from these results. The fatty amino is an oil soluble/water dispersible inhibitor. The additional source of inhibitor molecules from the oil phase can give better surface coverage during the working electrode direct exposure to the oil phase and thus improve the inhibition performance in the brine phase. Another explanation is that the wettability of the steel surface changed from hydrophilic to hydrophobic after inhibitor molecules adsorbed at the steel surface, forming a thin oil film. The obvious enhanced corrosion inhibition is found after the first direct oil wetting. However, the improvement could not be enhanced with further periodic direct oil wetting.

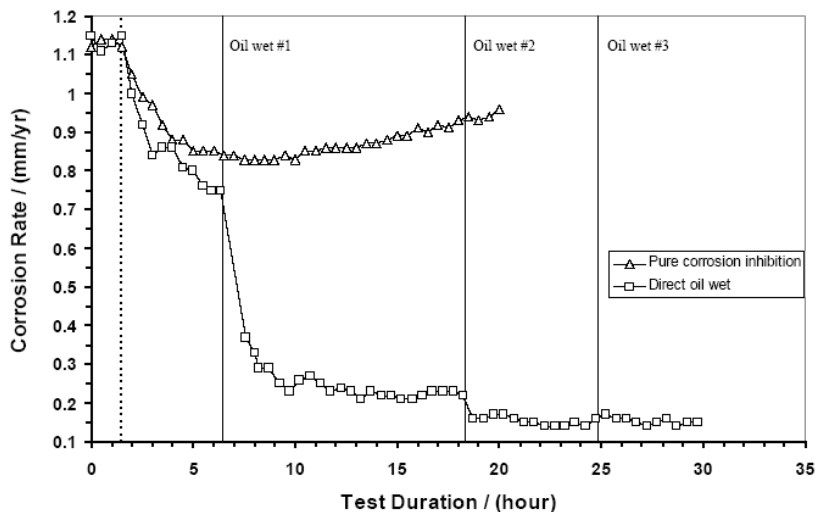


Figure 44 Comparison of corrosion rates in direct oil wet and pure corrosion inhibition tests for 1 ppm fatty amino inhibitor. The straight dotted line indicates inhibitor addition timeline and other straight solid lines indicate oil wetting timelines.

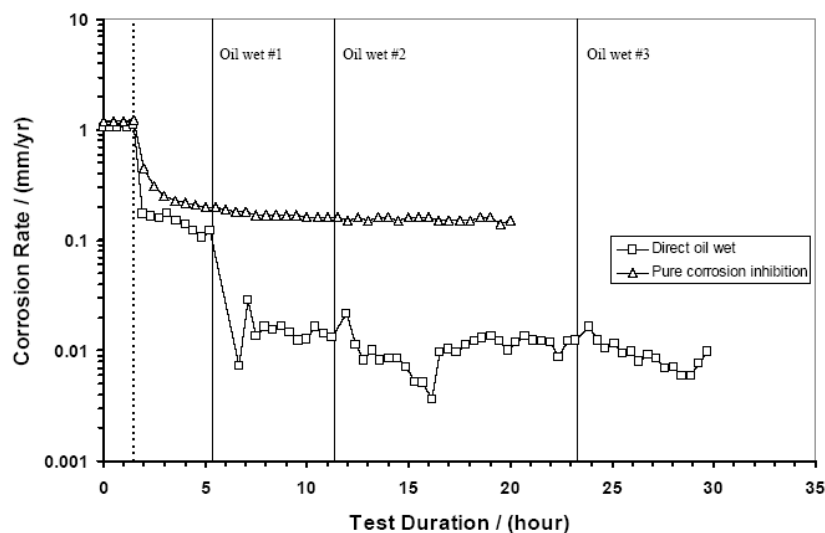


Figure 45 Comparison of corrosion rates in direct oil wet and pure corrosion inhibition tests for 5 ppm fatty amino inhibitor. The vertical dotted line indicates inhibitor addition timeline and other vertical solid lines indicate oil wetting timelines.

### 5.2.3 Partitioning tests

Figure 46 shows the comparison of corrosion rates in partitioning and pure corrosion inhibition test (from Section 5.2.1) for 5 ppm fatty amino. The vertical dotted

line on the figure indicate the time point of inhibitor injection. The vertical solid lines on the figure indicate the time points of the additions of the model oil. 5-mL model oil is added on the top of brine phase at 6 hours of test duration. It does not affect corrosion rate at all after 16.8 hours waiting time. Then 20-mL model oil is added into the cell at 22.8 hours. It is found that corrosion rate remains steady until the end of experiment. The final corrosion rate obtained from the partitioning test with 5 ppm fatty amino is identical to the result from the pure corrosion inhibition test at the same inhibitor concentration. Partitioning tests are also conducted with injection of 20 and 60 ppm fatty amino, “quat” and one commercial inhibitor package provide by one of the sponsors. There is no improvement of corrosion inhibition found during all those partitioning tests with different inhibitors and different concentrations.

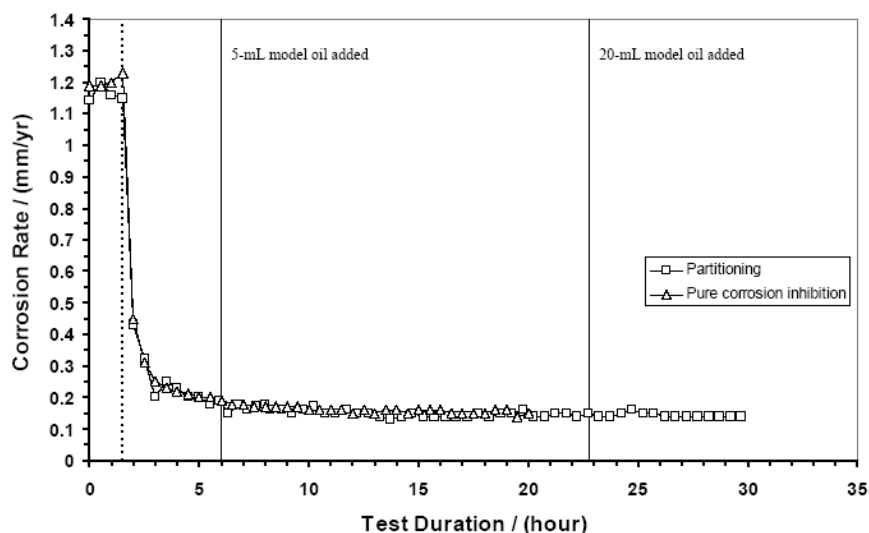


Figure 46 Comparison of corrosion rates in partitioning and pure corrosion inhibition tests for 5 ppm fatty amino inhibitor. The straight dotted line indicates inhibitor addition time and two straight solid lines represent the model oil addition timelines.

### 5.3 Summary

The CO<sub>2</sub> corrosion inhibition in an oil-water two-phase system is studied by using a glass cell, rotating cylinder electrode and electrochemical techniques. Fatty amino and “quat” inhibitors both show the same inhibition mechanism of first inhibiting the anodic reaction, and then slowing down the cathodic reaction. The inhibition performance of the fatty amino inhibitor is enhanced when the steel surface is direct wetted by oil phase at the first time, however no further improvement is found in periodical oil wetting. Direct oil wet has negligible effect on the “quat” inhibitor performance. There is no effect of the presence of oil on top of the brine found in the partitioning tests.

## CHAPTER 6: EXPERIMENTAL STUDY OF CORROSION INHIBITOR

### SURFACE ACTIVE PROPERTIES

#### 6.1 Experimental setup and procedure

##### 6.1.1 Equipment

Surface active properties of corrosion inhibitors are studied by measuring oil-water interfacial tension, contact angle of droplet on the steel surface and emulsion stability. A CSC-DuNouy tensiometer, which is shown in Figure 47, is used to measure the changes of oil-water interfacial tension due to the addition of an inhibitor. The tensiometer has a platinum wire ring, which is immersed in the water phase. The oil phase is slowly added on top of the water phase. The platinum ring is pulled up and when it suddenly breaks through the oil-water interface, the required force in units of dyne/cm (equal to milliNewtons per meter) can be read from the dial of the tensiometer.

The wettability of the steel surface is characterized by the contact angle of oil/water droplet on steel surface immersed in a continuous water/oil medium. The contact angle measurements are conducted with a goniometer. This was designed and built (Tang *et al.*, 2008) at the Institute for Corrosion and Multiphase Technology at Ohio University. Figure 48 shows a real view picture of the system including the goniometer, camera and light source used for the measurements. Both contact angle of oil droplet on steel surface in a continuous brine phase (oil-in-water) and contact angle of water droplet on steel surface in a continuous oil phase (water-in-oil) can be measured in the goniometer. A carbon steel coupon is placed on a Teflon<sup>TM</sup> sample holder. In the measurements, both images and videos analyzed by Rincon<sup>®</sup> software.

A series of oil-water emulsion tests are conducted in a 50-mL beaker. A magnetic stirrer bar is placed in the beaker to mix oil and water in the presence of different concentrations of corrosion inhibitor. The types of emulsion (either water-in-oil or oil-in-water) are determined measuring solution resistance with a digital voltage meter.



Figure 47 A real view picture of the CSC-DuNouy tensiometer used to measure oil-water interfacial tension (Courtesy of Francois Ayello).

#### 6.1.2 Experimental procedure

Prior to measuring the changes of oil-water interfacial tension, sample preparation is very important to allow for the inhibitor to partition between the oil and the water. The deionized water with 1 wt% NaCl is deoxygenated with purging CO<sub>2</sub> gas in a 500-mL breaker for 1 hour and is adjusted to pH 5.0 by adding NaHCO<sub>3</sub>. To control the water chemistry during inhibitor addition, a plastic glove bag with CO<sub>2</sub> gas purging is used. All

the interfacial tension experiment samples are prepared in the glove bag. Corrosion inhibitor is added to a test tube which contains 15-mL oil and 15-mL brine (deionized water with 1 wt% NaCl). The concentration of inhibitor is calculated based on the total volume of liquid. After inhibitor addition, the test tube is shaken for a few minutes and then set still for a period of 1 day for inhibitor partitioning. At the end of this partitioning period the oil and the water are transferred by syringes to the glass container (see Figure 47), which is used for tensiometer measurements.

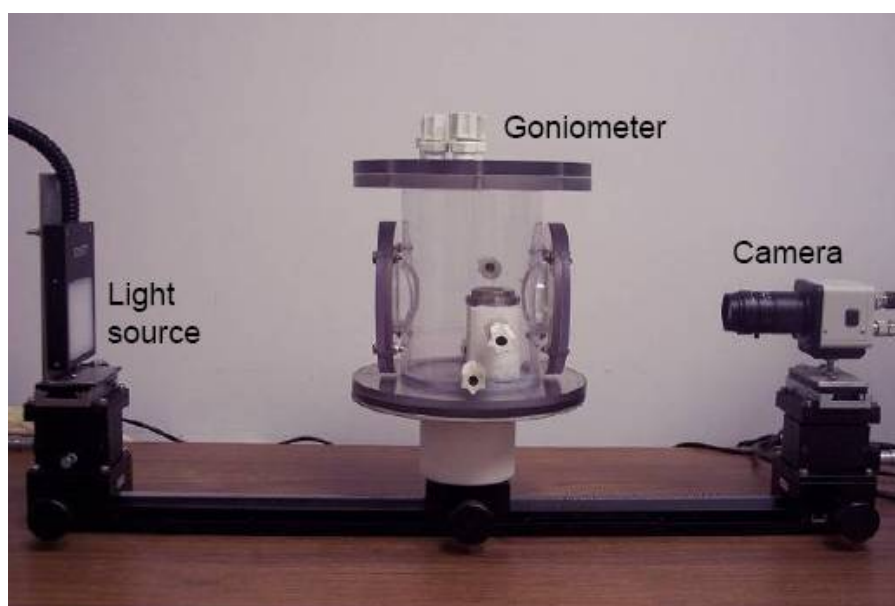


Figure 48 A real view of the system including goniometer, camera and light source used to measure contact angle of droplet on the steel surface (Courtesy of Xuanping Tang).

For the contact angle test, either oil or brine (deionized water with 1 wt% NaCl) is filled in the goniometer to 500-mL. A bubbler is inserted into the liquid to purge CO<sub>2</sub> gas for deoxygenation. The pH of the brine phase is adjusted to 5.0 with NaHCO<sub>3</sub>. A flat X65 carbon steel coupon is polished with 400- and 600-grit SiC paper, washed with

isopropanol and dried with an air blower. After the coupon is immersed into the solution, an oil droplet on bottom or a water droplet on top of the coupon surface is placed using a 10- $\mu$ L syringe. A baseline test (no inhibitor) is carried out first after which corrosion inhibitor is injected into the continuous phase and the concentration is increased stepwise.

Two emulsion experiment series are conducted at 50% and 20% water cut, respectively. A total volume of 40-mL oil-water mixture is filled in a clean and dry 50-mL beaker. The water chemistry of brine phase is well controlled, as in other tests. Different concentrations of corrosion inhibitors are added into the oil-water mixtures in separate tests. The beaker is sealed with parafilm. The rotation speed of the magnetic stirrer bar is controlled at 600 rpm and mixing is maintained for 2 minutes. After mixing, the total separation time is recorded.

After each oil-water interfacial tension, contact angle and emulsion test, the equipment including the glass containers, platinum ring, test tubes and beakers are carefully washed with tap water, deionized water and isopropanol to avoid inhibitor contamination in the following tests.

### 6.1.3 Test matrix

Table 21, Table 22 and Table 23 show the test matrix of oil-water interfacial tension, contact angle and emulsion stability measurements. The properties of the oil phase can be seen from Table 4. The formulations of two inhibitor packages can be found from Table 17 and Table 18. The chemical composition of X65 carbon steel is shown in Table 24.

Table 21 Test matrix of oil-water interfacial tension measurements.

<b>Brine solution</b>	Deionized water with 1 wt% NaCl
<b>pH of brine solution</b>	5.0
<b>Oil phase</b>	Model oil (LVT 200)
<b>Total pressure / (bar)</b>	1.013
<b>Temperature / (°C)</b>	25
<b>Water cut / (%)</b>	50
<b>Partitioning time / (hour)</b>	24
<b>Inhibitor type</b>	Quaternary ammonium chloride and fatty amino
<b>Inhibitor concentration / (ppm)</b>	0 – 200

Table 22 Test matrix of contact angle measurements.

<b>Brine solution</b>	Deionized water with 1 wt% NaCl
<b>pH of brine solution</b>	5.0
<b>Oil phase</b>	Model oil (LVT 200)
<b>Specimen material</b>	X65 carbon steel
<b>Total pressure / (bar)</b>	1.013
<b>Partial pressure of CO<sub>2</sub> / (bar)</b>	0.96
<b>Temperature / (°C)</b>	25
<b>Inhibitor type</b>	Quaternary ammonium chloride and fatty amino
<b>Inhibitor concentration / (ppm)</b>	0 - 200

Table 23 Test matrix of emulsion stability measurements.

<b>Brine solution</b>	Deionized water with 1 wt% NaCl
<b>pH of brine solution</b>	5.0
<b>Oil phase</b>	Model oil (LVT 200)
<b>Total pressure / (bar)</b>	1.013
<b>Temperature / (°C)</b>	25
<b>Water cut / (%)</b>	20 and 50
<b>Rotation speed of stirrer / (rpm)</b>	600
<b>Mixing time / (minute)</b>	2
<b>Inhibitor type</b>	Quaternary ammonium chloride and fatty amino
<b>Inhibitor concentration / (ppm)</b>	0 - 200

Table 24 Chemical composition of X65 carbon steel.

<b>C</b>	<b>Si</b>	<b>P</b>	<b>S</b>	<b>Mn</b>	<b>Al</b>	<b>Cr</b>	<b>Cu</b>	<b>Ni</b>	<b>Fe</b>
0.05	0.31	0.01	0.002	1.32	0.03	0.04	0.02	0.04	Balance

## 6.2 Results and discussion

The model oil-brine interfacial tension measured from the baseline test (no inhibitor addition) is 40.0 dyne/cm. Figure 49 shows the changes of oil-water interfacial tension due to addition of fatty amino and “quat” inhibitors, respectively. It can be seen for both inhibitors that initially a rapid drop in oil-water interfacial tension occurs at low additive concentration. When the oil-water interfacial tension is stable, the critical micelle concentration (CMC) has been reached since the oil-water interface has become saturated with inhibitor molecules. It can be seen that the CMC point is 3 ppm for fatty amino and 5 ppm for “quat”, respectively. As discussed in Chapter 2, a reduction of oil-water interfacial tension makes the water entrainment easier. However, it is very important to measure oil-water interfacial tension with inhibitor addition using the proper sample preparation as described above.

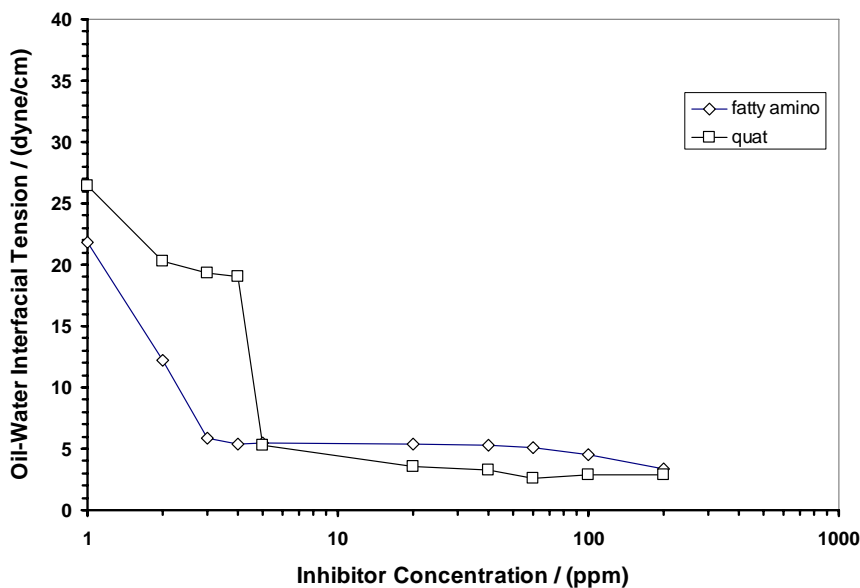


Figure 49 Model oil-brine interfacial tension measured at different concentrations of fatty amino and “quat” corrosion inhibitors.

The contact angle measurements are carried out in two series, oil-in-water and water-in-oil. The reported values always refer to the angle between the droplet and the steel surface in respect to the brine phase. An angle of  $90^\circ$  or less means that the surface is hydrophilic. An angle of greater than  $90^\circ$  indicates hydrophobic surface. The images of oil-in-water contact angle measurements for fatty amino and “quat” are shown in Figure 50 and Figure 51. In each image, the contact angle of an oil droplet pushed up against the bottom surface (the top black area on each image) of carbon steel specimen which is immersed in the continuous brine phase is indicated by two straight lines. The measured value of the angle is shown on the picture with the inhibitor concentration. A  $22^\circ$  contact angle of oil-in-water is obtained for baseline test (no inhibitor). It can be seen that the contact angle of the model oil droplet becomes bigger with increasing inhibitor concentration for both fatty amino and “quat”. A plot of the oil-in-water contact angles versus inhibitor concentration for “quat” and fatty amino tests is shown in Figure 52.

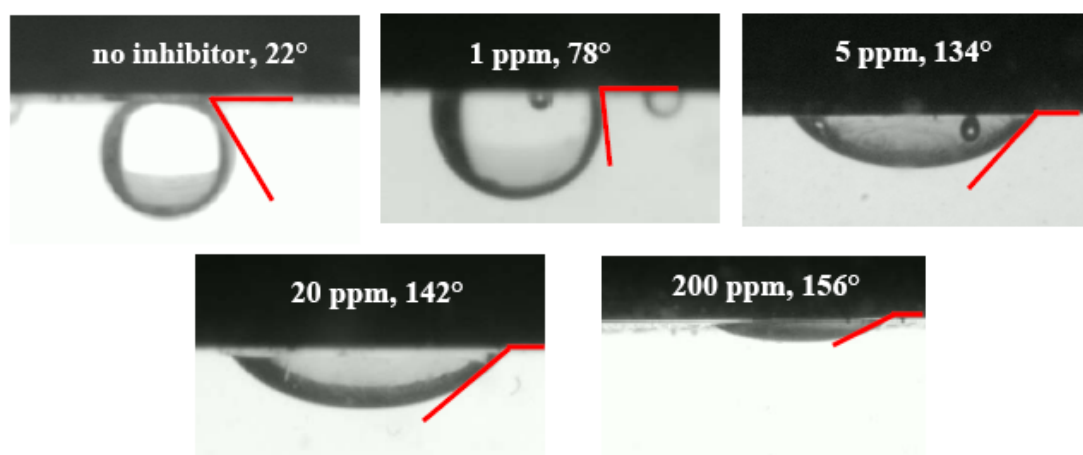


Figure 50 Images of oil droplet on steel surface in contact angle measurements with 0, 1, 5, 20 and 200 ppm fatty amino inhibitor added in the continuous water phase. In the pictures, inhibitor concentrations and measured contact angle values are written on the black areas, which are the bottom portions of carbon steel specimens.

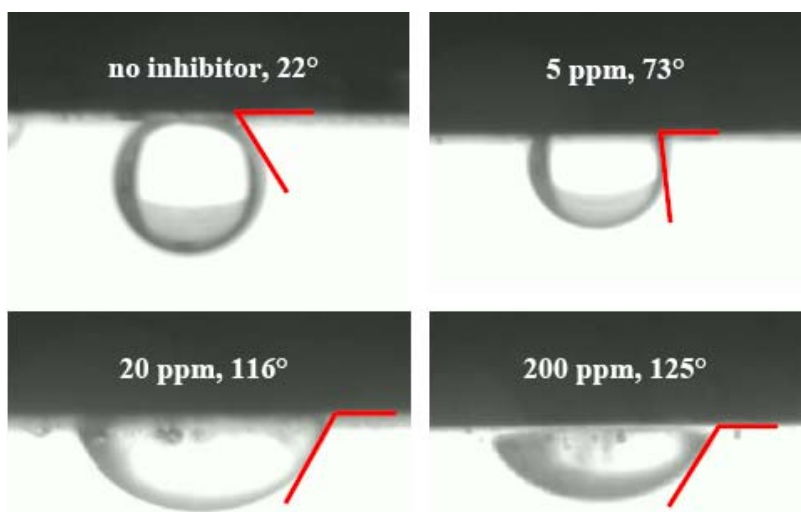


Figure 51 Images of oil droplet on steel surface in contact angle measurements with 0, 1, 5, 20 and 200 ppm “quat” inhibitor added in the continuous water phase. In the pictures, inhibitor concentrations and measured contact angle values are written on the black areas, which are the bottom portions of carbon steel specimens.

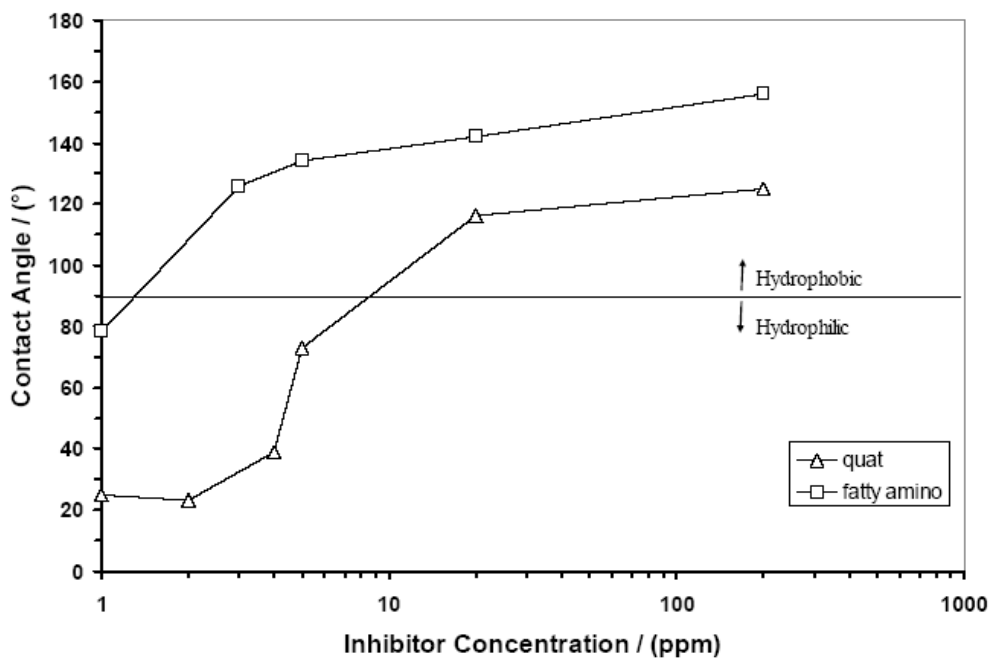


Figure 52 Contact angles of oil-in-water versus inhibitor concentration for “quat” and fatty amino.

The images of water-in-oil contact angle measurements for fatty amino are shown in Figure 53. Similar to the above, each angle of the brine droplet on the top surface (the bottom black area on each image) of the carbon steel coupon which is immersed in the continuous oil phase is indicated by two straight lines. The measured angle values with inhibitor concentration are written on each image. It is clear to see that the contact angle of water-in-oil is increased with inhibitor addition. No water-in-oil contact angle measurement was conducted for “quat” inhibitor because it is water soluble only.

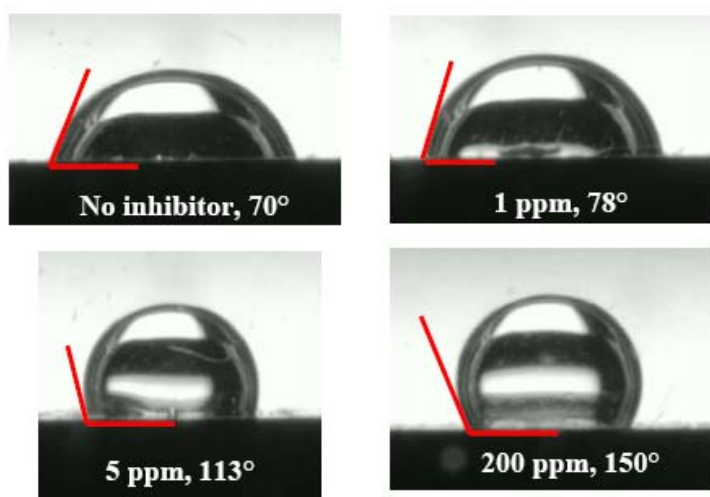


Figure 53 Images of water droplet on steel surface in contact angle measurements with 0, 1, 5 and 200 ppm fatty amino inhibitor added in the continuous oil phase. In the pictures, inhibitor concentrations and measured contact angle values are written on the black areas, which are the bottom portions of carbon steel specimens.

The oil-in-water contact angle measurements simulate the case of pipe inner surface initially wetted by water phase. It is found that the carbon steel surface retains hydrophilic properties when an oil droplet approaches to the steel surface. Therefore it is very difficult for the oil droplet to replace the water and spread out on the surface. However, with the addition of corrosion inhibitor, “quat” or fatty amino, into the water

phase, the oil droplet becomes much easier to be “adsorbed” on the steel surface and replace the water phase. This indicates that the wettability of steel surface becomes hydrophobic with the addition of an inhibitor. The water-in-oil contact angle tests simulate the case of pipe inner surface initially wetted by hydrocarbon. Without inhibitor addition, the water droplet can replace oil phase from the steel surface to give water wetting. This result further confirms the wettability of the clean carbon steel surface to be hydrophilic. With the addition of fatty amino (oil soluble) inhibitor to the oil phase, the water droplet is not able to spread out on the initial oil wetted surface to replace the oil. The experimental findings can be explained by the hydrophilic heads on the inhibitor molecules adsorbing on the steel surface, orientating their hydrophobic tails towards solution. Those hydrophobic tails repulse water and attract oil, which leads to oil wetting. The switch of wettability of the carbon steel surface from hydrophilic (water wetting) to hydrophobic (oil wetting) due to corrosion inhibitor surface active properties could reduce the possibility of internal pipeline corrosion.

The formation and stability of oil-water emulsion in the presence of “quat” or fatty amino is studied by examination of the separation time after vigorous mixing. In the baseline tests (no inhibitor addition), the model oil and brine separates quickly in 3 and 6 seconds for 20% and 50% water cuts, respectively. No oil-water emulsion is observed in the baseline tests. The solution resistance measured with a voltage meter indicates that dispersion of water in the continuous oil phase forms at 20% water cut and dispersion of oil in the continuous water phase occurs at 50% water cut. With additions of the “quat” and fatty amino inhibitors, the time required for full separation begins to increase. Figure

54 and Figure 55 show the recorded time for the model oil-brine complete separation with “quat” and fatty amino additions in the emulsion stability tests at 20% and 50% water cuts. At 20% water cut, although separation time is longer when inhibitor is added than that for the baseline test (no inhibitor), only dispersion of water droplets in the continuous oil phase is found. No stable oil-water emulsion is observed even up to 200 ppm inhibitor concentration. It also can be seen from the figure that the separation time is almost the same for two inhibitors in the tested concentration range. At 50% water cut and low inhibitor concentration (5 to 20 ppm), the separation time is longer than that obtained at 20% water cut with the same inhibitor concentration. By increasing the concentration from 20 to 200 ppm, a stable oil-in-water emulsion is formed, which means fine oil droplets dispersed in the continuous brine phase.

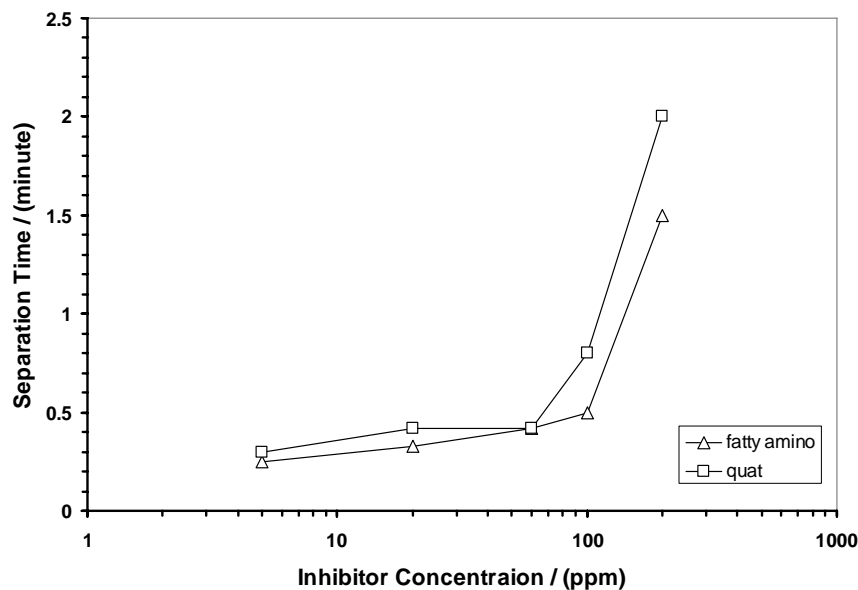


Figure 54 Recorded time for model oil-brine complete separation in emulsion stability tests with “quat” and fatty amino addition at 20% water cut.

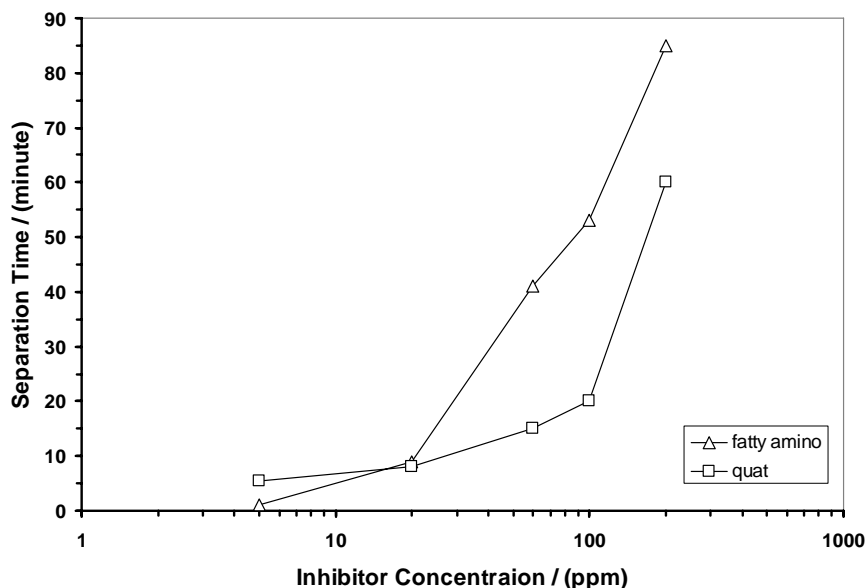


Figure 55 Recorded time for model oil-brine complete separation in emulsion stability tests with “quat” and fatty amino addition at 50% water cut.

### 6.3 Summary

The surface active properties of corrosion inhibitors are investigated by measuring changes of oil-water interfacial tensions, contact angles and emulsion stability. It is found that a dramatic drop in oil-water interfacial tension occurs with inhibitor addition prior to the critical micelle concentration (CMC), which was also found by Moon and Horsup (2002). The reduction of oil-water interfacial tension enhances the possibility of achieving oil wetting regime in oil-water two-phase flow. Addition of corrosion inhibitor can change the wettability of the steel surface from hydrophilic to hydrophobic, which was also found by McMahon (1991). This change of the wettability can reduce the possibility of CO<sub>2</sub> corrosion due to preferential oil wetting. The preliminary emulsion stability tests show that stable oil-water emulsion can form at 50% water cut and above 20 ppm “quat” or fatty amino concentration.

## **CHAPTER 7: EXPERIMENTAL STUDY OF OIL-WATER TWO-PHASE FLOW IN DOUGHNUT CELL**

### **7.1 Experimental setup and procedure**

#### 7.1.1 Development of the doughnut cell

A small scale apparatus is preferable for studying phase wetting and CO<sub>2</sub> corrosion in oil-water two-phase flow. Due to the small size, it requires minimal amounts of oil for testing and less time and manpower for operation. One of the challenging problems of developing the small scale apparatus is that the phenomena of water entrainment, coalescence, breakout and hydrodynamic interactions between oil, water and the steel surface need to be simulated to correspond to the conditions found in the pipe flow. Otherwise, the results from small scale apparatus may not be transferable to the large scale oilfield pipe flow.

Recently a prototype small scale apparatus, called the doughnut cell, has been developed in this work to simulate phase wetting in oil-water two-phase flow. Figure 56 shows the whole doughnut cell test system including the cell and instrumentation used for tests (pitot tube, differential pressure transducer, transducer digital reader and data acquisition boards for wall conductance probes). The doughnut cell is mounted on a heavy duty steel mobile cart.

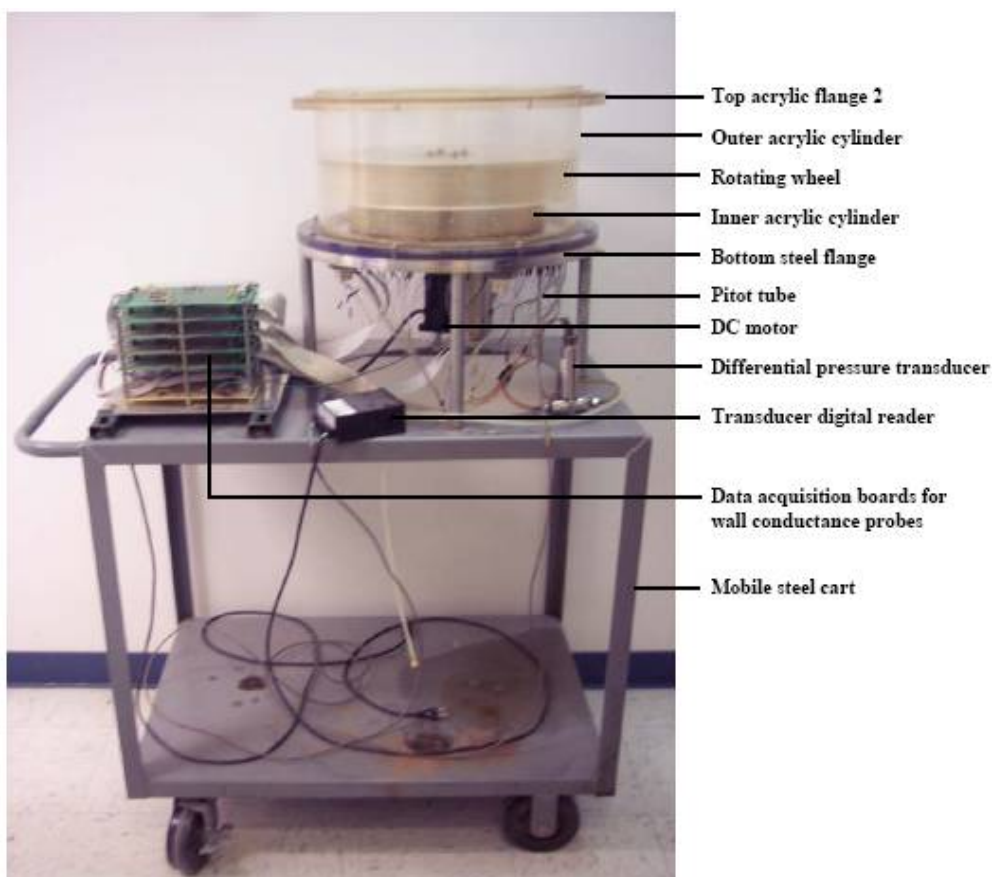


Figure 56 The whole doughnut cell test system with main components named.

Figure 57 shows a schematic cut view of the doughnut cell. Oil and water are placed in an annular flow channel between two acrylic cylinders (number 3 and 6 on Figure 57), which are held by a bottom flange (number 9) made of stainless steel 316 type. The top surface of this steel flange represents the bottom portion of the pipe inner wall in the phase wetting study. The other three acrylic flanges (number 1, 2 and 7) are used to seal and hold the cell. A rotating wheel (number 4) is set on top of the oil phase. Its rotational motion brings the oil and water phases into annular motion by shear stress. In the design assumption, the water phase at the bottom will be entrained in the flowing oil phase as increasing circumferential velocity of the oil phase. The reverse will occur

when the rotational velocity of the rotating wheel is reduced. The rotating wheel is connected to a DC motor (number 11) through a shaft coupling (number 5). A motor rotational speed controller is used to adjust circumferential velocity of the rotating wheel. The DC motor is attached to a key plate (number 12) and a motor holder (number 13), which is mounted at the bottom side of the stainless steel flange. The key plate and the motor holder allow the position of the motor to be adjusted (3D schematic is shown in Figure 58). The height of the rotating wheel is then changed with adjusting the motor position.

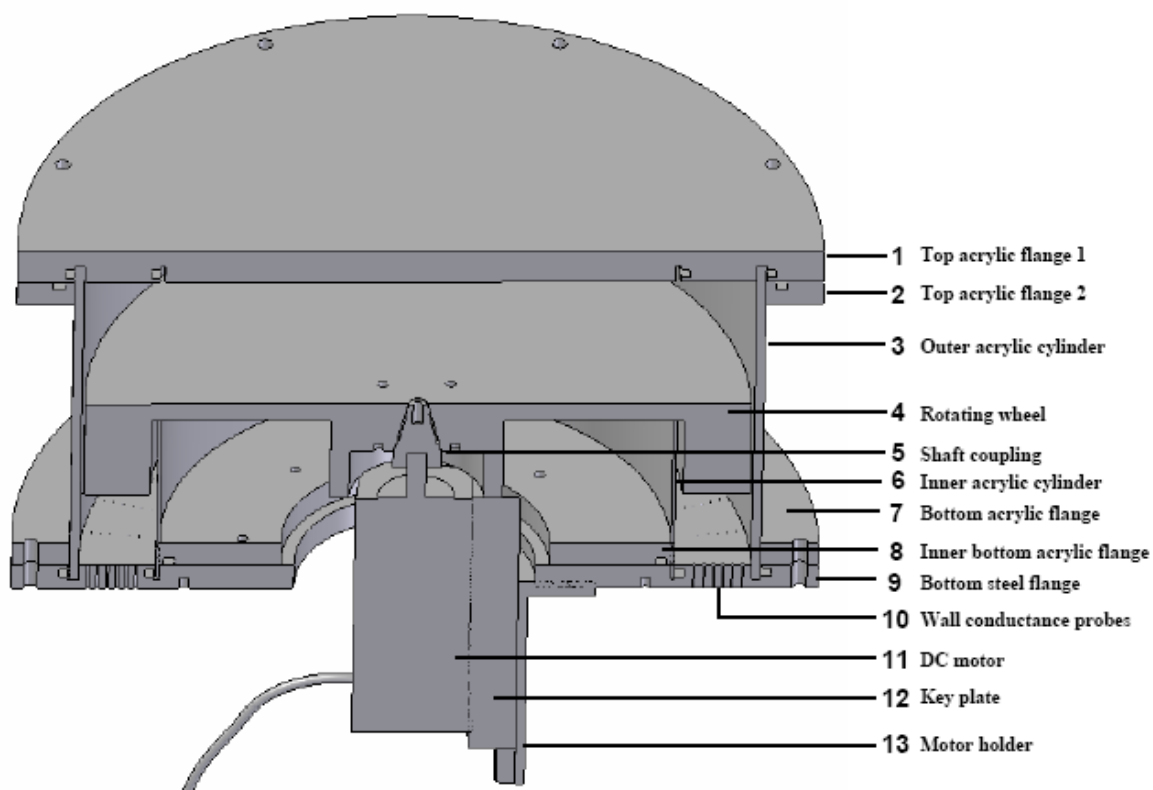


Figure 57 Cut view of the doughnut cell with main components numbered and named.

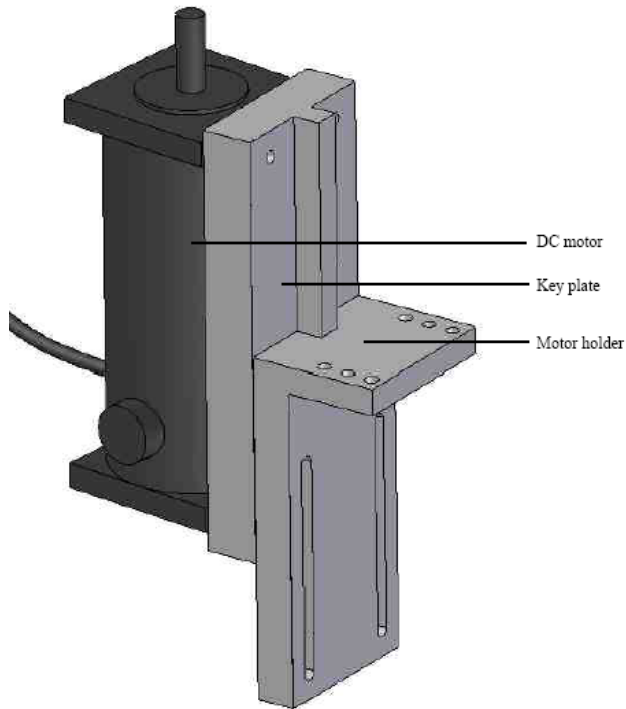


Figure 58 3D schematic of the DC motor mounted on the key plate and motor holder.

Computational Fluid Dynamics (CFD) modeling by using a commercial CFD software package, Fluent, is used for dimension optimization of the cell. A secondary flow is predicted to form in the flow channel because of rectangular shape of the cross section of the flow channel. The secondary flow, which in this case is the motion of fluids in the plane perpendicular to the primary circular flow, can affect water entrainment and breakout. A main effort with the help from CFD simulations is made to minimize the intensity of secondary flow in the flow channel by modifying the dimensions of the cell. It should be noted that the dimensions of the cell are not only determined by simulations, but are also affected by material availability in the market. The outer acrylic cylinder has 18-inch OD and 17.5-inch ID (0.25-inch wall thickness) and the inner acrylic cylinder has 13.7-inch OD and 13.5-inch ID (0.1-inch wall thickness). The actual width of the

circular flow channel is 1.81 inch due to machine allowance on the grooves in the steel flange for holding these two cylinders.

The instrumentation used for phase wetting study includes flow pattern visualization, wall conductance probes and corrosion rate monitoring. Acrylic cylinders are chosen for flow pattern visualization. A schematic top view of the stainless steel flange is shown in Figure 59. Wall conductance probes which have been successfully applied to determine phase wetting regime in pipe flows are flush mounted on the flange. Twenty eight rows with five probes in a row which gives a total of 140 probes are evenly distributed in four segments. ER probe, LPR probe and weight loss coupon can be flush mounted through the access ports for CO<sub>2</sub> corrosion rate monitoring. A pitot tube is inserted into the cell through a tee valve on a draining port for measuring *in situ* circumferential velocity of the oil phase. The pitot tube is connected to a differential pressure transducer and a digital transducer reader. The measured differential pressure,  $\Delta p$  (psi), can be converted to fluid velocity ( $u$ , m/s) according to Bernoulli's Equation (7-1), in which 6894.76 is a unit conversion factor for pressure from psi to Pa. Since turbulent flow is found in most tests, a time-averaged measurement value is taken as the *in situ* oil velocity. The oil velocity fluctuations are within  $\pm 2\%$  for all the doughnut cell tests.

$$u = \sqrt{\frac{2 \cdot \Delta p \cdot 6894.76}{\rho_{fluid}}} \quad (7-1)$$

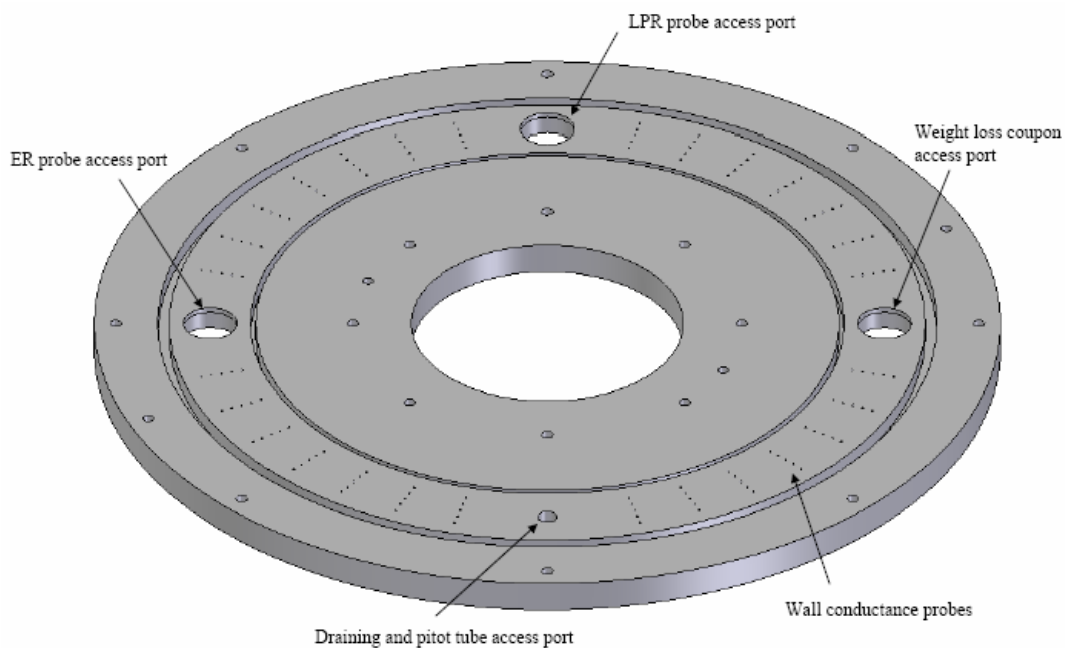


Figure 59 A schematic top view of the stainless steel 316 flange.

### 7.1.2 Experimental procedure

The distance between the top surface of the stainless steel flange and the bottom surface of the rotating wheel is set as 2.75 inch for all the tests in this study. With this constant setup the required total liquid phase volume is kept at 4.2 liters. The volumes of water and oil phases are calculated based on the water cut. Water is first poured into the cell from the top and then oil added. The measurement point on the pitot tube is set at the middle plane of the oil phase to record the *in situ* oil phase circumferential velocity. The test starts at the low motor rotational speed which gives low oil velocity. Increasing motor rotational speed step by step allows water to be entrained in the flowing oil phase until full oil wetting is achieved. A reverse measurement from oil wetting (high oil velocity) to water wetting (low oil velocity) is conducted to check the accuracy of phase wetting regimes. After draining the liquid, the cell is opened for cleaning with tap water,

deionized water and isopropanol. If chemicals are applied in the cell, such as corrosion inhibitors, the oil used in the test should be collected and treated as used oil to avoid experimental contamination.

### 7.1.3 Test matrix

Table 25 shows the test matrix for oil-water two-phase flow tests in the doughnut cell. The model oil and three different crude oils (C1, C2 and C3) are tested in the multiphase flow loop. This allows comparison of the results from small scale and large scale, two test systems. Two other crude oils (C6 and C7) are also tested in the doughnut cell. Their physical properties are described in Table 4.

Table 25 Test matrix of the doughnut cell tests.

<b>Oil phase</b>	Model oil (LVT 200) and Crude oils (C1, C2, C3, C6, C7)
<b>Water phase</b>	De-ionized water with 1 wt% NaCl (dyed with red food color)
<b>Total liquid volume</b>	4.2 liters
<b>Water cut</b>	0 – 20%
<b>Width of flow channel</b>	1.8125 inch
<b>Height of flow channel</b>	2.75 inch
<b>System temperature</b>	Room temperature (25°C)
<b>System pressure</b>	Atmospheric pressure (1.013 bar)

## 7.2 Results and discussion

Figure 60 shows the phase wetting map of model oil-brine in doughnut cell experiments. The three phase wetting regimes are the same as those found in the flow loop tests: oil wetting, intermittent wetting and water wetting as identified by wall conductance probes. Between 0.5 to 1 m/s oil velocity, water wetting dominates at water cut even as low as 4%. It can be seen that in that same range of oil velocity even 0.5%

water still produces intermittent wetting. Increasing the oil velocity from 1 to 1.5 m/s, the region of intermittent wetting on the map becomes smaller leading to oil wetting prevailing in that range of oil velocity. When the oil phase velocity is increased above 1.5 m/s, all the water is fully entrained to produce water-in-oil dispersed flow. It should be noted that the oil phase velocity has a measurement error of  $\pm 2\%$  on each test point for the phase wetting maps obtained from the doughnut cell tests.

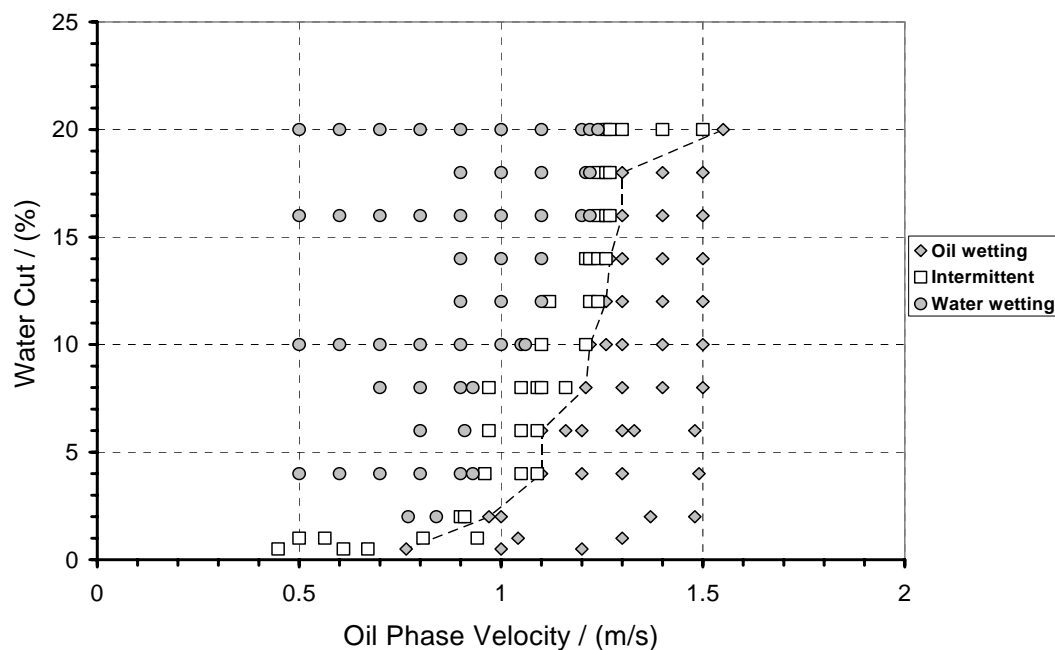


Figure 60 Phase wetting map of model oil-brine in doughnut cell experiments. The dotted line shows a transition line from intermittent to oil wetting.

The phase wetting map of C1 crude oil-brine from the doughnut cell is shown in Figure 61. At low water cut, 0.5 to 2%, there is no stable water wetting found in the tests. Water wetting occurs at water cut above 3% and oil velocity below 0.9 m/s. When the oil phase velocity is over 1 m/s, oil wetting dominates at all tested water cuts. Figure 62 and

Figure 63 show the phase wetting maps of C2 and C3 crude oil-brine from the doughnut cell, respectively. Water wetting only occurs when the oil phase velocity is below 0.6 m/s and oil wetting prevails at oil velocity of 0.7 m/s or higher.

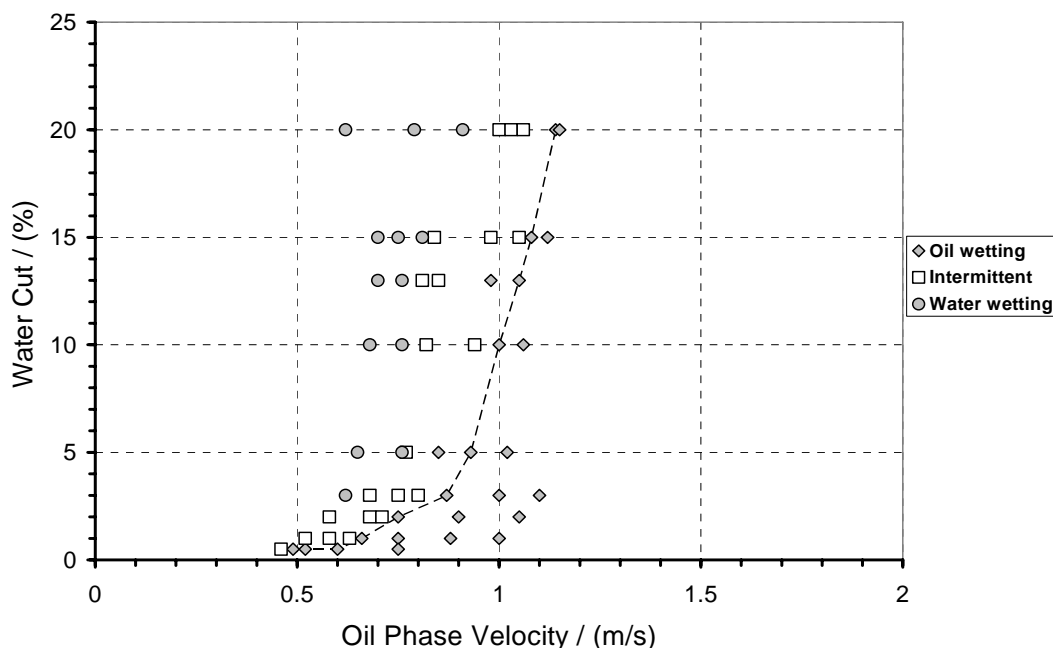


Figure 61 Phase wetting map of C1 crude oil-brine in doughnut cell experiments. The dotted line shows a transition from intermittent to oil wetting.

The phase wetting maps of C6 and C7 crude oil-brine in doughnut cell experiments are shown in Figure 64 and Figure 65, respectively. The distributions of three phase wetting regimes on the two maps are very similar. Water wetting occurs at oil phase velocity below 0.5 m/s and water cut of 10% or higher. Between 0.2 to 0.5 m/s oil phase velocity and 0.5 to 10% water cut intermittent wetting prevails. When the oil phase velocity is higher than 0.5 m/s, oil wetting takes place.

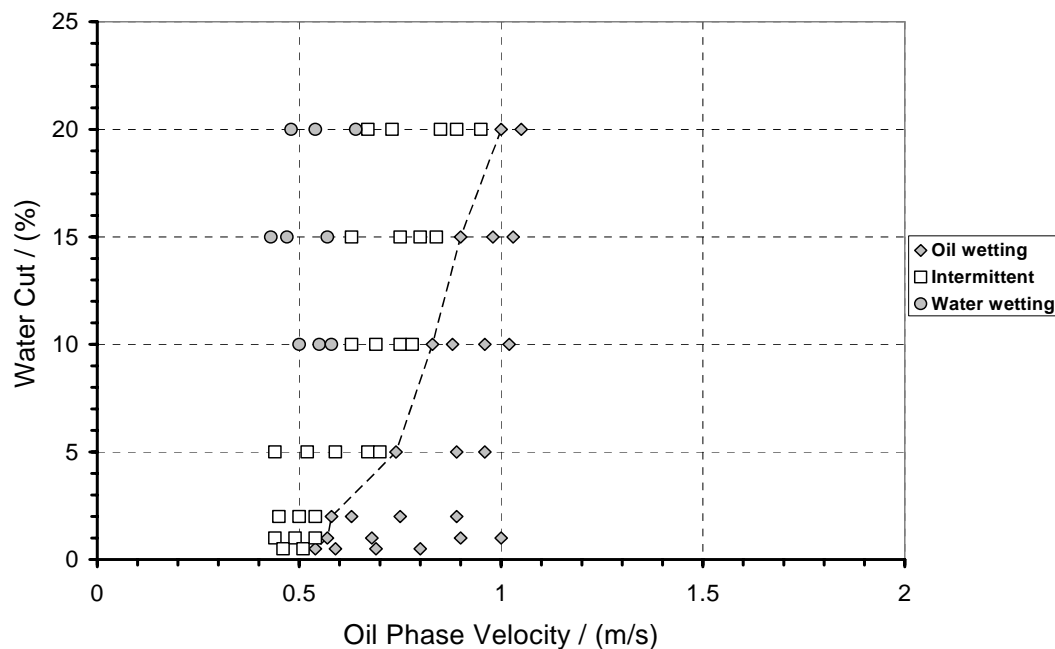


Figure 62 Phase wetting map of C2 crude oil-brine in doughnut cell experiments. The dotted line shows a transition from intermittent to oil wetting.

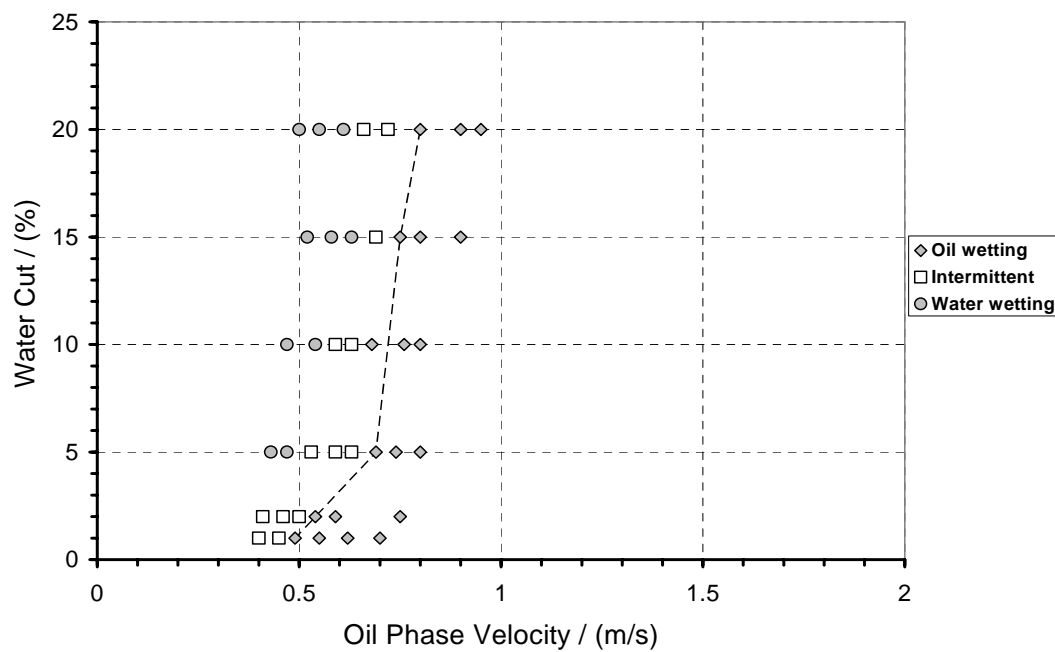


Figure 63 Phase wetting map of C3 crude oil-brine in doughnut cell experiments. The dotted line shows a transition from intermittent to oil wetting.

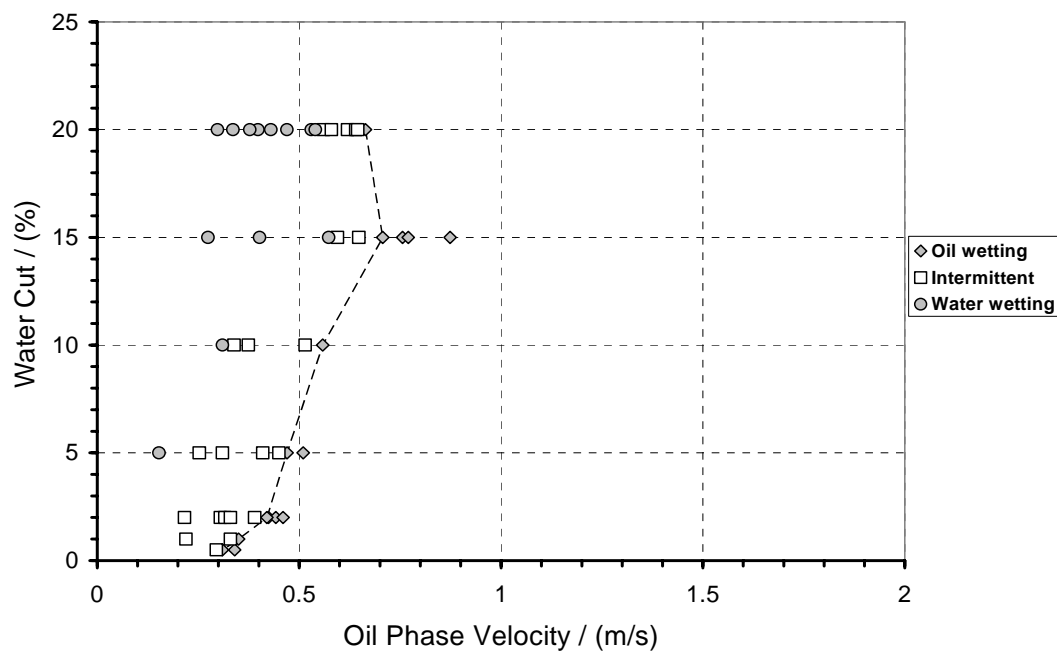


Figure 64 Phase wetting map of C6 crude oil-brine in doughnut cell experiments. The dotted line shows a transition from intermittent to oil wetting.

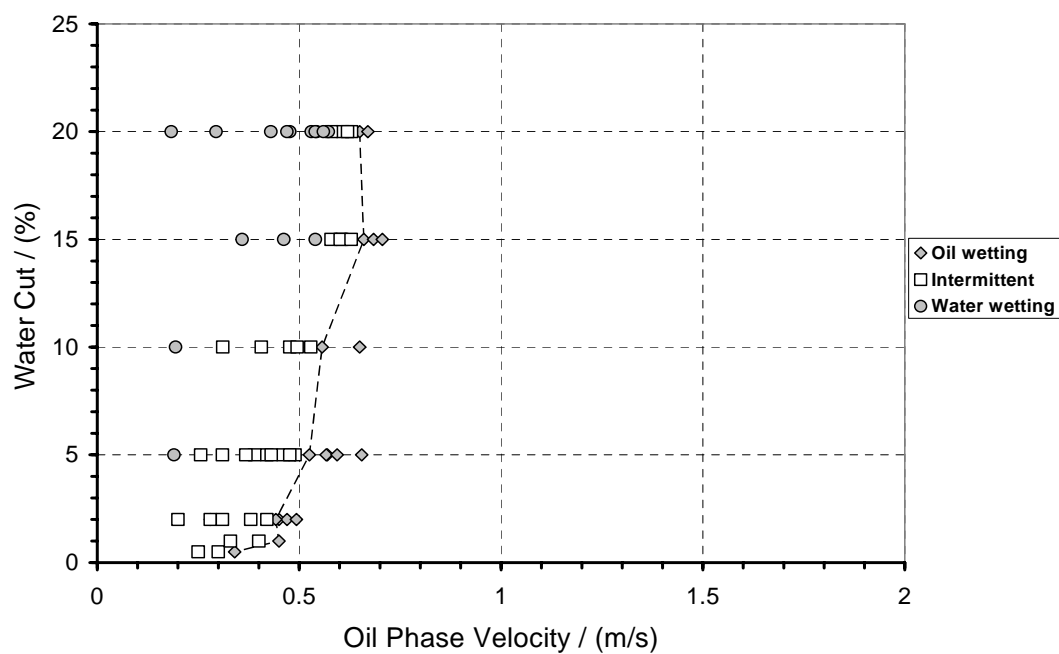


Figure 65 Phase wetting map of C7 crude oil-brine in doughnut cell experiments. The dotted line shows a transition from intermittent to oil wetting.

The transition lines from intermittent wetting to oil wetting are determined in the same conservative way as that described in the flow loop tests. A comparison of transition lines for model oil and different crude oils in the doughnut cell experiments is shown in Figure 66. The difference in the transition lines is explained by the physical properties (Table 4) of the tested crude oils. Oil-water interfacial tension plays an important role in phase wetting transition from intermittent wetting to oil wetting. Since all the tested crude oils have lower interfacial tension than the model oil, it is expected to find lower critical entrainment oil phase velocity for crude oils. From the comparison of experimental results, it is confirmed that easier water entrainment is achieved for the crude oils than the model oil. Comparing transitions lines of C1, C2 and C3 crude oils, higher viscosity and density typical for heavy crude oil helps to reduce the minimum oil phase velocity for full water entrainment. C6 crude oil is heavier (higher viscosity and density) and also has lower oil-water interfacial tension than C7 crude oil, which is beneficial for water entrainment towards lower oil phase velocity. It is expected that the transition line of C6 crude oil shift to left side of the transition line of C7 crude oil on the phase wetting map. However, it is interesting to see that no obvious difference can be found between those two transition lines of C6 and C7 crude oils. Comparing the physical properties of C3 and C6 crude oils, it is noticed that the densities, viscosities and oil-water interfacial tensions are very close between those two oils. However, C6 crude oil can entrain more water at a given oil phase velocity than C3 crude oil, such as at oil phase velocity of 0.5 m/s, up to 6.5% water cut can be entrained for C6 crude oil, but only 1% water cut for C3 crude oil. At oil phase velocity of 0.6 m/s, the maximum water

cut of 12% for full water entrainment is achieved for C6 crude oil, but only 3% water cut for C3 crude oil. One of the possible explanations is that the crude oil chemistry parameter, which is not included in this research may play an important role in phase wetting transitions.

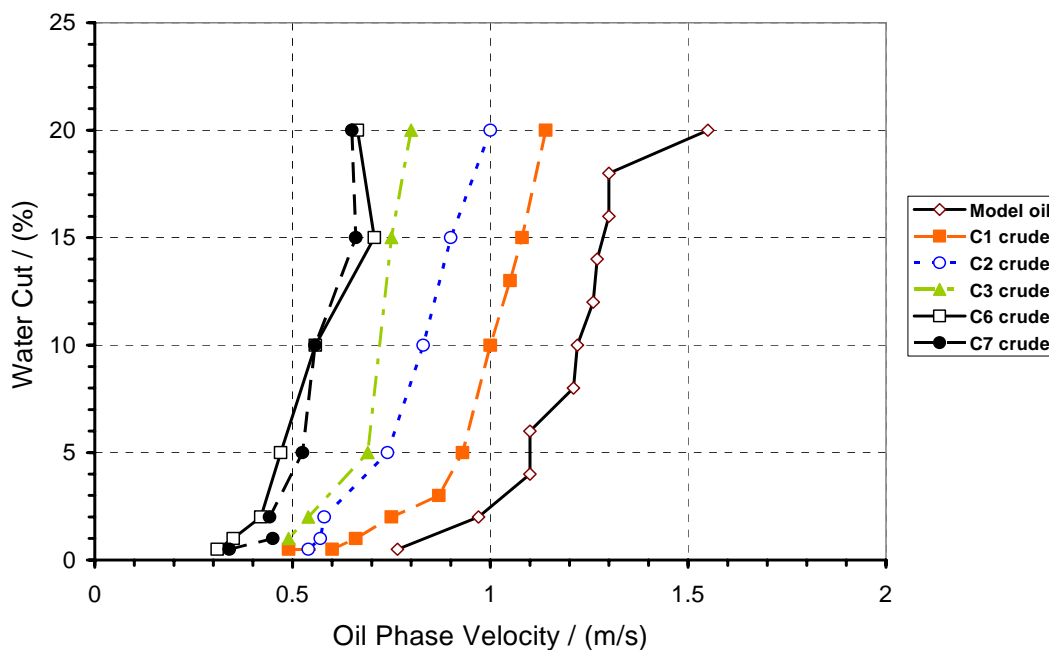


Figure 66 Comparison of the transition lines from intermittent wetting to oil wetting for model oil and five different crude oils in doughnut cell experiments.

The objective of the doughnut cell development is that by conducting experiments on a small scale gives an accurate prediction on phase wetting regime of oil-water two-phase pipe flow, in particular for oilfield large diameter pipelines. One of the most challenging problems is how to scale up test results from small scale doughnut cell to large scale pipe flow. Since some experiments with the same crude oils are carried out in both doughnut cell and 4-inch ID multiphase flow loop, the comparison of test results

can shed a light on the linkage between the two different test systems. Figure 67 shows comparisons of the transition lines from intermittent wetting to oil wetting for model oil and three different crude oils in flow loop and doughnut cell experiments. The experimental errors are included and shown on each transition points in the comparisons. For the light oils including the model oil and C1 crude oil, some degree of agreement can be seen at water cut below 4%, but major differences occur when water cut is higher than 4% and it increases with increasing water cut. Much higher oil phase velocity is required to entrain a given water cut in the flow loop than in the doughnut cell. However, for the heavier oils like C2 and C3 crude oils, a good agreement is found at water cut below 8%. Although there are differences between the transition lines of C2 and C3 in two test systems, the degree of the difference is smaller than that found for light oils.

Corrosion inhibitor, “quat” is used in the model oil-brine two-phase flow in the doughnut cell. The phase wetting maps of the model oil-brine with 1, 5 and 20 ppm “quat” additions in the doughnut cell experiments are shown in Figure 68, Figure 69 and Figure 70, respectively. Corrosion inhibitor can lower the oil-water interfacial tension, which makes water entrainment easier towards lower values of the oil phase velocity. Figure 71 shows comparison of the phase wetting transition lines at different concentrations of “quat”. It can be seen that increasing “quat” concentration leads to transition line shifting to the lower critical entrainment oil phase velocity at given water cut. The results imply that inhibitor addition helps enhance oil wetting in oil-water two-phase flow.

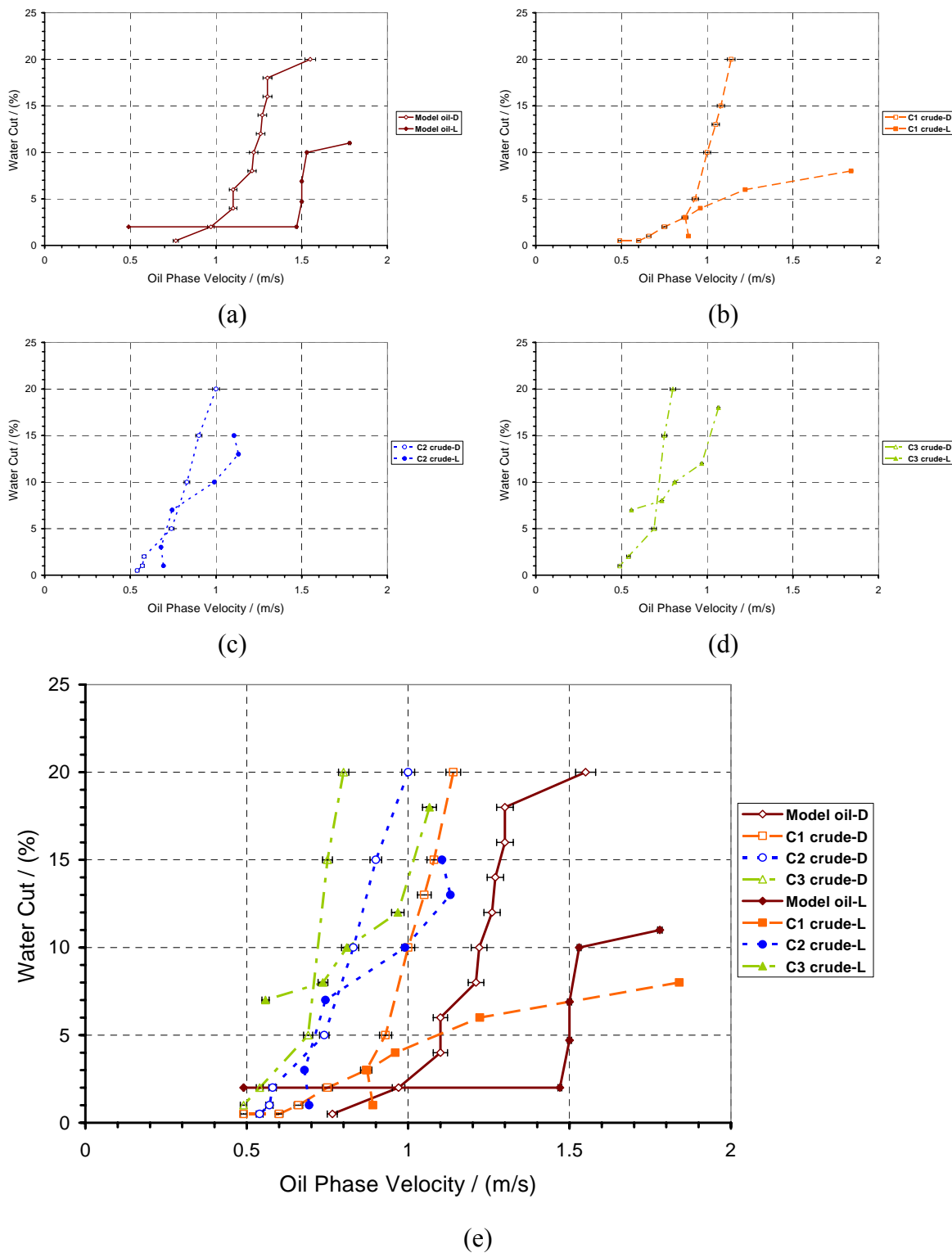


Figure 67 Comparison of the transition lines from intermittent wetting to oil wetting. (a) for model oil, (b) for C1 crude, (c) for C2 crude, (d) for C3 crude and (e) for four different oils in flow loop (L) and doughnut cell (D) experiments.

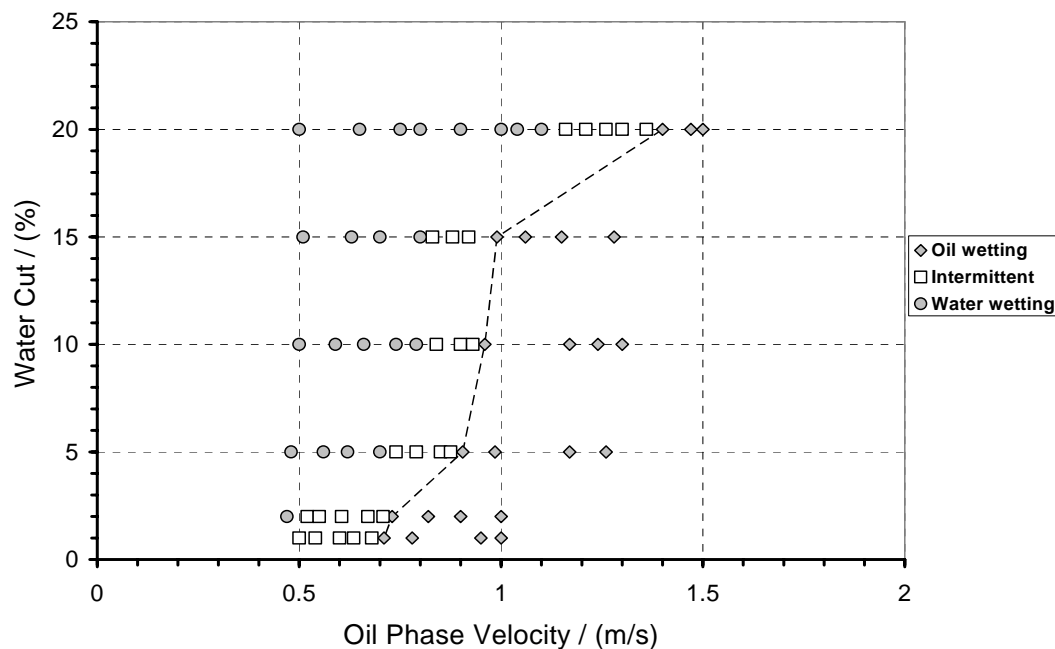


Figure 68 Phase wetting map of model oil-brine with 1 ppm “quat” addition in doughnut cell experiments. The dotted line shows a transition from intermittent to oil wetting.

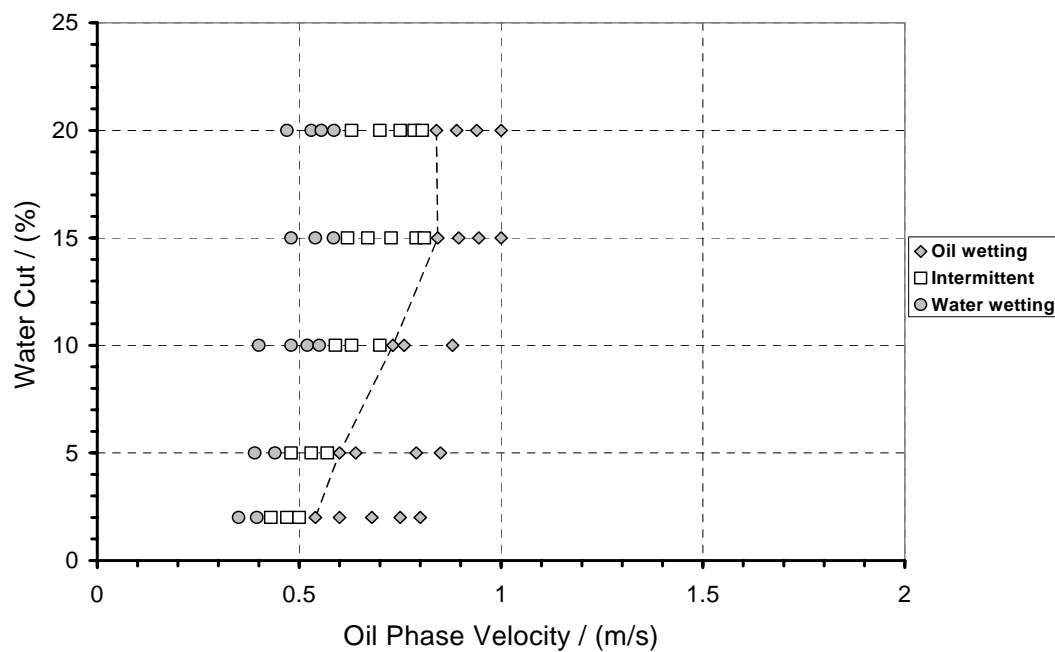


Figure 69 Phase wetting map of model oil-brine with 5 ppm “quat” addition in doughnut cell experiments. The dotted line shows a transition from intermittent to oil wetting.

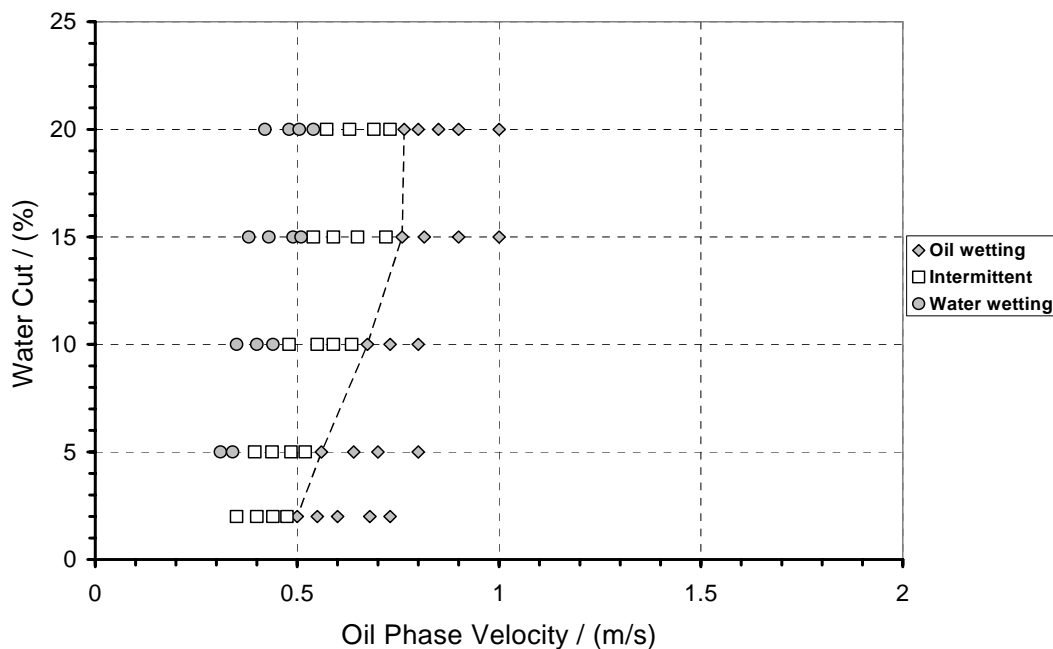


Figure 70 Phase wetting map of model oil-brine with 20 ppm “quat” addition in doughnut cell experiments. The dotted line shows a transition from intermittent to oil wetting.

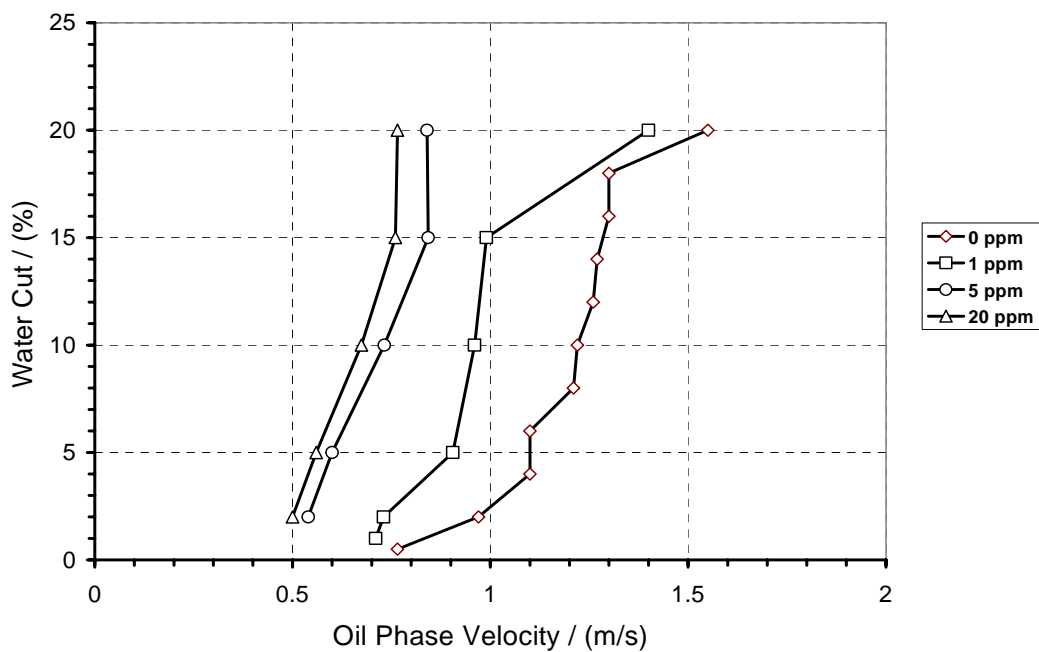


Figure 71 Comparisons of the transition lines from intermittent wetting to oil wetting for model oil-brine with 0, 1, 5 and 20 ppm “quat” inhibitor addition in the doughnut cell experiments.

### **7.3 Summary**

A unique small scale apparatus, called the doughnut cell, is developed in this work to study phase wetting in oil-water two-phase flow. Wall conductance probes are successfully transferred from the flow loop to doughnut cell instrumentation setup. The phase wetting maps are constructed for the model oil and five different crude oils in the doughnut cell experiments. Comparison of the transition lines from different oils shows that the physical properties and chemistry of the oil phase are of key importance to determine the critical entrainment velocity. Comparison between two test systems shows that a dimension mismatch needs to be corrected for. A scale up method using mechanistic phase wetting prediction model to correct the dimension mismatch between the doughnut cell and the flow loop will be described in Chapter 8. Addition of corrosion inhibitor makes the phase wetting transition line move towards the lower oil phase velocity due to a decrease in the oil-water interfacial tension, which enhances the possibility of achieving oil wetting regime in oil-water two-phase flow.

## CHAPTER 8: PHASE WETTING AND CARBON DIOXIDE CORROSION

### INHIBITION PREDICTION MODELS

#### 8.1 Phase wetting prediction model

##### 8.1.1 Model development

A model oil and seven different crude oils, which were provided by the project sponsors, have been tested to determine phase wetting regimes in the laboratory small scale and large scale test systems. A phase wetting prediction model is truly helpful for oilfield production operation and future project design. The development of the phase wetting prediction model for oil-water two-phase flow will be presented below.

The theory behind the flow pattern transition between stratified flow and full dispersed flow proposed by Brauner (2001) is adopted for developing transition criteria between water entrainment and breakout. In Brauner's (2001) theory, two maximum droplet sizes are calculated for dilute (2-33) and dense (2-43) dispersions, respectively. The maximum droplet size in dilute dispersion, which comes from Hinze's (1955) droplet size model, only considers a single dispersed water droplet. It was discussed by Brauner (2001) that an assumption (8-1) in which  $\rho_c$  is the density of the continuous phase,  $\varepsilon_d$  is the hold up of the dispersed phase and  $\rho_m$  is the density of the oil-water mixture, needs to be satisfied in the dilute dispersions. In homogeneous flow, the mixture density is calculated with Equation (2-36). Substituting it into Equation (8-1), it is found that dilute dispersion is valid only when the holdup of entrained liquid phase is close to zero ( $\varepsilon_d \ll 1\%$ ). This condition is very impractical for oil-water two-phase pipe flow as occurs in the oil and gas industry. The calculation of maximum droplet size proposed by

Brauner (2001) in dense dispersion takes coalescence of many dispersed droplets into account. A balance between the total surface energy of dispersed phase and the turbulent kinetic energy is applied. Brauner (2001) suggested that the maximum droplet size is the largest of the two values obtained from dilute and dense dispersions. However, as discussed above, it is impractical to satisfy the dilute dispersion criterion, Equation (8-1). It is reasonable to pick the value from dense dispersion as maximum dispersed droplet size, Equation (8-2), which was discussed in Section 2.2.2, Equation (2-43).

$$\frac{\rho_c(1-\varepsilon_d)}{\rho_m} \approx 1 \quad (8-1)$$

$$d_{\max} = 2.22 \left( \frac{\rho_c U_c^2}{\sigma} \right)^{-0.6} \left( \frac{\varepsilon_d}{1-\varepsilon_d} \right)^{0.6} \left[ \frac{\rho_m}{\rho_c(1-\varepsilon_d)} f \right]^{-0.4} D^{0.4} \quad (8-2)$$

Barnea (1986 and 1987) proposed calculations of two critical droplet sizes from effects of gravity (8-3) and distortion (8-4) to determine separation of dispersed droplets from the continuous phase. In a conservative consideration the critical droplet size is the smallest one of the two values (8-5).

$$d_{cg} = \frac{3}{8} \frac{\rho_c U_m^2 f}{|\rho_d - \rho_c| g \cos \beta} \quad (8-3)$$

$$d_{cd} = \left( \frac{0.4\sigma}{|\rho_d - \rho_c| g \cos \beta'} \right)^{0.5}$$

$$\text{With } \beta' = \begin{cases} |\beta|, & |\beta| < 45^\circ \\ 90^\circ - |\beta|, & |\beta| > 45^\circ \end{cases} \quad (8-4)$$

$$d_{crit} = \text{Min}(d_{cg}, d_{cd}) \quad (8-5)$$

At this point, a final transition criterion between water entrainment and breakout is formulated in Equation (8-6). If the maximum droplet size calculated by Equation (8-2) is less than the critical droplets size calculated by Equations (8-3), (8-4) and (8-5), all the water is entrained in the flowing oil phase leading to oil wetting regime. If the maximum droplet size is larger than the critical droplet size, water breakout occurs leading to intermittent wetting or water wetting. When the two droplet sizes equal each other, it is at a transition point from the intermittent wetting to oil wetting. This allows us to calculate the minimum critical oil velocity for water entrainment.

$$d_{\max} \leq d_{\text{crit}} \quad (8-6)$$

Although much attention is paid to water dispersion in the continuous oil phase, oil can be entrained in the flowing water phase above the phase inversion point. It is essential to determine which of the liquid phases is continuous and which is dispersed in oil-water two-phase flow at any given water cut. The phase inversion point is a critical transition water cut between water-in-oil dispersion to oil-in-water dispersion. A prediction of phase inversion point ( $\varepsilon_{inv}$ ) proposed by Arirachakaran *et al.* (1989) is adopted (8-7). If the input water cut is less than or equals the phase inversion point, oil will be the continuous phase once the dispersed flow is formed. If the input water cut is greater than the phase inversion point, oil is entrained in the continuous water phase.

$$\varepsilon_{inv} = 0.5 - 0.1088 \log \left( \frac{\mu_o}{\mu_w} \right) \quad (8-7)$$

At this point, a phase wetting prediction model for oil-water two-phase flow is built based on calculation of maximum and critical droplet sizes and phase inversion

point. The explanations of physical processes are discussed in Chapter 2 as well as in this chapter. A flow chart of the phase wetting prediction model is shown in Figure 72. It should be noted that the predicted phase wetting regime by the model is only applied on the bottom portion of the pipe inner surface. Several parameters are required as model inputs, which include the pipe diameter and inclination, the densities of water and oil phases, the viscosities of water and oil phases, the oil-water interfacial tension, the superficial oil velocity and water cut (or the superficial water velocity). The phase inversion point is calculated with Equation (8-7). If the input water cut is smaller than the phase inversion point, oil is the continuous phase. Otherwise, water is the continuous phase. The maximum and critical droplet sizes are calculated with Equations (8-2), (8-3), (8-4) and (8-5) for either water or oil phase. In both oil continuous and water continuous flows, if the maximum droplet size is greater than the critical droplet size, where the continuous liquid phase cannot hold up all the dispersed liquid phase, stratified flow forms and leads to either water wetting or intermittent wetting on the bottom of the pipe wall. In the water continuous flow, if the maximum droplet size is less than or equal to the critical droplet size, all the oil phase is entrained in the flowing water phase, which leads to water wetting on the whole pipe circumference. On the contrary, if the maximum water droplet size is less than or equal to the critical water droplet size in an oil continuous flow, water-in-oil dispersed flow occurs, which leads to oil wetting regime on the whole pipe circumference.

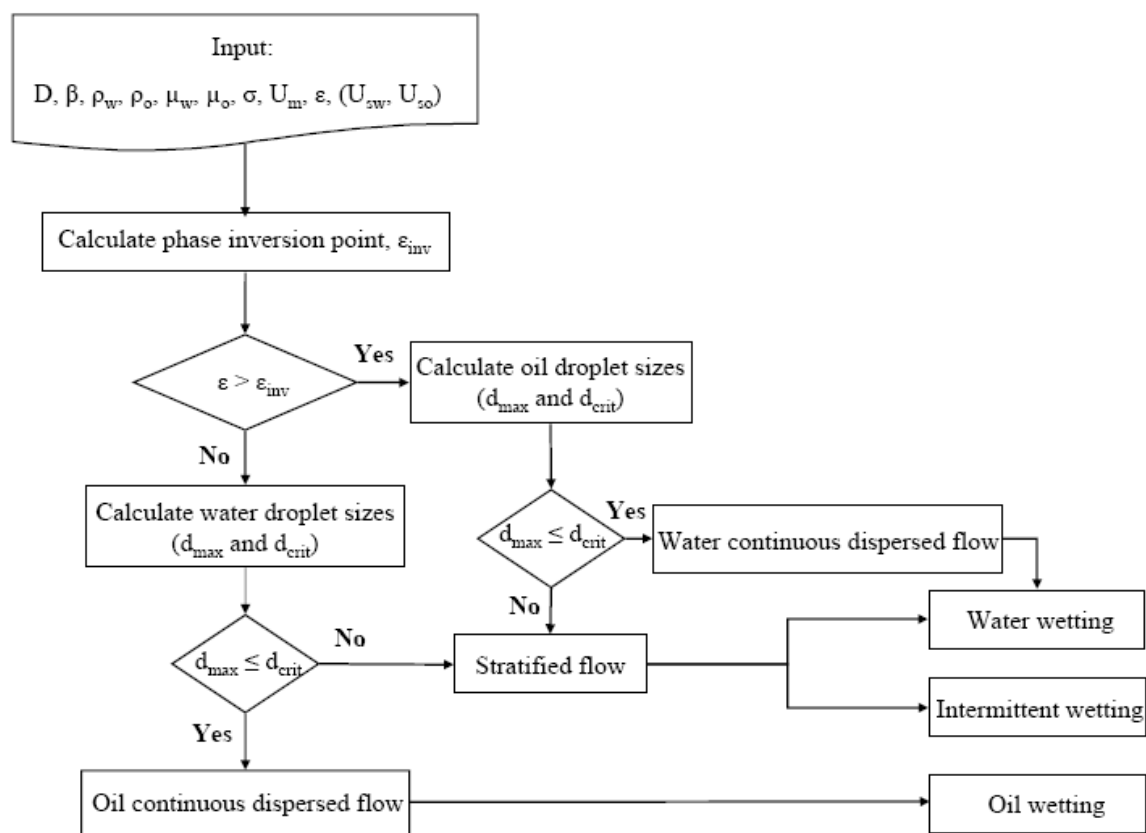


Figure 72 Flow chart of the phase wetting prediction model.

The entrainment and breakout criteria (8-6) can also be applied in the model to predict the critical entrainment velocity for the continuous phase. For example, if oil is the continuous phase and the maximum water droplet size is greater than the critical water droplet size at input water cut and oil phase velocity, one may want to know at which oil phase velocity all the water will be entrained. An iteration method is used to increase the oil phase velocity and re-check if the entrainment criterion is achieved or not. Once it is achieved during the iteration process, the critical entrainment velocity for the continuous phase is found, which is very helpful for the engineers and oilfield operators to maintain stable oil wetting regime in the pipelines.

In the stratified flow regime, either water wetting or intermittent wetting can occur. In this work, no effort is made to predict the transition boundary between water wetting and intermittent wetting. However, from corrosion point of view, it is essential to know some key parameters for CO<sub>2</sub> corrosion rate prediction, such as water layer thickness and *in situ* water phase velocity. The three-layer stratified flow model described in Chapter 2 is adopted in this study to connect the water wetting and intermittent wetting regimes with the CO<sub>2</sub> corrosion rate prediction model.

#### 8.1.2 Linkage between doughnut cell and flow loop

The comparison (Figure 67) of the transition lines from intermittent wetting to oil wetting in the doughnut cell and flow loop experiments shows that the two different test systems generate empirical differences for model oil and different crude oils. Although it was found that heavier crude oils have better agreements between the two test systems at water cut below 8%, a scale up method should be applied in all cases to correct the mismatch of the transition lines found in the doughnut cell and the flow loop. The mechanistic phase wetting prediction model described in Section 8.1.1 is built on the physics of water entrainment and breakout in pipe flow, which apply in the doughnut cell as well. The phase wetting prediction model is proposed to link between the two test systems. An obvious dimension difference can be observed, where the cross section of the flow loop is circular shaped but rectangular for the doughnut cell flow channel. The concept of a hydraulic diameter is applied for adopting the rectangular shaped cross section of the doughnut cell to the circular pipe diameter. The hydraulic diameter of the doughnut cell flow channel can be calculated by using Equation (8-8), in which H is the

height and  $W$  is the width of the flow channel. The 2.75 inch height and 1.81 inch width of the doughnut cell setup for all the experiments corresponds to a 2.18 inch hydraulic pipe diameter.

$$D_H = \frac{2 \cdot H \cdot W}{H + W} \quad (8-8)$$

The converted 2.18 inch hydraulic diameter for the doughnut cell flow channel is used as input in the phase wetting prediction model (Figure 72). Since this value is almost half of the flow loop 4-inch pipe diameter, it is expected that the transition lines in the doughnut cell experiments shift to the lower oil phase velocity at given water cut compared with that in the flow loop experiments. However, this dimension mismatch can be corrected by the mechanistic phase wetting prediction model. Figure 73 shows a comparison of the predicted transition lines from the intermittent wetting to oil wetting by the model for the model oil in both the flow loop and the doughnut cell. The difference of the calculated critical entrainment oil phase velocity at constant water cut is caused by the pipe diameter difference for the two test systems. The experimental results from the doughnut cell can be scaled up by adding the difference of the oil phase velocity predicted by the model at each test point. In this way, a phase wetting transition line for a specific oil in a large scale flow loop pipe flow can be predicted by conducting only small scale doughnut cell experiments, which requires much smaller amounts of the oil.

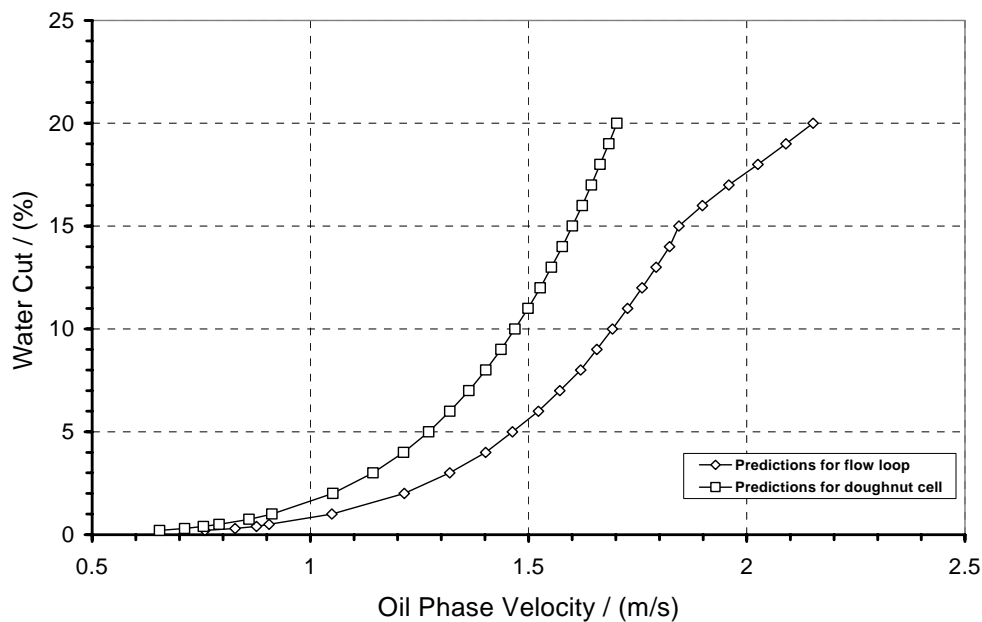


Figure 73 Comparison of the predicted transition lines for model oil in the flow loop (4 inch) and the doughnut cell (2.18 inch) by the mechanistic phase wetting prediction model from intermittent wetting to oil wetting.

### 8.1.3 Model verification

The developed phase wetting prediction model is verified with the experimental results of the model oil and seven different crude oils in the large scale flow loop and the small scale doughnut cell. The scale up method by using the phase wetting model to link the doughnut cell and the flow loop test systems is verified by comparing the results from the two test systems. Figure 74 shows the comparison of the empirical phase wetting transition lines for model oil and five different crude oils in the multiphase flow loop experiments (marked “L”) with the phase wetting model predictions (marked “P”). For the model oil (Figure 74 (a)), the model prediction has a good agreement with the empirical transition line except for low water cut region (< 2%). For the C1 light crude oil (Figure 74 (b)), the model overpredicts the critical entrainment oil phase velocity in

comparison to the empirical results when the water cut is below 8%. Since there is no empirical transition point determined for C1 crude oil at water cut over 8%, it is unable to validate the model prediction performance in that range of the water cut.

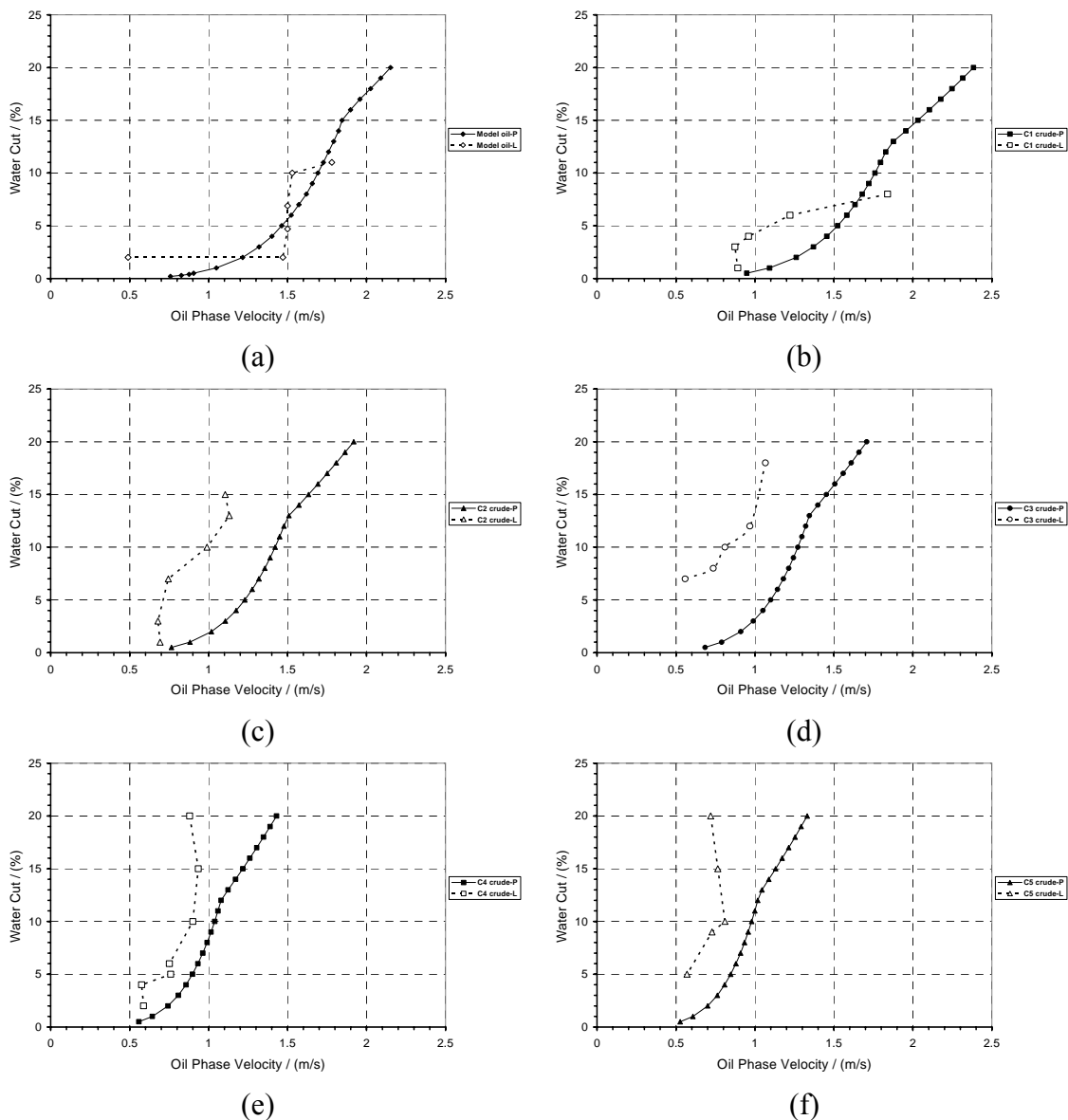


Figure 74 Comparison of the empirical phase wetting transition lines, (a) for mode oil, (b) for C1, (c) for C2, (d) for C3, (e) for C4 and (f) for C5 crude oils in multiphase flow loop (L) tests with the model predictions (P).

For other crude oils (Figure 74 (c)-(f)), the model always overpredicts the critical oil phase velocity for full water entrainment, *i.e.*, oil wetting. A factor of safety is used to evaluate the model performance, which is calculated as the critical entrainment oil phase velocity predicted by the model divided by that obtained from flow loop experiments at the same water cut. For example, at water cut of 10% for C2 crude oil (Figure 74 (c)), flow loop experimental results show that critical entrainment oil phase velocity is 0.99m/s and the model prediction value is 1.42 m/s, which gives factor of safety 1.4. The factor of safety greater than one means that the model prediction is conservative in comparison to empirical results. The calculated factors of safety based on the comparisons of experimental results and model predictions are listed in Table 26. At this point, it can be concluded that the predictions of the phase wetting model are conservative in comparison to all the tested crude oils in flow loop pipe flow, although the prediction has a good agreement with the model oil except for water cut lower than 2%.

Table 26 List of the factor of safety for the model oil and five different crude oils in the flow loop tests.

Oil	Water cut / (%)	1	2	3	4	5	6	7	8	9	10	12	15	18	20
		Factor of safety													
Model			2.5			1		1			1.1				
C1		1.2		1.6	1.5		1.3		0.9						
C2		1.3		1.6				1.8			1.4		1.5		
C3								2.1	1.6		1.6	1.4		1.5	
C4			1.3		1.5		1.2				1.2				1.6
C5						1.5				1.3					1.8

It was found that the addition of corrosion inhibitor, either “quat” or fatty amino, causes a great reduction in oil-water interfacial tension. The performance of the phase wetting model is compared to the empirical phase wetting transition line from model oil-brine-inhibitor system by adjusting the value for interfacial tension. The experiments of model oil-brine with addition of 5 ppm “quat” based on the total liquid volume are conducted in the multiphase 4 inch flow loop. Figure 75 shows the phase wetting map of model oil-brine-5ppm “quat” in horizontal flow loop experiments. The solid and dotted lines on the figure are the phase wetting transition lines determined from model predictions and empirical results, respectively. It can be seen that the model predictions deviate from the empirical line by a factor of safety of 1.1, except for 1.6 factor of safety at low water cut region ( $\leq 2\%$ ). It is reasonable to claim that the model predictions are good for the phase wetting transition in model oil-brine-inhibitor system. Addition of 5 ppm “quat” lowers the oil-water interfacial tension to 5.3 dyne/cm, which is much lower than the values of crude oil-brine interfacial tension. The conservative performance of the model to all the tested crude oils may result from crude oil chemistry.

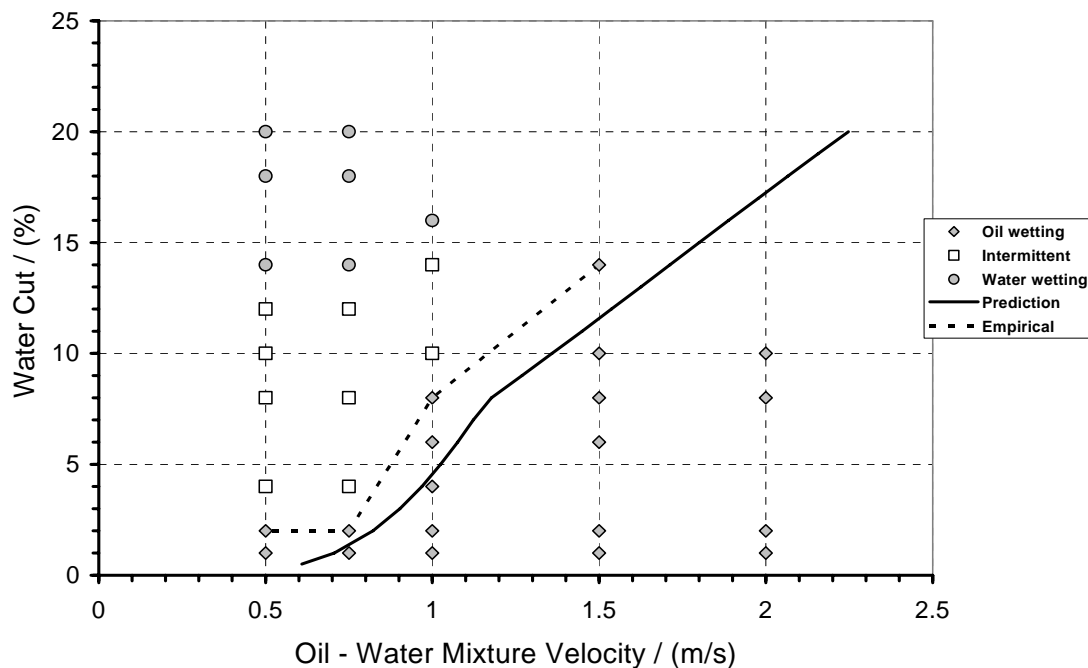


Figure 75 Phase wetting map of the model oil-brine with 5 ppm “quat” inhibitor addition in horizontal flow loop experiments. The solid and dotted lines are the phase wetting transition lines from model predictions and empirical test results, respectively.

The performance of the phase wetting prediction model is also verified with the experiments for model oil and C1, C2, C3, C6 and C7 crude oils in the doughnut cell. Figure 76 shows the comparison of the empirical phase wetting transition lines in the doughnut cell experiments (marked “D”) with the model predictions (marked “P”). Figure 76 shows that the predictions are conservative for all the tested crude oils, *i.e.*, the model overpredicts the critical oil phase velocity for full water entrainment compared to the empirical results, same as for the flow loop results (Figure 74). The calculated factors of safety for the model oil and five different crude oils in the doughnut cell tests are listed in Table 27.

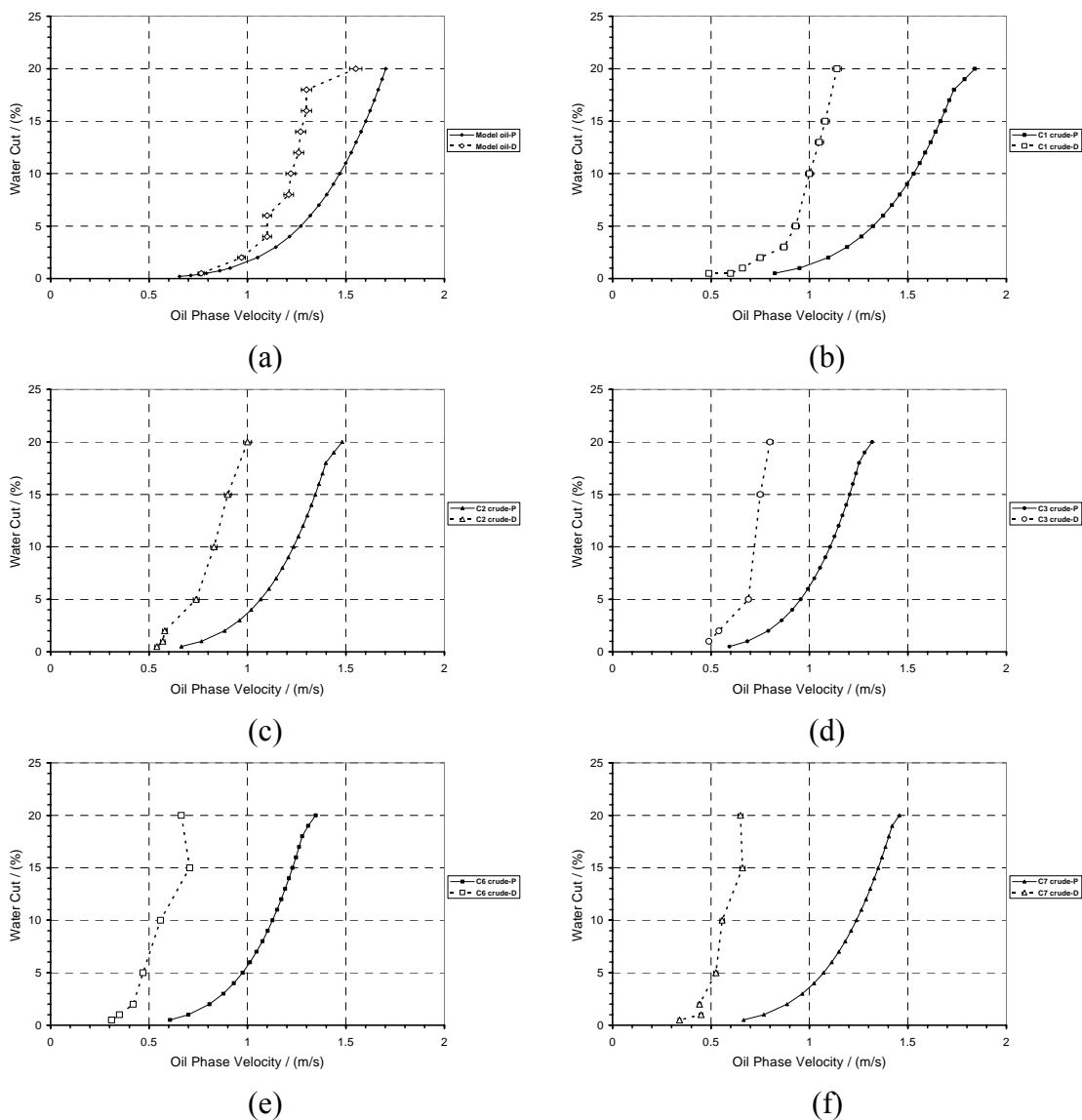


Figure 76 Comparison of the empirical phase wetting transition lines, (a) for model oil, (b) for C1, (c) for C2, (d) for C3, (e) for C6 and (f) for C7 crude oils in the doughnut cell (D) tests with the phase wetting model predictions (P).

Table 27 Factor of safety for the model oil and five crude oils in the doughnut cell tests.

Oil	Factor of safety
Model	1 – 1.3
C1	1.4 – 1.6
C2	1.2 – 1.5
C3	1.3 – 1.6
C6	1.7 – 2.1
C7	1.7 – 2.2

Figure 77 shows comparison of the empirical phase wetting transition lines for the model oil-brine with 1, 5 and 20 ppm of “quat” inhibitor additions in the doughnut cell (marked “D”) with model predictions (marked “P”). The calculated factors of safety are between 1.1 to 1.5 for all cases, which indicate higher predicted critical oil phase velocity for full water entrainment than empirical oil phase velocity. The result of the corrosion inhibitor test series in the doughnut cell is consistent with the results from the flow loop experiments, which show lower oil-water interfacial tension leading to lower critical oil velocity for full water entrainment.

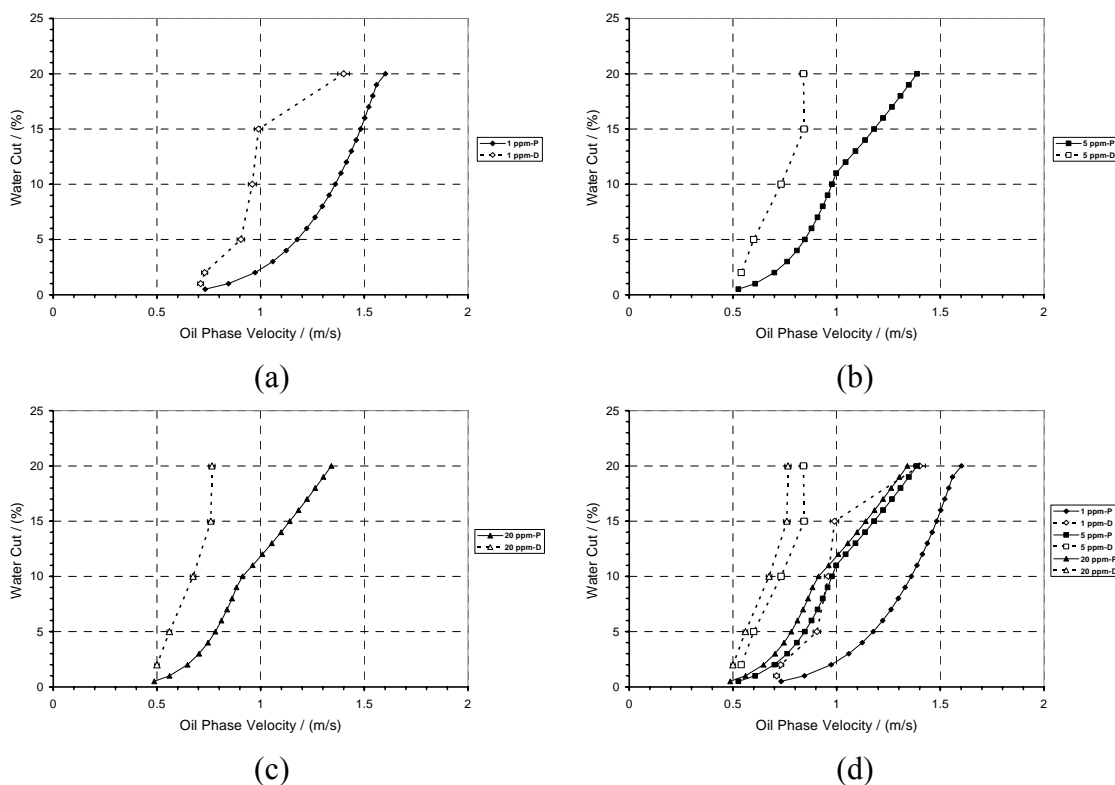


Figure 77 Comparison of the empirical phase wetting transition lines for the model oil-brine with (a) for 1 ppm, (b) for 5 ppm, (c) for 20 ppm “quat” inhibitor additions and (d) for all the test concentrations in the doughnut cell (D) tests with the model prediction (P).

The objective of the doughnut cell is that quick phase wetting experiments are conducted on small scale level and then the results are used to predict actual phase wetting regime in large scale pipe flow. As discussed above, dimension difference between the doughnut cell and the flow loop is corrected by using the hydraulic diameter concept. The results in the doughnut cell can be scaled up by the developed phase wetting prediction model with the calculated hydraulic diameter for the doughnut cell flow channel. Differences of the predicted critical entrainment oil phase velocities by phase wetting model in the two test system at each given water cut are calculated. The velocity difference between the predicted values in the doughnut cell (2.19 inch) and in the flow loop (4 inch) is then added to the empirical doughnut cell results. For example, the oil phase velocity difference in the two test systems for the model oil at 20% water is 0.45 m/s (Figure 73). The empirical result of the model oil-brine doughnut cell test shows that 1.55 m/s oil phase velocity is required for 20% water entrainment (Figure 60). This critical oil velocity is scaled up from 2.19 inch doughnut cell to 4 inch flow loop by adding 0.45 m/s velocity difference between the two systems. To verify the proposed scale up method, comparisons of the phase wetting transition lines for model oil, C1, C2 and C3 crude oils in the flow loop (marked "L") with the transition lines in the doughnut cell experiments, which are corrected by the phase wetting prediction model (marked "D+C"), are shown in Figure 78. It can be seen that the corrected transition lines (marked "D+C") for heavier crude oils (C2 and C3) have good agreement with the empirical lines in the flow loop experiments. However, gaps between the corrected transition lines in the

doughnut cell and the lines in the flow loop experiments are still found for light oil (model oil and C1 crude), in particular at water cut of 2 to 13%.

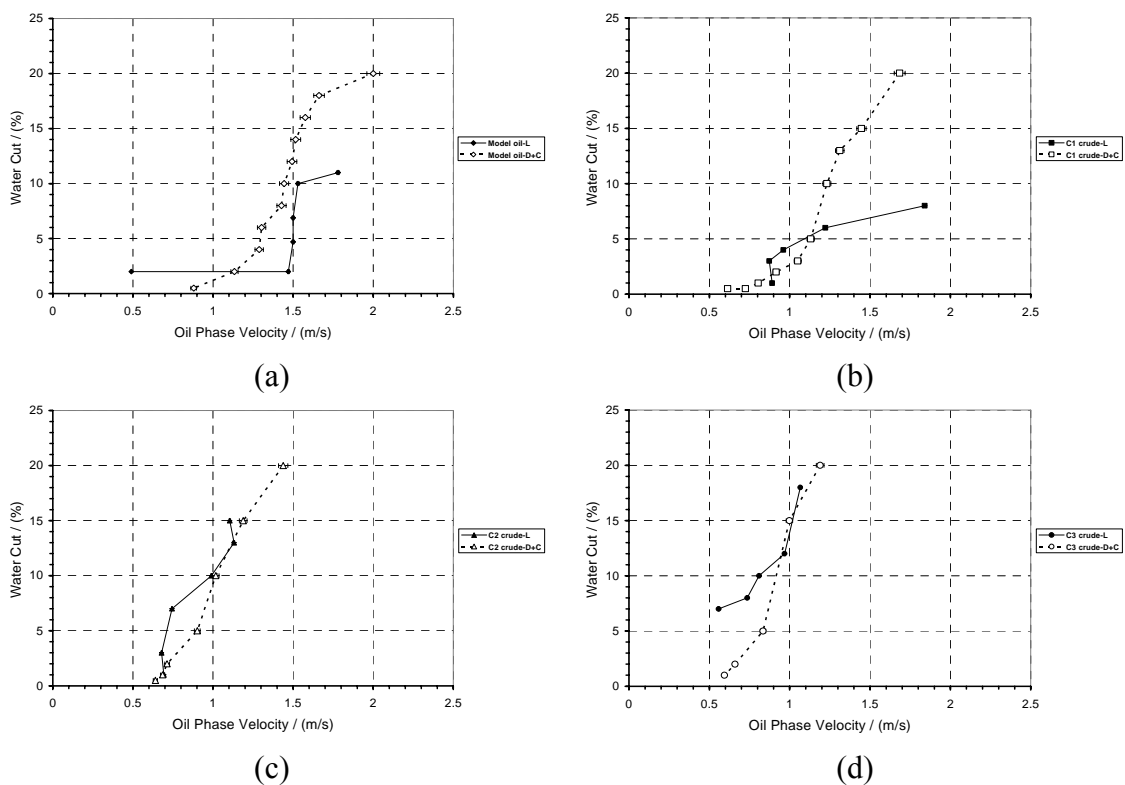


Figure 78 Comparison of the phase wetting transition lines, (a) for model oil, (b) for C1, (c) for C2 and (d) for C3 crude oils in the flow loop (L) with that in the doughnut cell experiments corrected by the phase wetting model (D+C).

## 8.2 Carbon dioxide corrosion inhibition model

### 8.2.1 Model development

A carbon dioxide corrosion inhibition model is developed to predict the corrosion rate with an addition of corrosion inhibitor. As discussed in Chapter 2, the simple approach for predicting inhibition efficiency is to use adsorption isotherm, which is also commonly applied for adsorption of surfactants. Under mechanism of inhibition by a

surface coverage effect, the inhibition efficiency is assumed to equal the surface coverage. A relationship between the surface coverage with the concentration of corrosion inhibitor in the bulk solution is built by the adsorption isotherm. In this work, Langmuir adsorption isotherm (8-9), which is explained in Section 2.3.2 is used to fit the experimental data. The measured inhibition efficiencies (surface coverage,  $\theta$ ) at different inhibitor concentrations for “quat” and fatty amino in glass cell experiments are shown in Figure 37. The unknown parameter ( $K_{a/d}$ ) is solved by using least square linear regression method in MATLAB. Figure 79 shows the plot of the corrosion inhibition experimental data of “quat” and fatty amino fitted by the Langmuir adsorption isotherm.

$$K_{a/d}c_{inh} = \frac{\theta}{1-\theta} \quad (8-9)$$

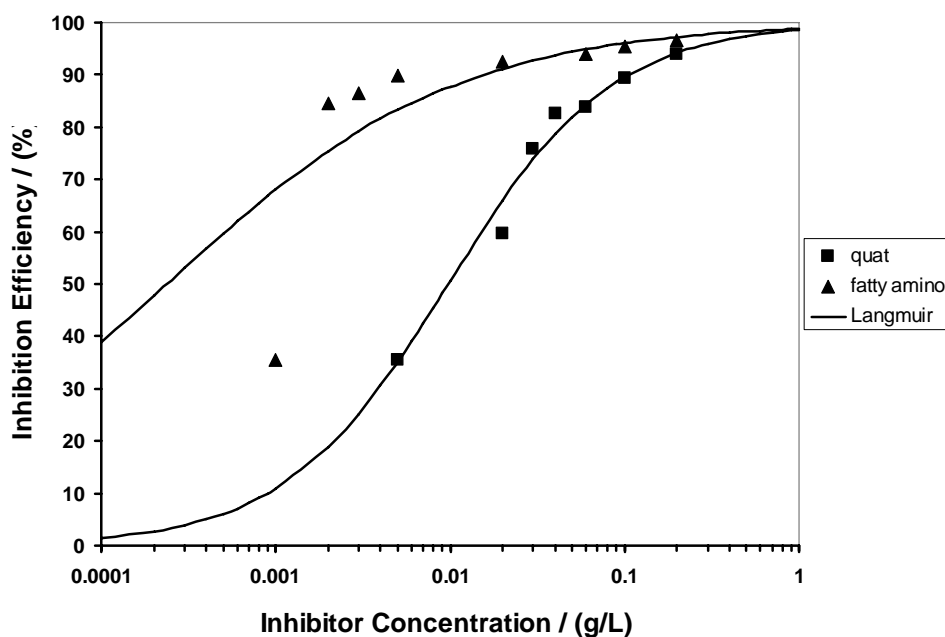


Figure 79 Corrosion inhibition experimental data of “quat” and fatty amino inhibitors fitted by the Langmuir adsorption isotherm.

The Langmuir isotherm fits the experimental data well, in particular for the high inhibition efficiency range. The correlation coefficients (R-squared values) which represent how good the data fit to the model are 0.72 and 0.98 for fatty amino and “quat”, respectively. However, it can be seen that the Langmuir isotherm is unable to fit the data point of 1 ppm fatty amino, which has a sharp increase in the inhibition efficiency for fatty amino from 1 to 2 ppm addition. The best-fit values of the adsorption/desorption equilibrium constants ( $K_{a/d}$ ) are 81.3 and 71.9 for fatty amino and “quat”, respectively. Using these calculated constants ( $K_{a/d}$ ), the inhibition efficiency can be calculated with the Langmuir isotherm at given “quat” or fatty amino inhibitor concentrations. The inhibited CO<sub>2</sub> corrosion rate is then determined by multiplying the inhibition efficiency with the uninhibited CO<sub>2</sub> corrosion rate.

The CO<sub>2</sub> corrosion rate in oil-water two-phase pipe flow is highly dependent on the phase wetting regimes. It is essential to build a connection between existing CO<sub>2</sub> corrosion rate prediction models used for single water phase with the phase wetting prediction model developed in this work. Figure 80 shows a strategy of predictions of the uninhibited and inhibited CO<sub>2</sub> corrosion rate in oil-water two-phase pipe flow by linking the phase wetting, three-layer stratified flow, CO<sub>2</sub> corrosion and inhibition models. The same approach has been used by Nesic *et al.* (2004 and 2008b) to integrate CO<sub>2</sub>/H<sub>2</sub>S corrosion model with multiphase flow model. The phase wetting prediction model gives the answer of phase wetting regimes by using strategy shown in Figure 72. If an oil wetting regime is predicted, absence of corrosion is assumed. Under both water wetting and intermittent wetting, the three-layer stratified flow model calculates the thickness and

velocity of the water layer flowing at the bottom of the pipe. The CO<sub>2</sub> corrosion model developed at Ohio University is included in MULTICORP, which is a proprietary program only accessible to companies which sponsor the Institute for Corrosion and Multiphase Technology, and included in FREECORP which is a free model available to public and include CO<sub>2</sub>/H<sub>2</sub>S corrosion models which are accessible in literature. They are all built based on the mechanisms of CO<sub>2</sub> corrosion discussed in Chapter 2. Several key parameters which include temperature (T), total pressure (P), partial pressure of CO<sub>2</sub> gas (P<sub>CO<sub>2</sub></sub>), and pH of aqueous solution are required by the CO<sub>2</sub> corrosion prediction model. The uninhibited CO<sub>2</sub> corrosion rate is predicted by the corrosion model and then the inhibition model built for specific corrosion inhibitor with Langmuir adsorption isotherm gives the inhibited CO<sub>2</sub> corrosion rate. The inhibition model requires empirical tests in glass cells or autoclaves to build relationships between surface coverage ( $\theta$ ) and inhibitor concentration ( $c_{inh}$ ). Addition of corrosion inhibitors can produce a decrease in oil-water interfacial tension, which affects oil-water phase wetting regime. Empirical tests need to be conducted to determine the relationship between oil-water interfacial tension ( $\sigma$ ) and inhibitor concentration ( $c_{inh}$ ). The empirical value of the oil-water interfacial tension at given inhibitor concentration is then an input of the phase wetting prediction model. A strategy of the CO<sub>2</sub> corrosion rate prediction (Figure 80) includes the effects of corrosion inhibitor by considering both changes in oil-water interfacial tension and surface coverage. The effect of wettability alternation of the steel surface from hydrophilic to hydrophobic on the CO<sub>2</sub> corrosion rate is not modeled in this work.

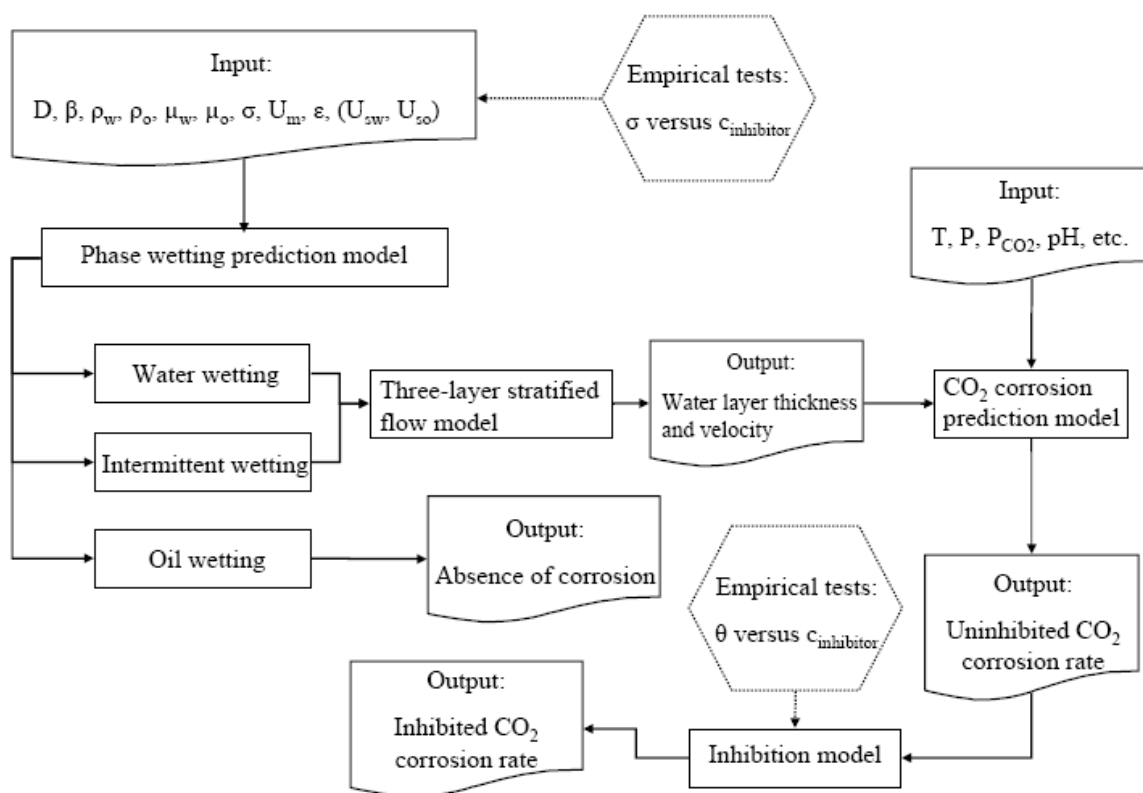


Figure 80 A strategy of the uninhibited and inhibited CO<sub>2</sub> corrosion rate predictions for oil-water two-phase pipe flow by connecting the phase wetting model, three-layer stratified flow model, CO<sub>2</sub> corrosion prediction model and corrosion inhibition model.

### 8.3 Summary

A mechanistic phase wetting model is developed to predict phase wetting regime in oil-water two-phase pipe flow. The model is also used as a scale up method to correct the dimension difference between the doughnut cell and the flow loop. Both experimental results in the flow loop and the doughnut cell for model oil and seven different crude oils are applied to validate the phase wetting model. The model predictions have good agreements with empirical results for model oil in the doughnut cell and in the flow loop. However, the performances of the model are conservative to all the tested crude oils, although better agreements are achieved for heavier crude oils (like C4 and C5). The

corrected phase wetting transition lines by using hydraulic diameter in the phase wetting model for the doughnut cell experiments show a better agreement with the flow loop results.

The model overpredicts the critical entrainment oil phase velocities (in a conservative way) compared to the empirical results of model oil-brine with “quat” inhibitor addition in the flow loop and in the doughnut cell. But both experimental results and model predictions agree with each other in that addition of corrosion inhibitor makes water easier to be entrained (the lower water entrainment oil phase velocity required) due to lowering of oil-water interfacial tension.

A strategy is proposed to predict uninhibited and inhibited CO<sub>2</sub> corrosion rates in oil-water two-phase pipe flow by connecting the phase wetting, three-layer stratified flow, CO<sub>2</sub> corrosion and inhibition models. The effects of surface coverage and surface active property of corrosion inhibitor on corrosion rate are considered in the strategy.

## CHAPTER 9: CONCLUSIONS AND FUTURE WORK

### 9.1 Conclusions

A comprehensive study including both experimental and modeling approaches has been carried out to investigate phase wetting regimes, CO<sub>2</sub> corrosion and corrosion inhibition in oil-water two-phase flow. The main findings and achievements in this research are summarized following:

- Three phase wetting regimes are identified: water wetting, intermittent wetting and oil wetting.
- An absence of internal corrosion only occurs under oil wetting regime. Both water wetting and intermittent wetting lead to internal corrosion.
- It is found that heavy crude oil (higher density and viscosity) has better entrainment capability compared to light crude oil.
- A unique small scale apparatus, called the doughnut cell, is developed to study phase wetting and CO<sub>2</sub> corrosion in oil-water two-phase flow.
- The predictions of the mechanistic phase wetting model have good agreements with empirical results for model oil in the doughnut cell and in the flow loop. However, the model overpredicts the critical entrainment oil phase velocities in comparison to empirical results of all the tested crude oils, although better agreements are achieved for heavier crude oils.
- The corrected phase wetting transition lines by using hydraulic diameter of the doughnut cell flow channel in the phase wetting model show a better agreement with the flow loop results.

- A CO<sub>2</sub> corrosion inhibition model is built for “quat” and fatty amino using Langmuir adsorption isotherm, which creates a relationship between the surface coverage and the concentration of inhibitor in aqueous solution.
- Addition of corrosion inhibitor can change the wettability of the steel surface from hydrophilic to hydrophobic.
- A dramatic drop in oil-water interfacial tension occurs with inhibitor addition prior to the critical micelle concentration (CMC).
- A strategy for prediction of the uninhibited and inhibited CO<sub>2</sub> corrosion rates in oil-water two-phase flow is proposed by connecting the phase wetting, three-layer stratified flow, CO<sub>2</sub> corrosion and corrosion inhibition models. The effect of corrosion inhibitor on phase wetting regime and CO<sub>2</sub> corrosion is considered in the strategy.

## 9.2 Future work

A few aspects of future work are:

- Measurement of the thicknesses of water layer and mixing layer under stratified flow by using four traversing conductance probes (Figure 14), which are promising tools to verify three-layer stratified flow model predictions.
- Development of a surface wettability model, which can incorporate the changes of steel surface wettability due to corrosion inhibitor addition.

- Improvement of the current phase wetting prediction model, which overpredicts the critical entrainment oil phase velocity for crude oils.
- Validation of the developed phase wetting prediction model and the proposed strategy for CO<sub>2</sub> corrosion rate predictions with the actual corrosion data in oilfields.
- Investigation of phase wetting in gas-oil-water three-phase flow by modeling and experiment approaches, which include experiments in the doughnut cell and the flow loop.
- Modification of the doughnut cell design to accommodate high temperature and high pressure tests.

**REFERENCE**

- Adams, C.D., Garber, J.D., Walters, F.H., Singh, C. (1993). Verification of computer modeled tubing life predictions by field data. *NACE Corrosion/93*, paper no. 93082.
- Angeli, P., & Hewitt, G.F. (2000). Flow structure in horizontal oil-water flow. *International Journal of Multiphase Flow*, 26, 1117-1140.
- Arirachakaran, S., Oglesby, K.D., Malinowsky, M.S., Shoham, O., Brill, J.P. (1989). An analysis of oil/water flow phenomena in horizontal pipes. *SPE Professional Production Operating Symposium*, paper no. 18836.
- Ayello, F., Robbins, W.K., Richter, S., & Nestic, S. (2008a). Crude oil chemistry effects on inhibition of corrosion and phase wetting. *17th International Corrosion Congress*, paper no. 3149.
- Ayello, F., Li, C., Tang, X., Cai, J., Nestic, S., Cruz, C.I.T., & Al-Khamis, J.N. (2008b). Determination of phase wetting in oil-water pipe flows. *NACE Corrosion/08*, paper no. 08566.
- Barnea, D. (1986). Transition from annular flow and from dispersed bubble flow – unified models for the whole range of pipe inclinations. *International Journal of Multiphase Flow*, 12, 733-744.
- Barnea, D. (1987). A unified model for predicting flow-pattern transitions for the whole range of pipe inclinations. *International Journal of Multiphase Flow*, 13, 1-12.
- Batchelor, G.K. (1951). Pressure fluctuations in isotropic turbulence. *Proceedings of the*

*Cambridge Philosophical Society*, 47, 359-374.

Bockris, J.O.M., Drazic, D., & Despic, A.R. (1961). The electrode kinetics of the deposition and dissolution of iron. *Electrochimica Acta*, 4, 325.

Bond, W.N., & Newton, D.A. (1928). Bubbles, drops, and Stokes' law. *Philosophy Magazine*, 5, 794-800.

Brauner, N., & Maron, D.M. (1989). Two phase liquid-liquid stratified flow. *Physicochemical Hydrodynamics*, 11, 487-506.

Brauner, N., & Maron, D.M. (1992). Flow pattern transitions in two-phase liquid-liquid flow in horizontal tubes. *International Journal of Multiphase Flow*, 18, 123-140.

Brauner, N. (2001). The prediction of dispersed flows boundaries in liquid-liquid and gas-liquid systems. *International Journal of Multiphase Flow*, 27, 885-910.

Brodkey, R.S. (1969). *The Phenomena of fluid motions*. Reading, MA: Addison-Wesley.

Cai, J., Nestic, S., & de Waard, C. (2004). Modeling of water wetting in oil-water pipe flow. *NACE Corrosion/04*, paper no. 04663.

Cai, J., Nestic, S., Li, C., Tang, X., Ayello, F., Cruz, C.I.T., & Al-Khamis, J.N. (2005a). Experimental studies of water wetting in large diameter horizontal oil-water pipe flows. *SPE Annual Technical Conference and Exhibition*, paper no. 95512-MS.

Cai, J., Li, C., Tang, X., Ayello, F., & Nestic, S. (2005b). Water wetting and CO<sub>2</sub> corrosion in horizontal & inclined oil-water pipe flows. *Institute for Corrosion and Multiphase Technology, Ohio University*, a final water wetting project report to Saudi Aramco Oil Company.

Charles, M.E., Govier, G.W., & Hodgson, G.W. (1961). The horizontal pipeline flow of

- equal density oil-water mixtures. *Canadian Journal of Chemical Engineering*, 39, 27-36.
- Chokshi, K.K. (2004). A study of inhibitor – scale interaction in carbon dioxide corrosion of mild steel. *Master's thesis*, Ohio University.
- Clay, P.H. (1940). The mechanism of emulsion formation in turbulent flow. *Proceedings of the Section of Sciences*, 43, 852-965.
- Colebrook, C.F. (1939). Turbulent flow in pipes, with particular reference to the transition region between the smooth and rough pipe laws, *Journal of Institution of Civil Engineers*, 11, 133-156.
- Craig, B. (1998). Predicting the conductivity of water-in-oil solutions as a means to estimate corrosiveness. *NACE Corrosion/98*, paper no. 98657.
- de Waard, C., & Milliams, D.E. (1975a). Carbon acid corrosion of steel. *Corrosion*, 31, 177-181.
- de Waard, C., & Milliams, D.E. (1975b). Prediction of carbonic acid corrosion in natural gas pipelines. *First International Conference on the Internal and External Protection of Pipes*, paper no. F1.
- de Waard, C., & Lotz, U. (1993). Prediction of CO<sub>2</sub> corrosion of carbon steel. *NACE Corrosion/93*, paper no. 93069.
- de Waard, C., Lotz, U., & Dugstad, A. (1995). Influence of liquid flow velocity on CO<sub>2</sub> corrosion: a semi-empirical model. *NACE Corrosion/95*, paper no. 95128.
- de Waard, C., Smith, L., & Craig, B.D. (2001). The influence of crude oil on well tubing corrosion rates. *EUROCORR 2001*, The European Corrosion Congress.

- Dhar, H.P., Conway, B.E., & Joshi, K.M. (1973). On the form of adsorption isotherms for substitution adsorption of molecules of different sizes. *Electrochemical Acta*, 18, 789-798.
- Dugstad, A., Nyborg, R., & Seiersten, M. (2003). Flow assurance of pH stabilized wet gas pipelines. *NACE Corrosion/03*, paper no. 03314.
- Durnie, W.H. (2000). Development of a structure/activity relationship for carbon dioxide corrosion inhibitors. *Doctoral dissertation*, Curtin University of Technology.
- Fairuzov, Y.V., Arenas-Medina, P., Verdejo-Fierro, J., & Gonzalez-Islas, R. (2000). Flow pattern transportation in horizontal pipelines carrying oil-water mixtures: full-scale experiments. *Journal of Energy Resources Technology*, 122, 169-176.
- Fang, H., Nesic, S., & Wang, S. (2006). CO<sub>2</sub> corrosion of carbon steel in high ionic strength brine solution. *NACE Corrosion/06*, paper no. 06372.
- Federal Highway Administration. (2002). Corrosion costs and preventive strategies in the United States. *United States Department of Transportation*, publication no. FHWA-RD-01-156.
- Foss, M., Gulbrandsen, E., & Sjoblom, J. (2008). Interaction of carbon dioxide corrosion inhibitors with corrosion products deposit. *NACE Corrosion/08*, paper no. 08343.
- Gray, L.G.S., Anderson, B.G., Danysh, M.J., & Tremaine, P.R. (1989). Mechanisms of carbon steel corrosion in brines containing dissolved carbon dioxide at pH 4. *NACE Corrosion/89*, paper no. 89464.
- Gray, L.G.S., Anderson, B.G., Danysh, M.J., & Tremaine, P.R. (1990). Effect of pH and

temperature on the mechanism of carbon steel corrosion by aqueous carbon dioxide. *NACE Corrosion/90*, paper no. 90040.

Guet, S., Rodriguez, O.M.H., Oliemans, R.V.A., & Brauner, N. (2006). An inverse dispersed multiphase flow model for liquid production rate determination. *International Journal of Multiphase Flow*, 32, 553-567.

Gusmano, G., Labella, P., Montesperelli, G., Privitera, A., & Tassinari, S. (2006). Study of the inhibition mechanism of imidazolines by electrochemical impedance spectroscopy. *Corrosion*, 62, 576-583.

Haaland, S.E. (1983). Simple and explicit formulas for the friction factor in turbulent pipe flow. *Journal of Fluids Engineering*, 105, 89-90.

Halvorsen, A.M.K., Andersen, T.R., Halvorsen, E.N., Kojen, G.P., & Skar, J.I. (2007). The relationship between internal corrosion control method, scale control and MEG handling of a multiphase carbon steel pipeline carrying wet gas with CO<sub>2</sub> and acetic acid. *NACE Corrosion/07*, paper no. 07313.

Hinze, J.O. (1955). Fundamentals of the hydrodynamic mechanism of splitting in dispersion processes. *AIChE Journal*, 1, 289-295.

Hurlen, T., Gunvaldsen, S., Tunold, R., Blaker, F., & Lunde, P.G. (1984). Effects of carbon dioxide on reactions at iron electrodes in aqueous salt solutions. *Journal of Electroanalytical Chemistry*, 180, 511-526.

Jacobson, G.A. (2007). Corrosion at Prodhoe Bay - a lesson on the line. *Materials Performance*, 46, no. 8, 26-34.

Kapusta, S.D., Pots, B.F.M., & Connell, R.A. (1999). Corrosion management of wet gas

- pipelines. *NACE Corrosion/99*, paper no. 99045.
- Knag, M., Sjoblom, J., & Gulbrandsen, E. (2006). Partitioning of a model corrosion inhibitor in emulsions. *Journal of Dispersion Science and Technology*, 27, 65-75.
- Kurban, A.P.A., Angeli, P.A., Mendes-Tassis, M.A., & Hewitt, G.F. (1995). Stratified and dispersed oil-water flows in horizontal pipes. *7th International Conference on Multiphase Production*, 277-291.
- Li, C., Tang, X., Ayello, F., Cai, J., Nestic, S., Cruz, C.I.T., & Al-Khamis, J.N. (2006a). Experimental study on water wetting and CO<sub>2</sub> corrosion in oil-water two-phase flow. *NACE Corrosion/06*, paper no. 06595.
- Li, C. (2006b). Mechanisms of inhibition of scaling and fouling. *Department of Chemical and Biomolecular Engineering, Ohio University*, Ph.D. comprehensive exam report.
- Li, C., Richter, S., & Nestic, S. (2008). Effect of corrosion inhibitor on water wetting and CO<sub>2</sub> corrosion in an oil-water two-phase system. *17th International Corrosion Congress*, paper no. 2662.
- Lotz, U. (1990). Velocity effects in flow induced corrosion. *NACE Corrosion/90*, paper no. 90027.
- McMahon, A.J. (1990). The mechanism of a sodium alkylethoxyphosphate as an oilfiled corrosion inhibitor. *Proceedings of the 7th European Symposium on Corrosion Inhibitors (7SEIC)*, no. 9.
- McMahon, A.J. (1991). The mechanism of action of an oleic imidazoline based corrosion inhibitor for oilfiled use. *Colloids and Surfaces*, 59, 187-208.

- Moon, T., & Horsup, D. (2002). Relating corrosion inhibitor surface active properties to field performance requirements. *NACE Corrosion/02*, paper no. 02298.
- Nadler, M., & Mewes, D. (1997). Flow induced emulsification in the flow of two immiscible liquids in horizontal pipes. *International Journal of Multiphase Flow*, 23, 55-68.
- Nesic, S., & Postlethwaite, J. (1996a). An electrochemical model for prediction of CO<sub>2</sub> corrosion. *Corrosion*, 52, 280-293.
- Nesic, S., Thevenot, N., Crolet, J.L., & Drazic, D.M. (1996b). Electrochemical properties of iron dissolution in the presence of CO<sub>2</sub> – basics revisited. *NACE Corrosion/96*, paper no. 96003.
- Nesic, S., & Carroll, F. (2003). Horizontal rotating cylinder - a compact apparatus for studying the effect of water wetting on carbon dioxide corrosion of mild steel. *Corrosion*, 59, no. 12, 1085-1095.
- Nesic, S., & Lee, J. (2003). A mechanistic model for carbon dioxide corrosion of mild steel in the presence of protective iron carbonate films-part3: film growth model. *Corrosion*, 59, 616-628.
- Nesic, S., Wang, S., Cai, J., & Xiao, Y. (2004). Integrated CO<sub>2</sub> corrosion – multiphase flow model. *NACE Corrosion/04*, paper no. 04626.
- Nesic, S. (2007). Key issues related to modeling of internal corrosion of oil and gas pipelines – a review. *Corrosion Science*, 49, 4308-4338.
- Nesic, S., Li, H., Sormaz, D., & Huang, J. (2008a). A free open source mechanistic

- model for prediction of mild steel corrosion. *17th International Corrosion Congress*, paper no. 2659.
- Nesic, S., Wang, S., Lee, J., Sun, W., & Fang, H. (2008b). A new updated model of CO<sub>2</sub>/H<sub>2</sub>S corrosion in multiphase flow. *NACE Corrosion/08*, paper no. 08535.
- Nordsveen, M., Nesic, S., Nyborg, R., & Stangeland, A. (2003). A mechanistic model for carbon dioxide corrosion of mild steel in the presence of protective iron carbonate films-part1: theory and verification. *Corrosion*, 59, 443-456.
- Nyborg, R. (2002). Overview of CO<sub>2</sub> corrosion models for wells and pipelines. *NACE Corrosion/02*, paper no. 02233.
- Papavinasam, S. (2000). Corrosion inhibitors. In R.W. Revie (Ed.), *Uhlig's corrosion handbook* (pp. 1091-1096). New York: John Wiley & Sons.
- Papavinasam, S., Doiron, A., Panneerselvam, T., & Revie, R.W. (2007). Effect of hydrocarbons on the internal corrosion of oil and gas pipelines. *Corrosion*, 63, no. 7, 704-712.
- Pots, B.F.M. (1995). Mechanistic models for the prediction of CO<sub>2</sub> corrosion rates under multiphase flow conditions. *NACE Corrosion/95*, paper no. 95137.
- Pots, B.F.M., Hollenberg, J.F., & Hendriksen, E.L.J.A. (2006). What are the real influences of flow on corrosion. *NACE Corrosion/06*, paper no. 06591.
- Ramachandran, S., Tsai, B., Blanco, M., Chen, H., Tang, Y., & Goddard, W.A. (1996). Self-assembled monolayer mechanism for corrosion inhibition of iron by imidazolines. *Langmuir*, 12, 6419-6428.
- Rippon, I.J., & Simon Thomas, M.J.J. (2002). Selection of corrosion control options to

- optimize production field development. *NACE Corrosion/02*, paper no. 02278.
- Rodriguez, O.M.H., & Oliemans, R.V.A. (2006). Experimental study on oil-water flow in horizontal and slightly inclined pipes. *International Journal of Multiphase Flow*, 32, 322-343.
- Rosen, M.J. (2004). *Surfactants and interfacial phenomena* (3rd edition). Hoboken, NJ: John Wiley & Sons.
- Russell, T.W.F., Hodgson, G.W., & Govier, G.W. (1959). Horizontal pipeline flow of mixtures of oil and water. *Canadian Journal of Chemical Engineering*, 37, 9-17.
- Schmitt, G., & Rothmann, B. (1978a). Studies on the corrosion mechanism of unalloyed steel in oxygen-free carbon dioxide solutions, part 1: kinetics of the liberation of hydrogen. *Werkstoffe Und Korrosion*, 28, 154-162.
- Schmitt, G., & Rothmann, B. (1978b). Studies on the corrosion mechanism of unalloyed steel in oxygen-free carbon dioxide solutions, part 2: kinetics of iron dissolution. *Werkstoffe Und Korrosion*, 29, 153-166.
- Schmitt, G., & Stradmann, N. (1998). Wettability of steel surfaces at CO<sub>2</sub> corrosion conditions – 1. effect of surface active compounds in aqueous and hydrocarbon media. *NACE Corrosion/98*, paper no. 98028.
- Shi, H. (2001). A study of oil-water flows in large diameter horizontal pipelines. *Doctoral dissertation*, Ohio University.
- Simmons, M.J.H., & Azzopardi, B.J. (2001). Drop size distribution in dispersed liquid-liquid pipe flow. *International Journal of Multiphase Flow*, 27, 843-859.
- Smith, L.M. (1987). Controlling factors in the rate of CO<sub>2</sub> corrosion. *UK Corrosion'87*

*Brighton.*

- Smith, L.M. (1999). Control of corrosion in oil and gas production tubing. *British Corrosion Journal*, 34, 247-253.
- Taitel, Y., Barnea, D., & Brill, J.P. (1995). Stratified three phase flow in pipes. *International Journal of Multiphase Flow*, 21, 53-60.
- Tang, X., Ayello, F., Li, C., Cai, J., Nestic, S., Cruz, C.I.T., & Al-Khamis, J.N. (2006). Investigation on water wetting in large diameter horizontal and slightly inclined oil-water pipe flows. *11th Middle East Corrosion Conference & Exhibition*.
- Tang, X., Li, C., Ayello, F., Cai, J., Nestic, S., Cruz, C.I.T., & Al-Khamis, J.N. (2007). Effect of oil type on phase wetting transition and corrosion in oil-water flow. *NACE Corrosion/07*, paper no. 07170.
- Tang, X., Richter, S., & Nestic, S. (2008). Study of wettability of different mild steel surface. *17th International Corrosion Congress*, paper no. 3109.
- Torres-Monzon, C.F. (2006). Modeling of oil-water flow in horizontal and near horizontal pipes. *Doctoral dissertation*, The University of Tulsa.
- Trallero, J.L. (1995). Oil-water flow patterns in horizontal pipes. *Doctoral dissertation*, The University of Tulsa.
- Turgoose, S. (2004). Corrosion control in oil and gas industry. *Lecture notes*, Corrosion and Protection Center, UMIST.
- Valle, A., & Utvik, O.H. (1997). Pressure drop, flow pattern and slip for two phase crude oil/water flow: experiments and model predictions. *International Symposium on Liquid-Liquid Two Phase Flow and Transport Phenomena*, Antalya, Turkey.

- Vedapuri, D., Bessette, D., & Jepson, W.P. (1997). A segregated flow model to predict water layer thickness in oil-water flows in horizontal and slightly inclined pipelines. *8th International Conference on Multiphase'97*, 75-105.
- Videm, K., & Kvarekvaal, J. (1996). Surface effects on the electrochemistry of iron and carbon steel electrodes in aqueous CO<sub>2</sub> solutions, *NACE Corrosion/96*, paper no. 96001.
- Videm, K. (2000). The anodic behavior of iron and steel in aqueous solutions with CO<sub>2</sub>, HCO<sub>3</sub><sup>-</sup>, CO<sub>3</sub><sup>2-</sup>, and Cl<sup>-</sup>. *NACE Corrosion/00*, paper no. 00039.
- Vigneaux, P., Chenais, P., & Hulin, J.P. (1998). Liquid-liquid flows in an inclined pipe. *AIChE Journal*, 34, 781-789.
- Wegmann, A., & von Rohr, P.R. (2006). Two phase liquid-liquid flows in pipes of small diameters. *International Journal of Multiphase Flow*, 32, 1017-1028.
- Wicks, M., & Fraser, J.P. (1975). Entrainment of water by flowing oil. *Materials Performance*, 14, no. 5, 9-12.
- Wu, Y. (1995). Entrainment method enhanced to account for oil's water content. *Oil & Gas Journal*, 93, issue 35, 83-86.

## **APPENDIX A: INTERFACE OF ACQUISITION SOFTWARE FOR WALL CONDUCTANCE PROBES USED ON FLOW LOOP AND DOUGHNUT CELL**

Wall conductance probe used for phase wetting determination in the flow loop and in the doughnut cell experiments is key measurement technique in this work. Considering convenience of data collection, an acquisition software for wall conductance probes has been developed in this work. The acquisition software communicates with the electric boards, which transfer the measured voltage of all probes to the computer. The first version of the software was developed by Mr. Albert Schubert (laboratory director) for the two test sections (93 and 160 probes installed respectively) used in the flow loop. The interface of the software and a time function of data collection were updated and added by the author in 2006. Later the software was further updated by the author in 2007 to accommodate the wall conductance probes used in the doughnut cell and the newly designed traversing probes (mentioned in Chapter 4) used in the flow loop. The software was developed in programming with Visual Basic 6.0.

Figure 81 shows the main interface of the software. Four options are available on the main interface: 160 and 93 wall conductance probes for the upstream and downstream test sections on the flow loop, respectively; 140 wall conductance probes on the doughnut cell and 4 traversing probes on the flow loop. The interfaces of each individual function are shown in Figure 82 to Figure 85.

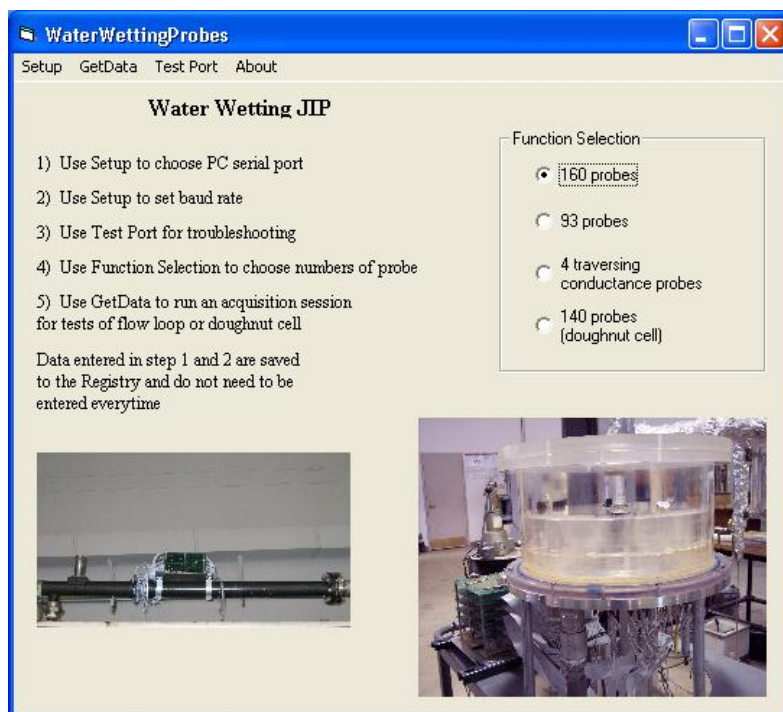


Figure 81 Main interface of the acquisition software.

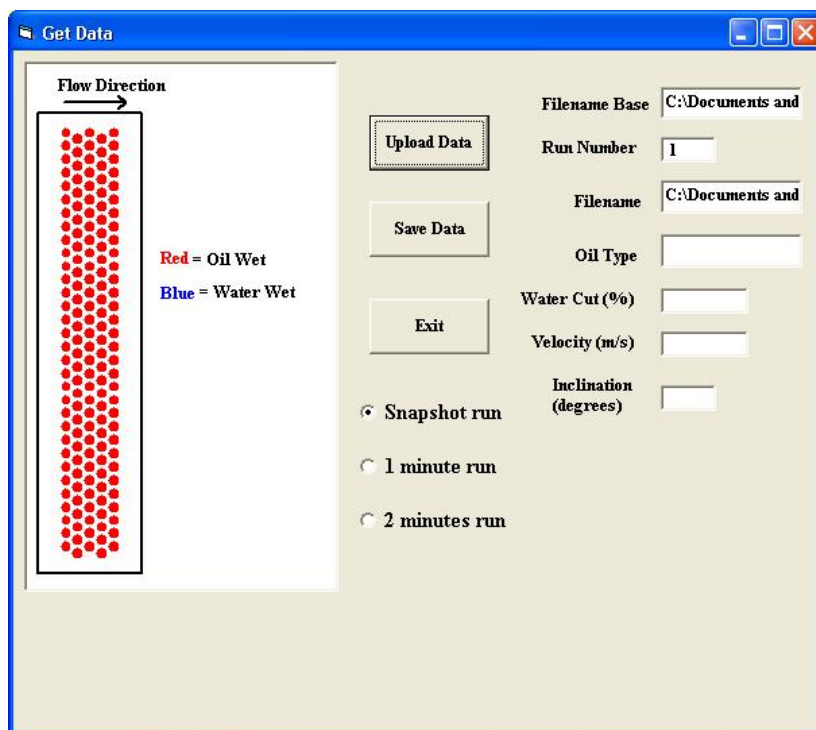


Figure 82 Interface of 160 wall conductance probes on the upstream test section.

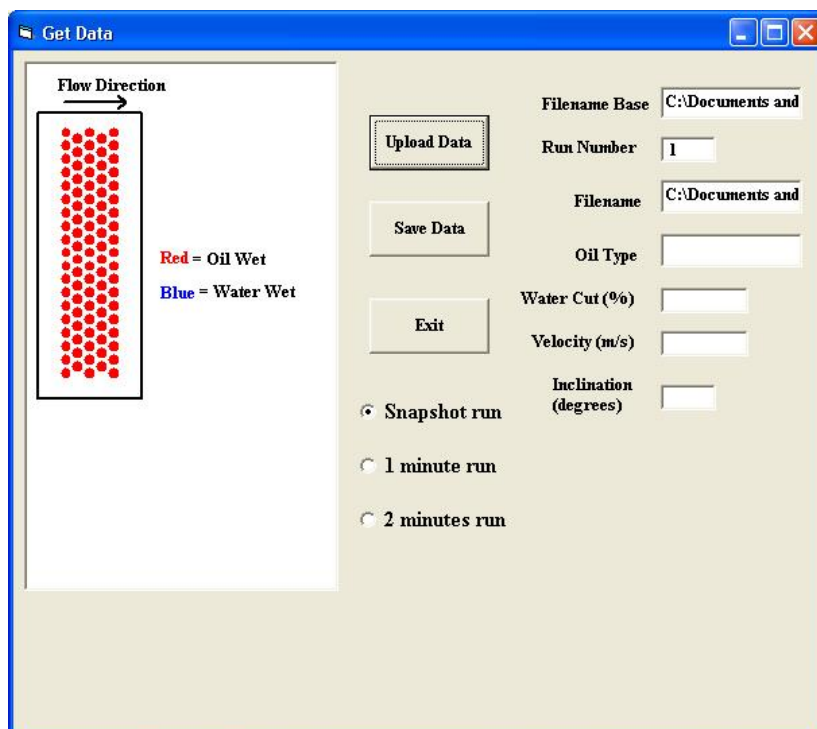


Figure 83 Interface of 93 wall conductance probes on the downstream test section.

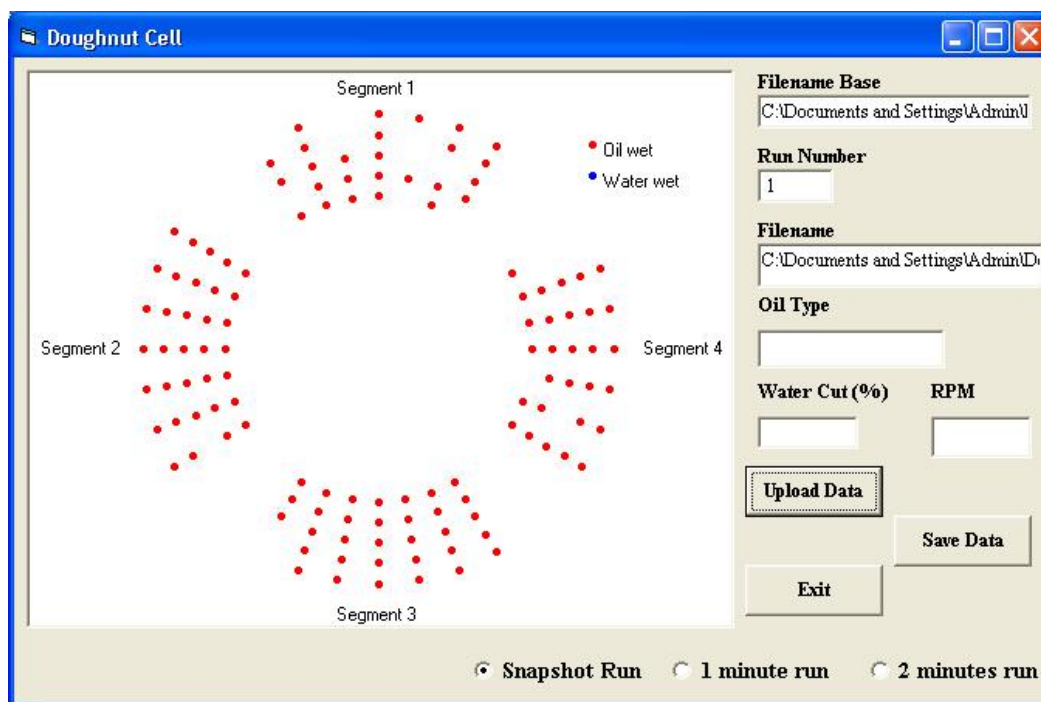


Figure 84 Interface of 140 wall conductance probes on the doughnut cell.

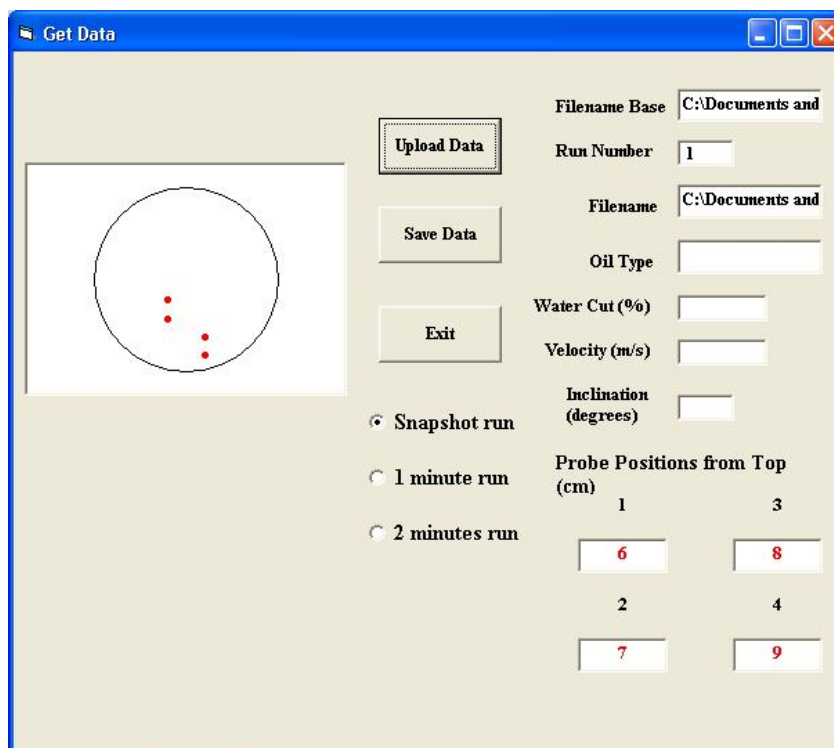


Figure 85 Interface of 4 traversing probes on the test section.